12-2013

Synthesis, Basic Characterization, and Resonant Ultrasound Studies of Novel Materials: Iron-based Superconductors and Mo3Sb7-based Thermoelectrics

Lindsay Heatherly Vanbebber
The University of Tennessee - Knoxville, lheathe2@utk.edu

To the Graduate Council:

I am submitting herewith a dissertation written by Lindsay Heatherly Vanbebber entitled "Synthesis, Basic Characterization, and Resonant Ultrasound Studies of Novel Materials: Iron-based Superconductors and Mo3Sb7-based Thermoelectrics." I have examined the final electronic copy of this dissertation for form and content and recommend that it be accepted in partial fulfillment of the requirements for the degree of Doctor of Philosophy, with a major in Materials Science and Engineering.

Veerle M. Keppens, Major Professor

We have read this dissertation and recommend its acceptance:

Erik G. Herbert, William J. Weber, Haidong Zhou

Accepted for the Council:

Carolyn R. Hodges

Vice Provost and Dean of the Graduate School

(Original signatures are on file with official student records.)

Synthesis, Basic Characterization, and Resonant Ultrasound Studies of Novel Materials: Iron-based Superconductors and Mo3Sb7-based Thermoelectrics

A Dissertation Presented for the
Doctor of Philosophy
Degree
The University of Tennessee, Knoxville

Lindsay Heatherly VanBebber
December 2013

Dedication

To my husband and parents for all the love and support I could ever want, and to my daughters who make every day brighter.

Acknowledgments

I have been very fortunate to work with some truly wonderful people in the process of completing this work.

I would like to express my gratitude, first and foremost, to Dr. Veerle Keppens. Her guidance has been instrumental; not only has she spent valuable time editing this dissertation and many other items, but she has always been available for support and advice. She has established a very encouraging work environment, for which I am very grateful. I would also like to thank Dr. Erik Herbert, Dr. George Pharr, Dr. William Weber, and Dr. Haidong Zhou for dedicating their time to serve on my committee.

I also feel especially fortunate to have had wonderful colleagues to work with in the lab. Michael Koehler, Ling Li, Amanda Haglund, Lin Jia, and Yanbing Luan have provided great help with equipment maintenance and programming. Moreover, they have helped to develop an enjoyable work environment with plenty of support and a great rapport. In addition, the MSE staff has been terrific; they have gone above and beyond to help with many issues throughout the years.

I am also very grateful to Athena Safa-Sefat, Brian Sales, Michael McGuire, and David Mandrus at Oak Ridge National Laboratory for the incredible help with sample preparation and characterization. I am honored to have had such a remarkable experience learning from them. A special thanks also goes to Jiaqiang Yan and Olivier Delaire for supplying many high-quality samples for study.

Abstract

The elastic behavior of materials with unusual low-temperature behavior involving structural, magnetic, and superconducting transitions has been studied using Resonant Ultrasound Spectroscopy (RUS). Two classes of materials have been examined, namely, iron-based superconductors and thermoelectric materials. A series of BaFe2As2 materials as well as TlFe1.6Se2 comprise the former class, and a series of Mo3Sb7 materials is included in the latter.

The elastic behavior of BaFe2As2 reveals that a large softening is observed as the material approaches a tetragonal-to-orthorhombic structural transition accompanied by an antiferromagnetic ordering near 132K. This significant shear softening indicates that the structural transition is due to magnetically-driven nematic fluctuations. The elastic behavior of superconducting cobalt-doped BaFe2As2, with a critical temperature of 22K, supports this finding. In BaFe2As2, an unusually large amount of softening is observed as the material approaches the superconducting transition, and the material begins to stiffen immediately following this transition. The effect of chromium doping in the BaFe2As2 material is also examined. It is found that chromium doping does not produce superconductivity at any concentration. It is shown that the structural transition that occurs in the BaFe2As2 parent material is suppressed with chromium doping, but this suppression is slower than that observed in cobalt-doped compounds. The TlFe1.6Se2 material displays a slight softening at 140K, where a canting of the iron spins occurs. When the original magnetic structure is recovered at 100K, stiffening is observed. A magnetic field of 3T does not affect the elastic response despite the magnetic feature.

The elastic behavior of a series of Mo3Sb7 single crystals is also examined with RUS. The temperature dependence of the elastic response of this material reveals a transition at around

53K, evidenced by a dramatic softening in *c'*. This softening is associated with a cubic-to-tetragonal structural transition. Single crystals that were doped with chromium, ruthenium, and tellurium were also examined. The chromium doping simply decreases the transition temperature by approximately 5K. While the addition of ruthenium and tellurium suppresses the transition, a structural instability persists, evidenced by a remaining *c'* softening.

Key words: Elastic Properties; Resonant Ultrasound Spectroscopy (RUS); Iron-based Superconductors; Thermoelectric Materials

Table of Contents

List of Figures

Introduction

Both superconducting materials and thermoelectric materials have the potential to make significant impacts on future energy processes and applications. Superconducting materials present zero electrical resistance which has obvious benefits for preserving current, and the Meissner effect observed in the superconducting state has also generated numerous potential applications. Thermoelectric materials have the ability to convert heat into electrical energy or vice versa. This ability provides promising applications in energy salvage as well as solid-state refrigeration. Though these materials present remarkable possibilities, each of these types of materials faces some ongoing challenges that must be faced before such proposed impacts can be achieved. The critical temperature of superconducting materials remains at cryogenic temperatures, while the efficiency of thermoelectric materials is not adequate for many practical applications.

The discovery of iron-based superconductors in 2008 was followed by a flurry of investigations into this new class of high-temperature superconductors. Because other high-temperature superconducting systems have been intensively studied for decades, and many important questions remain unanswered, the chance to investigate these new systems has been a welcome opportunity. It is anticipated that a better understanding of these materials may lead to the development of improved superconducting materials.

Though thermoelectric materials have been used for many years, their efficiency remains an issue. Because much current research is focused on reduction of the lattice portion of the thermal conductivity, a better understanding of the lattice dynamics of these materials is important. A better understanding may lead to the ability to enhance the thermoelectric properties.

The focus of this research is the elastic properties of compounds from these two classes of materials, namely members of the $BaFe_2As_2$ superconducting family and the $TlFe_{2-x}Se_2$ superconducting family and promising thermoelectric Mo_3Sb_7 and its doped variants. These studies are performed using Resonant Ultrasound Spectroscopy (RUS). RUS is a novel technique used to examine the elastic behavior of materials based on the measurement of a freely-vibrating sample's naturally-occurring resonant frequencies. RUS is used to determine the elastic tensor of a material, and the elastic constants that form this tensor are directly related to the atomic bonding of the material in addition to being linked to its thermal properties. The RUS technique is known to be extremely sensitive to transitions and ordering phenomena. Studying these materials and their various transitions with RUS provides valuable information about the physics that govern these transitions and contributes to a better understanding of the mechanisms involved.

The first chapter provides a summary of the literature concerning these materials, and the second chapter introduces the RUS technique used as well as the single-crystal growth process used to synthesize the samples. Chapters 3 and 4 outline the results of these RUS measurements as well as other information obtained during this study. A conclusion of this dissertation is provided after the final chapter.

Chapter 1

Literature Review

1.1 Superconductivity

Simply stated, superconductivity is the absence of electrical resistivity. The phenomenon of superconductivity was first discovered in 1911 by Heike Kamerlingh Onnes on elemental mercury following the successful liquefaction of helium [1]. The critical temperature (T_c), or temperature below which a material becomes superconducting, for mercury was measured at 4.2K. Following this result, the elements lead and tin were also found to be superconducting, and with time, many more materials were found to be superconducting at very low temperatures.

In 1914, Heike Kamerlingh Onnes also observed that magnetic fields have a destructive effect on superconductivity [1]. This effect is manifested as a critical field, the magnetic field at and above which the superconductivity is destroyed. The value of this critical field is dependent on the superconductor itself; it also distinguishes between two types of superconductors: Type I and Type II. Type I superconductors have a single critical field at which superconductivity is destroyed, whereas, Type II superconductors have a lower and an upper critical field. Above the lower critical field, the magnetic field can partially penetrate the material; the upper critical field is the field at which superconductivity is destroyed.

In addition to the critical field, superconductors have a critical current density. This value is the maximum amount of current that can flow through a superconductor without driving the material from the superconducting state to the normal state. Because flowing current creates a magnetic field, this critical current density is expected from the observation of the critical field.

Superconductivity is not simply perfect conductivity. The phenomenon of superconductivity is not only distinguished by zero electrical resistance, but it is also

characterized by strong diamagnetism. This characteristic is well illustrated by the Meissner effect discovered by Meissner and Ochsenfeld in 1933 [2]. This effect is a complete expulsion of a sufficiently weak magnetic field from the bulk of the superconducting material as it transitions form the normal state to the superconducting state. In a magnetic field that is lower than the critical field for the material, the superconductor develops electric currents near its surface, and the magnetic field of these currents cancels the applied magnetic field within the interior of the superconductor.

It was not until 1957 that a theory was developed to explain the microscopic origins of superconductivity; this theory is known as the BCS theory of superconductivity as it was proposed by Bardeen, Cooper, and Schrieffer [3]. Cooper had established the idea of bound electron pairs, now known as Cooper pairs, in 1956 [2]. Interactions between electrons and lattice vibrations cause the electrons to interact. Essentially, an electron moving through the lattice leaves behind a small distortion, which pulls in a second electron, and these two electrons form a pair. At low temperatures, many of these electron pairs form, and their wavefunctions align. These Cooper pairs, according to BCS theory, carry the current in the superconductor. BCS theory successfully predicts many of the properties of early superconductors, but it is unclear how applicable it is to newer, high-temperature superconductors. Thermal vibrations at higher temperatures (above about 30K) should be sufficient to destroy the phonon-mediated pairing of the electrons.

With the goal of finding superconducting materials with higher T_c values, many materials were explored throughout the middle of the twentieth century. However, T_c values above 30K were not found, which agreed with the prediction from BCS theory. Superconductivity was

utilized during this time for high-value applications, such as magnetic resonance imaging, but its use was limited because of the expense to cool the material to such low temperatures.

High-temperature superconductivity was first discovered in 1986 by Bednorz and Müller [4]. A copper oxide ceramic material, $Ba_xLa_{5-x}Cu_5O_{5(3-y)}$, was found to have a T_c of 35K. Shortly thereafter, in 1987, Wu et al. discovered that another copper oxide material, $(Y_{1-x}Ba_x)_2CuO_{4-\delta}$, becomes superconducting below 93K [5]. These discoveries were the start of intensive research in the field of high-temperature superconductivity. The term "high-temperature" is relative and generally refers to families of superconductors that do not appear to conform to BCS theory. Still, some of these copper oxide superconducting materials have a T_c well above 77K, the boiling point for liquid nitrogen, which means that cooling these materials below T_c is much simpler and much cheaper.

Despite the extensive investigations of these materials, there exists no complete, agreed-upon theoretical explanation for high-temperature superconductivity. Aside from the thermal energy being too high for these materials to become superconducting at such high temperature according to BCS theory, the properties of copper oxide superconductors are qualitatively different from classical superconductors in their normal state. In particular, the parent materials tend to display antiferromagnetism, a property unexpected near superconductivity due to the effect that magnetism has on superconductivity. The interaction between these two properties has been the subject of much study [6]. Many theories have been developed to explain behavior in nonconventional superconductors, but none of these theories has been widely accepted as a comprehensive description. The discovery of high-temperature superconductivity led to thoughts of room-temperature superconductivity, though, so far, the maximum T_c achieved under atmospheric pressure is less than 140K.

1.2 Iron-based Superconductors

In 2008, a class of high-temperature, iron-based superconducting materials was unexpectedly discovered [7]. These superconductors are the first non-copper oxide materials to display transition temperatures in excess of 50K [8-10], though, these temperatures are lower than those of the copper oxide superconductors. This discovery has presented an excellent opportunity to further study unconventional superconductivity. Although high-temperature superconductivity has been extensively researched since 1986, much remains uncertain about this phenomenon, and the iron-based superconductors have provided a new avenue for this study. It is hoped that these materials may provide insight into the properties that are essential to high-temperature superconductivity, which may aid in revealing other classes of superconducting materials. The excitement about these new materials is evidenced by the numerous studies that began immediately after their discovery.

Much curiosity about these new superconductors was due to the fact that they contain iron (probably the most well-known ferromagnetic element). Generally, superconductivity and magnetism are thought to be incompatible, and magnetic materials have largely been avoided in superconductivity research [11, 12]. Therefore, the simple existence of these iron-based superconducting materials revealed that an adequate understanding of superconductivity and its origins is lacking.

Most high-temperature superconductivity research has focused on copper oxide materials; however, these new iron-based materials have many characteristics that make them desirable for study. One distinct advantage of the iron-based superconductors is the fact that they are metallic rather than insulating ceramic, and the processing of this class of materials may make applications more practical. In addition, high-quality single crystals can be made for some

of these new materials. Furthermore, the crystal structures of some of these materials are simpler than those of the copper oxides. On the other hand, these materials share some qualities with the cuprate superconductors as well. In particular, both groups tend to have a two-dimensional structure and display antiferromagnetism in their parent materials.

Superconductivity was first observed for this class of materials in fluorine-doped LaFeAsO [7]. However, superconductivity was quickly observed in many similar materials and has now been seen in at least five different structural classes. These different structures are illustrated in Figure 1.1. Each of these structures is based on stacking planar layers consisting of iron atoms tetrahedrally coordinated to a pnictogen (most often arsenic) or chalcogen. The spacer layers between the iron-pnictogen (or chalcogen) layers are what distinguish these different structures. For convenience, these structures are often referred to as 11, 111, 122, 1111, and 32522 structures according to their chemical formula. These similar layered structures direct many to believe that superconductivity originates within the iron-pnictogen (or iron-chalcogen) layers. It is also thought that tuning the structure is key to controlling superconductivity.

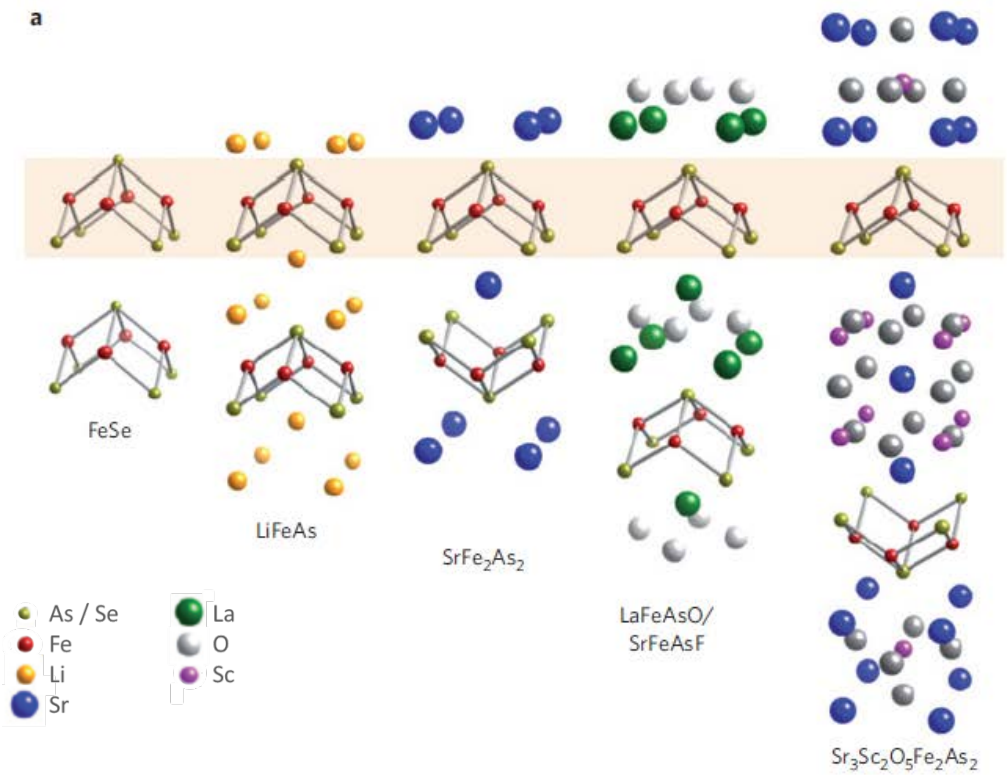

Figure 1.1. Structures of the various types of iron-based superconductors.[12] (Space group for FeSe, LiFeAs, and LaFeAsO is P4/nmm; space group for $SrFe_2As_2$ and $Sr_3Sc_2O_5Fe_2As_2$ is I4/mmm.)

In general, the emergence of superconductivity in these materials requires chemical doping or application of pressure to a parent material. These parent materials typically display a spin-density-wave antiferromagnetic order below their Curie temperature. Figure 1.2 illustrates the ordered moments of the FeAs layers in the antiferromagnetic parent material. The parent materials also undergo a structural transition, usually tetragonal-to-orthorhombic, around the Curie temperature. It is thought that this structural distortion is due to magnetostructural coupling; the magnetic interactions drive the distortion.

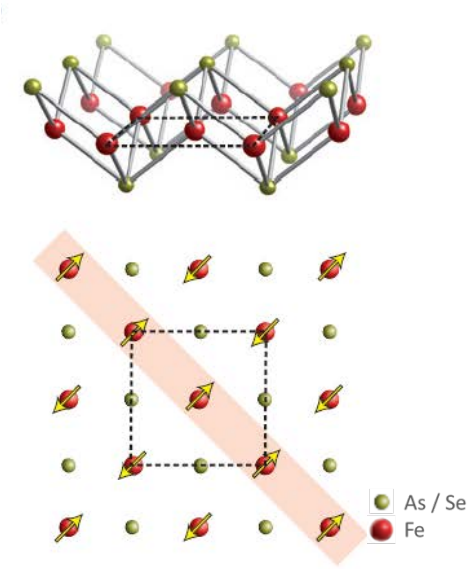

Figure 1.2. Illustration of the iron-pnictogen (or chalcogen) layer and the ordered moments of the FeAs-based materials.[12]

1.2.1 $BaFe_2As_2$

The 122 structural family of iron-based superconductors is most often studied due to the availability of single crystalline samples, the absence of oxygen, and the simplicity of its structure (seen in Figure 1.3). More importantly, this family of materials is believed to represent all of the significant characteristics of iron-based superconductors. The $BaFe_2As_2$ compound is the most notable member of this family.

At room temperature, the $BaFe_2As_2$ parent material has the $ThCr_2Si_2$-type structure. This material then displays the antiferromagnetic ordering and tetragonal-to-orthorhombic (*I4/mmm* to *Fmmm* [13]) structural transition at about 132K. This material is known to become superconducting upon the application of pressure or with the correct doping [13], and it has been observed that both hole doping on the Ba site [14] and electron doping in the FeAs layers [15] produce superconductivity. Partial phase diagrams for $BaFe_2As_2$ are given in Figure 1.4; these diagrams show how the material changes with both chemical substitution and pressure.

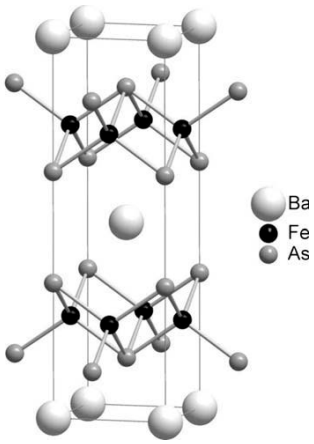

Figure 1.3. Room temperature $BaFe_2As_2$ structure.[13]

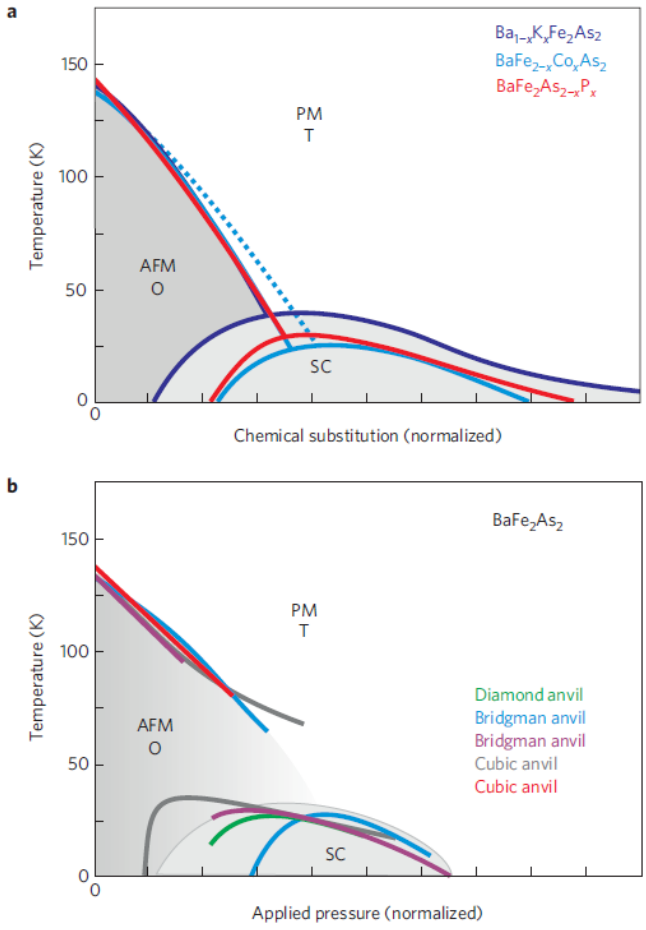

Figure 1.4. General phase diagrams for $BaFe_2As_2$. The effects of chemical doping are displayed in (a), and the effects of applied pressure are revealed in (b). (AFM – antiferromagnetic; PM – paramagnetic; O – orthorhombic; T – tetragonal; SC – superconducting).[12]

As seen in the phase diagrams, the structural transition to orthorhombic symmetry and the magnetic transition to an antiferromagnetic phase are eliminated and a superconducting dome forms with the addition of dopants or the application of pressure. The most notable aspect of these phase diagrams is the fact that the superconducting dome crosses into the antiferromagnetic region. In other words, at some temperatures, the magnetic order and superconductivity coexist for some doping concentrations and pressures. Phase separation into superconducting and magnetic phases was observed with μSR [16] in the chemically-doped samples.

In each of the optimal superconductors (having the highest T_c), superconductivity emerges following the suppression of both the antiferromagnetic spin-density-wave ordering and an associated tetragonal-to-orthorhombic structural transition. Thus, the spin fluctuations of iron are thought to be important in developing superconductivity in these materials. Since the superconductivity in iron-based compounds is known to take place in the proximity of these phase transitions, understanding the interactions that bring about these transitions is critical to understanding the development of superconductivity.

1.2.1.1 Cobalt-doped $BaFe_2As_2$

As mentioned, $BaFe_2As_2$ requires either chemical doping or application of pressure in order to become superconducting, and cobalt is often used as a dopant. Cobalt doping is known to produce superconductivity in this material at the right concentrations [15]; a partial phase diagram for cobalt-doped $BaFe_2As_2$ is shown in Figure 1.5. The suppression of the structural and magnetic transitions is apparent with the addition of cobalt. When optimally doped, around 8% cobalt, the T_c reaches a value of 22K [15].

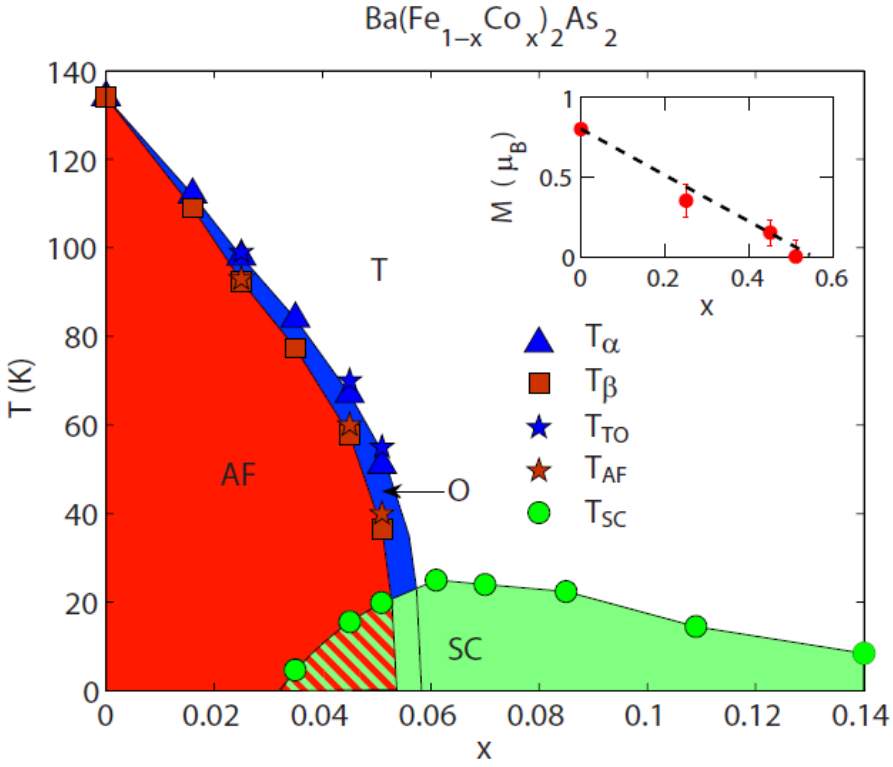

Figure 1.5. Partial phase diagram for the cobalt-doped series of $BaFe_2As_2$ showing the structural and magnetic phase transitions and the existence of superconductivity in an orthorhombic/antiferromagnetic material. (Note that the formula for this material is written differently than discussed in the text.) [17]

The addition of cobalt acts to electron dope the FeAs layers on the iron site, illustrating that the FeAs layers can tolerate in-plane disorder. Cobalt doping is beneficial because it adds carriers directly to the FeAs layers. Cobalt is also easier to handle than other common dopants, and cobalt doping is more homogeneous than other common dopants [15]. Superconductivity emerges for a range of cobalt concentration, and a superconducting dome is formed at low temperatures, as seen in the phase diagram. Interestingly, the phase diagram also shows that the superconducting dome extends into the antiferromagnetic and orthorhombic regions, revealing the coexistence of the magnetic order and the superconducting phase, as well as the existence of superconductivity in the absence of the structural transition.

1.2.1.2 Other Elemental Dopings of $BaFe_2As_2$

Partial substitution with several elemental dopants has successfully produced superconductivity in the $BaFe_2As_2$ material. Hole doping on the barium site with sodium [18], potassium [14], and rubidium [19] has been shown to produce superconductivity. In addition, many partial substitutions on the iron site have produced superconductivity. These successful iron-site dopants include cobalt [15], nickel [20], ruthenium [21, 22], rhodium [23], palladium [23], iridium [24], and platinum [25, 26]. Further, phosphorus [27] doping on the arsenic site has resulted in superconductivity.

Potassium doping of the $BaFe_2As_2$ parent material has produced the highest T_c for this material with chemical doping to date [14]. By substituting for barium, the potassium doping effectively hole dopes this spacer layer. At the proper concentration, the potassium-doped material becomes superconducting at 38K [14]; this optimally-doped material corresponds to an x value of about 0.4. A partial phase diagram is shown in Figure 1.6 that illustrates the superconducting dome that develops with potassium doping. Much like the cobalt-doped material, this material displays a suppression of the structural transition as the amount of dopant is increased. The superconducting dome in this case also extends into the orthorhombic region and, although not shown in the figure, the antiferromagnetically ordered region as well.

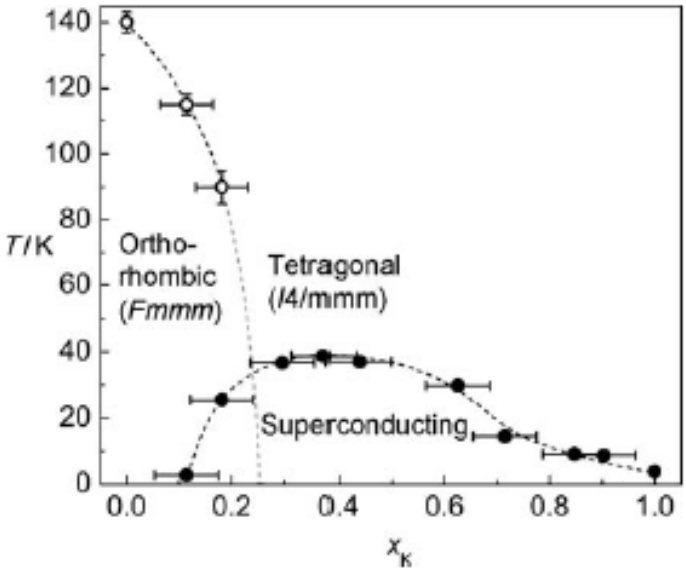

Figure 1.6. Partial phase diagram of $Ba_{1-x}K_xFe_2As_2$ showing the superconducting dome (●) and the structural transition temperatures (○) upon potassium doping.[28]

1.2.2 $TlFe_{1.6}Se_2$

While FeSe becomes a superconductor at about 8K [29], it has been observed that adding a monovalent element (such as K, Rb, Cs, or Tl) to form a spacer layer between square layers of FeSe may result in superconductivity [30-32]. The maximum T_c for this type of material was observed in $K_{0.8}Fe_{1.6}Se_2$ with a value of 32K [30]. These materials have shown interesting behavior as they display both antiferromagnetic order and superconductivity. They also display a large magnetoelastic coupling [32].

Like the $BaFe_2As_2$ parent, $TlFe_{1.6}Se_2$ at high temperature possesses the $ThCr_2Si_2$-type structure. However, iron vacancy ordering occurs around 460K [33], causing the basal plane lattice constant below this temperature to increase to $\sqrt{5}\,a$. Thus, the volume of this superstructure is 5 times larger than the original high-temperature substructure [30, 32-34]. An image of this structure is seen in Figure 1.7. For $TlFe_{2-x}Se_2$, there are always iron vacancies

present, and it is difficult to produce a material with 2-x greater than about 1.7. (Superconductivity with a T_c of 22.4K has been observed for $TlFe_{1.7}Se_2$ [31].) However, replacing some or all of the thallium with another monovalent element can increase this value of x, and increasing this amount of iron tends to increase the value of T_c for these materials [31]. $TlFe_{1.6}Se_2$ does not become a superconductor but becomes an antiferromagnetic insulator, illustrating the existence of an iron-based superconductor bordering on this very different behavior.

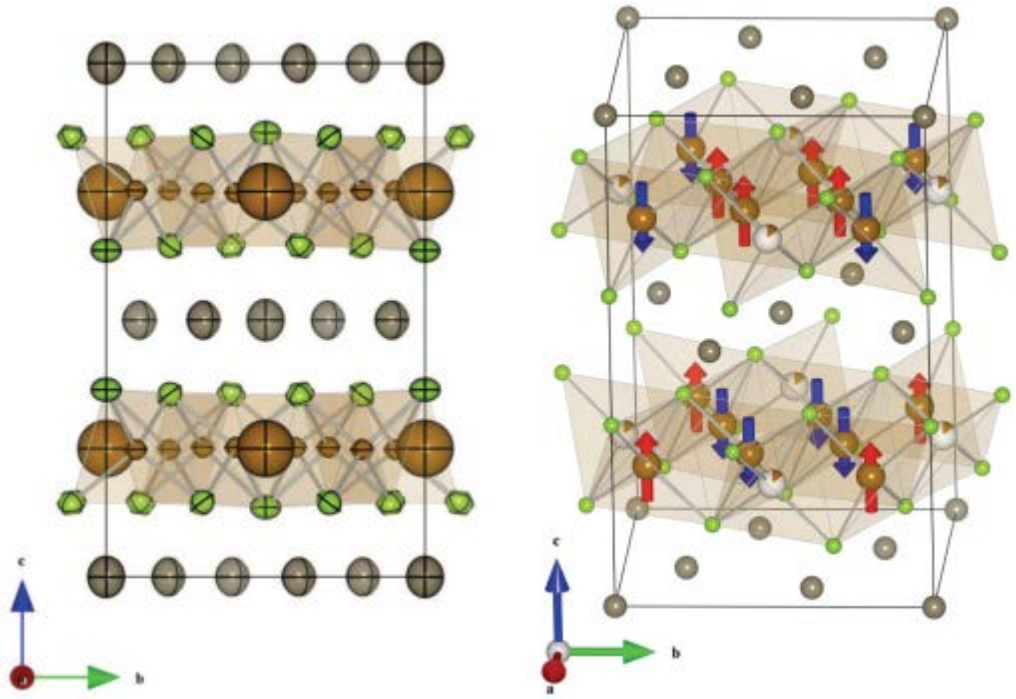

Figure 1.7. Image of $TlFe_{1.6}Se_2$ structure: Tl (gray), Se (green), and Fe (brown). The Fe spin orientations are illustrated in the second image.[32]

As mentioned, these materials display antiferromagnetic order. For $TlFe_{1.6}Se_2$, this magnetic ordering occurs at about 430K [32, 33]. The iron spins align antiferromagnetically along the c-axis in a block-checkerboard pattern below this temperature. These spins are

illustrated in both Figures 1.7 and 1.8a. However, interesting behavior has been observed in this material at low temperatures. In fact, two phase transitions have been evidenced at around 140K and 100K in heat capacity, magnetic susceptibility, electrical resistivity, and lattice parameter data [32, 33, 35].

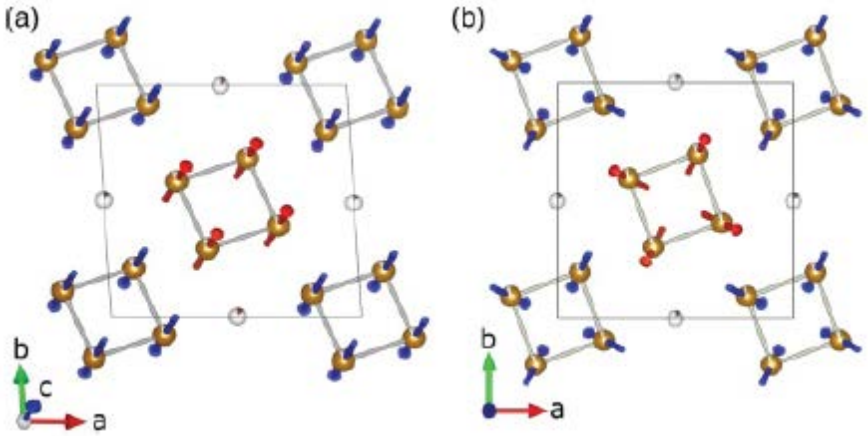

Figure 1.8. Illustration of the block-checkerboard antiferromagnetic order of $TlFe_{1.6}Se_2$ (a) iron moments above 140K and below 100K and (b) at 115K.[33]

Between 100K and 150K, a nonzero moment is observed in the ab-plane [33]. In this temperature range, it has been reported that the moments cant away from the c-axis as shown in Figure 1.8b. The angle of this moment from the c-axis is measured as 20° at 140K and 27° at 115K [33]. No change in the crystal symmetry is observed at these temperatures, but the lattice constants display interesting behavior in this temperature range [32]. In particular, the *c* lattice parameter exhibits a large jump at 100K [32, 33, 35]. At this temperature, the block-checkerboard antiferromagnetic structure with iron moments aligned along the c-axis is recovered; however, the magnetic moment is reduced. This value is suppressed from a maximum of $2.3\mu_B$ around 150K to $1.4\mu_B$ near 100K with the recovered magnetic structure [33].

Although this antiferromagnetic order is observed in conjunction with superconductivity in the $TlFe_{2-x}Se_2$ materials with lower x values (or higher 2-x values), it is believed that this coexistence is the result of very fine phase separation [30, 35]. It is thought that antiferromagnetism is displayed in the vacancy ordered regions, while superconductivity only occurs in paramagnetic regions of the material [30, 35]. These regions may drive more material to become superconducting due to large contact areas from the very fine phase separation. It has also been suggested that the superconducting phase consists of stoichiometric AFe_2Se_2 [30].

The studies of this material have mostly been conducted on crystals that have regions of vacancy order and disorder. The interactions between these different regions may have a large influence on the behavior of this material. In contrast to these crystals, a study on $TlFe_{1.6}Se_2$ samples that displayed complete vacancy ordering revealed a different magnetic ground state [35]. In this case, the spins reorient at around 100K so that the iron moments are aligned perpendicular to the c-axis.

1.3 Thermoelectric Materials

Thermoelectric materials have the potential to directly convert a temperature gradient into electrical energy or vice versa. In fact, all materials have a nonzero thermoelectric effect, but unlike most materials, so-called thermoelectric materials display a substantial effect. If a temperature gradient occurs across these materials, a voltage is generated that is proportional to this temperature difference. Thus, thermoelectric materials have attracted a lot of attention as a way to recover some of the energy lost to the environment in the form of heat. They are also of interest as solid-state refrigeration devices, and they have been employed as thermoelectric generators in space applications since the 1960s [36].

The efficiency of these materials to convert these types of energy is of great concern for practical application. In order to quantify the maximum efficiency of the conversion from temperature gradient to electrical energy, the thermoelectric figure of merit (ZT) is used. The material's figure of merit (unitless) is given by

$$ZT = \frac{\alpha^2 \sigma T}{\kappa} = \frac{\alpha^2 T}{\rho \kappa}. \quad (1.1)$$

The Seebeck coefficient is given as α, the electrical conductivity as σ, the temperature as T, and the total thermal conductivity as κ. The electrical conductivity may be replaced by the inverse of the electrical resistivity (ρ). Materials used in current applications have a ZT of about 1, but much higher values (3 to 4) are needed for improved efficiency.

From the equation, we can see that higher ZT values (higher efficiencies) result from a high Seebeck coefficient, high electrical conductivity, and low thermal conductivity. The Seebeck coefficient and electrical conductivity can be modified by doping and chemical composition. A variety of techniques are used to minimize the thermal conductivity and optimize the ZT. Low thermal conductivity is crucial to the effectiveness of thermoelectric materials because the temperature gradient that produces the thermoelectric voltage must be preserved. The propagation of phonons needs to be hindered in order to maintain low thermal conductivity, and the following techniques have been used in development of materials with low thermal conductivity: mass disorder due to alloying, rattling ions in large complex unit cells, and nanoscale structure [37-40].

Although there are many useful techniques to improve ZT by reducing the thermal conductivity, making these customized materials is difficult, and there are some concerns about their thermal stability. Therefore, materials with inherently low thermal conductivity are desired. In general, the ideal materials for thermoelectric applications are narrow-bandgap

semiconductors that have high-mobility carriers, low carrier concentration, and a minimized lattice thermal conductivity [41].

Though the efficiency of thermoelectric materials is a concern, these materials offer many advantages. The most obvious benefit of thermoelectric devices is the ability to recover some of the waste heat that would otherwise be an energy loss. These devices are also quite small and lightweight, and they can be inexpensive. They contain no moving parts, so maintenance is minimal and reliability is good. Furthermore, they have the ability to provide localized cooling (or heating).

1.4 Mo_3Sb_7 Thermoelectric Material

Mo_3Sb_7 is a promising thermoelectric material. This material has a complex crystalline structure (illustrated in Figure 1.9) that lends itself to low thermal conductivity. It is also possible to tune the electrical properties with chemical substitutions to improve ZT. Furthermore, Mo_3Sb_7 has some practical advantages: it is non-toxic and relatively inexpensive [42], both important considerations for practical application.

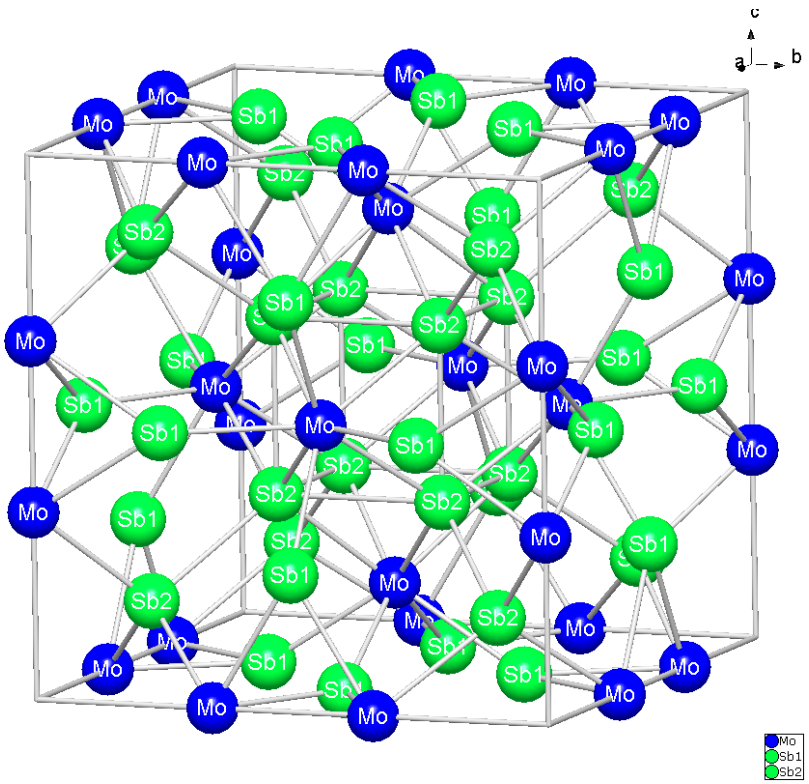

Figure 1.9. Image of Mo_3Sb_7 unit cell (space group Im-3m).[43]

At low temperatures, this material displays some interesting behavior involving magnetic interactions, structural instability, and superconductivity. The parent Mo_3Sb_7 compound displays a few transitions at low temperature. At around 53K, there exists a cubic-to-tetragonal structural transition [44, 45]. It is believed that this structural transition is the result of antiferromagnetic interactions between nearest-neighbors and next-nearest-neighbors, and this frustration is relieved by the transition to a tetragonal structure [45]. Also around 53K, there have been reports of a spin-gap formation [46-49]. At about 2.35K, Mo_3Sb_7 undergoes a transition to become a bulk type-II superconductor [50].

Mo_3Sb_7 is a poor metal and must be altered in order to improve its thermoelectric properties. This is often done by doping with ruthenium on the molybdenum site or tellurium on the antimony site [42, 44-48]. Both ruthenium and tellurium doping add extra electrons. Figures

1.10 and 1.11 display the thermoelectric figure of merit as a function of temperature for Mo_3Sb_7 materials that have been doped with ruthenium and tellurium, respectively. The figures reveal the improved thermoelectric properties with the addition of these elements. The transitions in the Mo_3Sb_7 series are also affected by doping. The addition of either ruthenium (3at%) or tellurium (0.3at%) results in the suppression of the cubic-to-tetragonal phase transition, and these additions also decrease the superconducting transition (T_c) [44]. The T_c for the ruthenium-doped material is shifted to 2.15K, and the T_c for the tellurium-doped material is shifted to 2.05K. From these results, it appears that the structural transition, which is very sensitive to ruthenium and tellurium doping, is not required for superconductivity to emerge. Furthermore, it has been suggested that these dopings slightly decrease the magnitude of the spin gap [45].

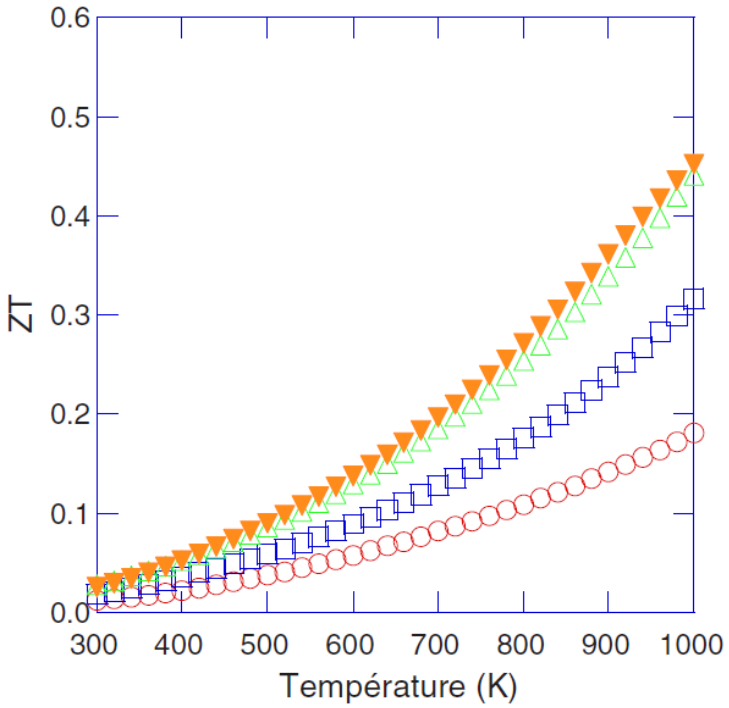

Figure 1.10. Thermoelectric figure of merit as a function of temperature for Mo_3Sb_7 (○), $Mo_{2.75}Ru_{0.25}Sb_7$ (□), $Mo_{2.5}Ru_{0.5}Sb_7$ (Δ), and $Mo_{2.2}Ru_{0.8}Sb_7$ (▽).[46]

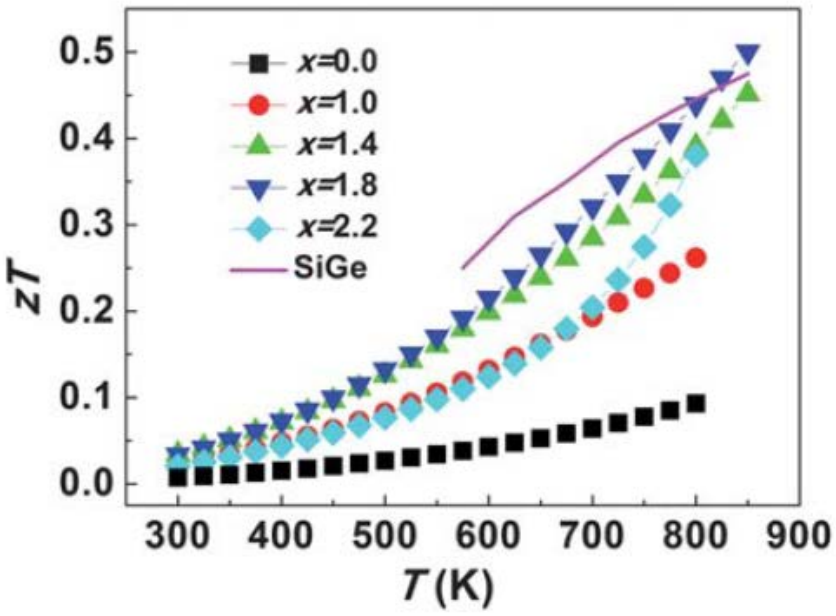

Figure 1.11. Thermoelectric figure of merit as a function of temperature for Mo_3Sb_7 (■), Mo_3Sb_6Te (●), $Mo_3Sb_{5.6}Te_{1.4}$ (▲), $Mo_3Sb_{5.2}Te_{1.8}$ (▼), and $Mo_3Sb_{4.8}Te_{2.2}$ (◆) with SiGe for reference.[42]

The effect of chromium (3at%) doping has also been examined. Unlike ruthenium and tellurium, the addition of chromium does not prevent the structural transition, but it does decrease the transition temperature by about 5K. It does, however, affect the superconducting transition. The material does not become superconducting above 1.8K, the lowest temperature at which it was measured [44].

Chapter 2

Experimental Details

2.1 Resonant Ultrasound Spectroscopy (RUS)

Resonant ultrasound spectroscopy (RUS) is an innovative technique based on the relation between a material's resonant frequencies and its elastic tensor. The RUS technique examines the mechanical response of a solid, freely-vibrating sample as an ultrasonic wave is applied. Because these mechanical resonances are directly related to the elastic constants of the material, this technique can be used to determine the material's full elastic tensor [51-53]. RUS can be used on either isotropic polycrystals or single crystals with various symmetries.

2.1.1 Development

Mechanical resonances have been utilized to investigate materials since the 19th century. Though these applications were rather superficial, it was observed that defects, such as cracks, change the resonance spectra, and sound could be used to examine the quality of manufactured parts. Analytic solutions for calculating the resonant frequencies of isotropic samples in terms of elastic constants and sample shape, size, and mass were developed around 1880 by Gabriel Lamé and Horace Lamb [53]. These solutions were developed for samples having cubic or spherical shapes. It was not until 1964 that D.B. Frasier and R.C. LeCraw performed what has been credited as the first RUS measurement [53] when they used a single transducer setup to calculate the elastic constants for a sphere of isotropic material [54]. Much of the credit for the development of RUS lies within the geophysics community. Development of this technique was driven by the need to accurately measure the elastic moduli of the Earth's constituent materials using the Earth's free-oscillation modes resulting from a major earthquake. A group of geophysicists including Orson Anderson, Naohiro Soga, and Edward Schreiber improved upon

the previous work of Frasier and LeCraw, eventually coining the phrase “resonant sphere technique” (RST). Much attention was brought to this measurement technique in 1970 when Anderson and Schreiber measured spherical lunar samples with RST [55]. It was Anderson’s student, Harold Demarest, who made the next breakthrough regarding the development of RUS. Demarest developed the solution for computing elastic constants for an anisotropic crystalline material shaped as a rectangular parallelepiped with its faces corresponding to the principal crystallographic planes [56]. Demarest’s work, which he referred to as cube resonance technique, later became known as the rectangular parallelepiped resonance technique (RPR), which is still in use today. Demarest’s work was expanded upon by Ohno, who in 1976, used this technique for rectangular parallelepipeds of lower crystal symmetry [57]. It was in 1988 that RUS began to be developed into its present form. Aided by the availability of modern computers, Albert Migliori, along with John Sarrao and William Visscher, worked to improve the physical measurement as well as the computational methods [51, 58, 59]. They provided the general physics community with a powerful technique for the determination of elastic constants. These types of measurements were given the name of “resonant ultrasound spectroscopy,” and this term includes any technique where elastic constants are determined with ultrasonic resonance frequencies. With the availability of high-speed computers, it is now possible to measure the elastic constants of materials with a wide range of shapes and crystal symmetries, and in principal, this technique can be applied to any sample with known shape and crystal symmetry.

2.1.2 Principle of RUS

As mentioned earlier, the first part of the RUS problem to be solved was calculating the resonant frequencies of a sample given the values of the sample’s elastic constants, density,

dimensions, and crystal structure and orientation (if not isotropic). This is referred to as the direct problem, as illustrated in the diagram in Figure 2.1, and can be solved as an eigenvalue problem – see section 2.1.4. However, the power of RUS lies in its ability to do the reverse. Given the information about the sample (density, dimensions, and crystal structure and orientation), the resonant frequencies are then measured, and the elastic constants are calculated using an iterative procedure. This process is referred to as the inverse problem, also shown in Figure 2.1. In this case, the measured frequencies are compared to a set of calculated frequencies based on an initial estimate for the elastic constants. These initial estimates are then adjusted in an iterative procedure until the agreement between the measured frequencies and the calculated frequencies is optimized.

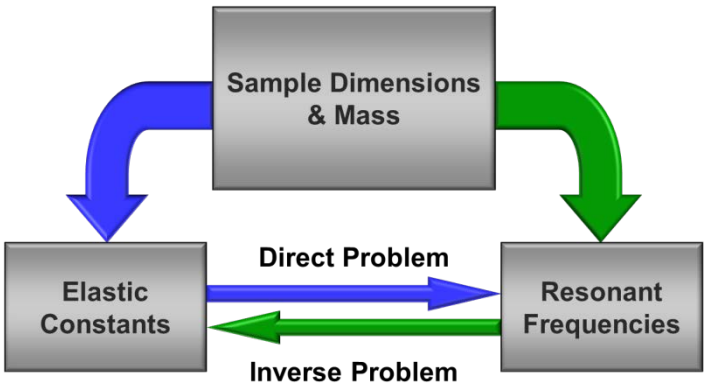

Figure 2.1. Block diagram illustrating the principle of RUS.

In order to locate the resonant frequencies of a given sample, a custom-built RUS probe, pictured in Figure 2.2, is used. The sample (generally on the order of a cubic mm) is mounted between two piezo-electric transducers. One transducer transmits an ultrasonic wave through the sample, and a second transducer detects the mechanical response of the sample, revealing the sample's resonant frequencies. The frequency is swept within a typical range of 100-2000 kHz,

and the response of the freely-vibrating sample is recorded as a function of frequency. The resonant frequencies, which are directly related to the elastic tensor, are examined in order to investigate the sample's elastic properties. Since many of the lowest-frequency resonances are strongly dependent on shear modes, a sufficient number of these resonances (dependent of sample symmetry) should be considered in order to represent non-shear behavior.

Figure 2.2. Image of the custom-built RUS probe.

As the frequency range is swept, a large response will be observed when this frequency corresponds to a resonant frequency for the sample. Figure 2.3 illustrates a partial resonance spectrum obtained using RUS. Each peak in this spectrum represents a resonant frequency for the sample, to be marked and recorded for use in the calculation of elastic constants. Because many more resonant frequencies, starting with the first and missing none, are required to calculate the elastic tensor, this spectrum is only a small portion of the spectra that is measured for RUS calculations. While data acquisition is fairly straightforward, data analysis can be quite complex, requiring an iterative fitting procedure to "match" the measured resonances with the calculated spectrum (section 2.1.5).

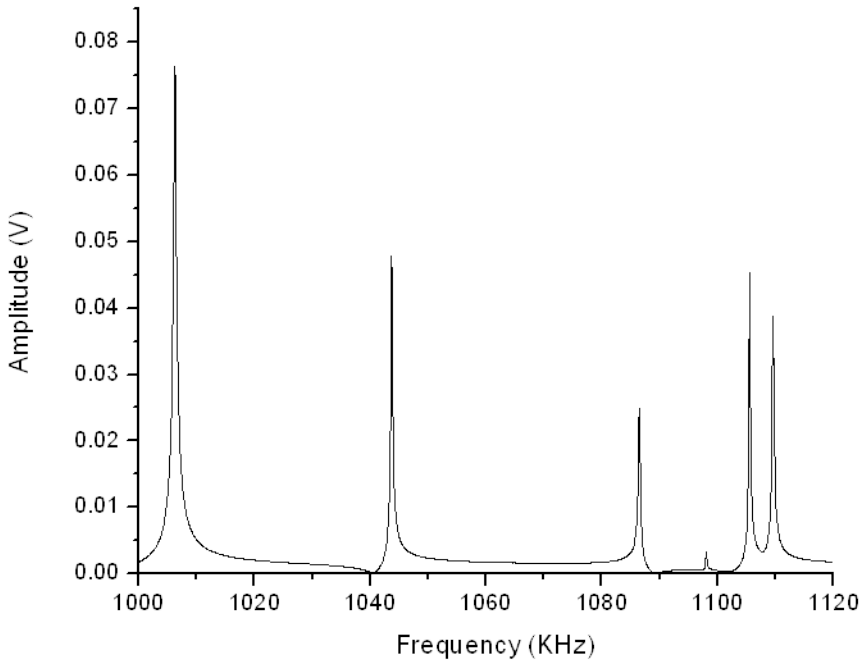

Figure 2.3. Partial resonance spectrum obtained using RUS.

2.1.3 Elastic Behavior

The primary purpose of RUS is the determination of elastic constants. These values are significant for the study of materials; they are directly related to the atomic bonding of the material and are closely related to a material's thermodynamic properties. Thus, they are particularly useful when examining phase transitions.

The application of an external force results in deformation of a material. If this force is sufficiently low, the material will remain in the linearly elastic region, meaning that the material will return to its original shape when the force is removed. A linear relationship between force and displacement exists for linear elasticity; this relationship is the well-known Hooke's Law:

$$\sigma_{ij} = C_{ijkl}\varepsilon_{kl}\,. \tag{2.1}$$

The applied stress is σ_{ij}, the elastic constants are C_{ijkl}, and the strain is ε_{kl}. The elastic constants for an object are arranged in a 9×9 matrix that is simplified using the following notation: 11→1, 22→2, 33→3, 23 and 32→4, 13 and 31→5, and 12 and 21→6. This produces a 6×6 elastic constant matrix with two subscripts for each elastic constant value, and Hooke's law appears as

$$\begin{pmatrix}\sigma_1\\ \sigma_2\\ \sigma_3\\ \sigma_4\\ \sigma_5\\ \sigma_6\end{pmatrix} = \begin{pmatrix} c_{11} & c_{12} & c_{13} & c_{14} & c_{15} & c_{16}\\ c_{12} & c_{22} & c_{23} & c_{24} & c_{25} & c_{26}\\ c_{13} & c_{23} & c_{33} & c_{34} & c_{35} & c_{36}\\ c_{14} & c_{24} & c_{34} & c_{44} & c_{45} & c_{46}\\ c_{15} & c_{25} & c_{35} & c_{45} & c_{55} & c_{56}\\ c_{16} & c_{26} & c_{36} & c_{46} & c_{56} & c_{66}\end{pmatrix}\begin{pmatrix}\varepsilon_1\\ \varepsilon_2\\ \varepsilon_3\\ \varepsilon_4\\ \varepsilon_5\\ \varepsilon_6\end{pmatrix}. \tag{2.2}$$

There are 21 independent elastic constants shown in this matrix, which is the elastic constant tensor for a triclinic crystal. Because this crystal structure is the lowest symmetry, it has the most elastic constants. For other crystals, as the symmetry increases, the number of independent elastic constants decreases. For cubic crystals, only three independent constants remain: c_{11}, c_{12}, and c_{44}. Further, isotropic crystals only have two independent elastic constants: c_{11} and c_{44}.

For RUS measurements, the sample may exhibit elastic deformation as the stress wave is applied. This deformation occurs as mode displacements, and some of the normal modes of vibration are seen in Figure 2.4 for an anisotropic rectangular parallelepiped. These mechanical responses can be complex; they depend on the elastic constants and sample shape, density, crystal structure and orientation. As will be seen, RUS relies on the ability to efficiently calculate these resonant frequencies.

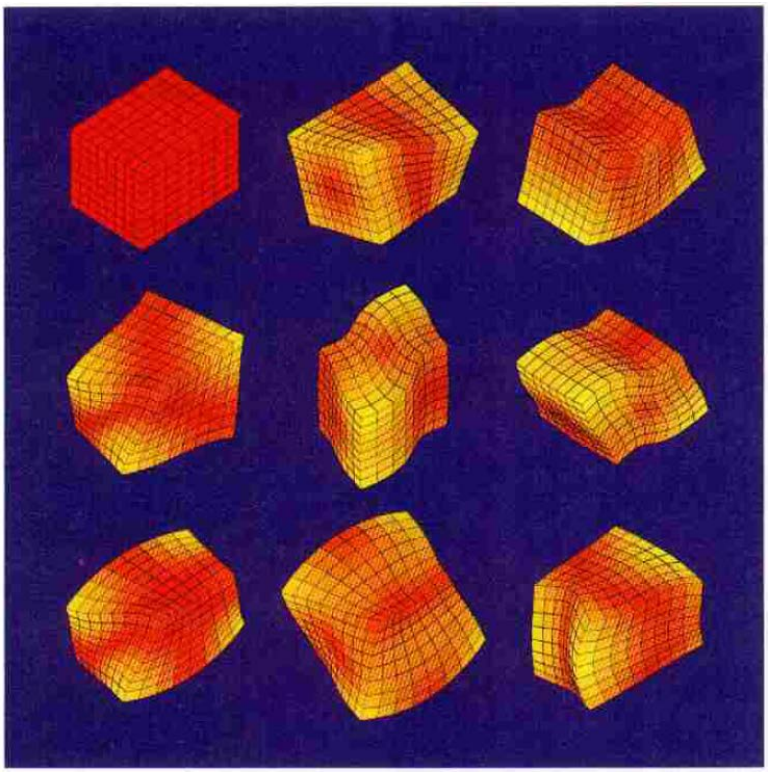

Figure 2.4. Images of several normal modes of vibration for a rectangular parallelepiped.[53]

2.1.4 Calculation of the Direct Problem

The essential component to RUS is the ability to quickly calculate the resonant frequencies of a well-defined sample. The equilibrium configuration of the system occurs at the minimum of the Lagrangian. Because this procedure involves solving for the stationary points of

the mechanical Lagrangian with free-surface boundary conditions, the determination of the resonant frequencies begins with consideration of the general form of the Lagrangian L

$$L = \int_V (\mathrm{KE} - \mathrm{PE}) dV \,. \tag{2.3}$$

Here KE and PE are the kinetic energy and the potential energy, respectively. The Lagrangian minimization procedure involves minimizing the difference between these two quantities over the sample volume. The kinetic and potential energies for an arbitrarily shaped elastic solid with volume V in a free surface S and with linear elastic tensor C_{ijkl} and density ρ are

$$\mathrm{KE} = \frac{1}{2} \sum_i \rho \omega^2 u_i^2 \tag{2.4}$$

and

$$\mathrm{PE} = \frac{1}{2} \sum_{i,j,k,l} C_{ijkl} \frac{\partial u_i}{\partial x_j} \frac{\partial u_k}{\partial x_l}, \tag{2.5}$$

respectively. Here, ω is the angular frequency, and u_i is the ith component of the displacement vector. For both kinetic and potential energy expressions, the summation on i ranges from 1 to 3, corresponding to the x, y, and z directions.

As mentioned, the equilibrium configuration of the system corresponds to the minimum of the Lagrangian. Therefore, finding this minimum is the start to finding the stationary points of the Lagrangian. We let u vary arbitrarily in V and on S ($u_i \rightarrow u_i + \delta u_i$), in order to find the minimum of the Lagrangian

$$L + \delta L = \int_V \left[\frac{1}{2} \sum_i \rho \omega^2 (u_i + \delta u_i)^2 - \sum_{i,j,k,l} C_{ijkl} \frac{\delta (u_i + \delta u_i)}{\delta x_j} \frac{\delta u_k}{\delta x_l} \right] dV \,. \tag{2.6}$$

Keeping terms to first order in δu_i

$$\delta L = \int_V \left[\sum_i \rho \omega^2 u_i \delta u_i - \sum_{i,j,k,l} C_{ijkl} \frac{\delta (\delta u_i)}{\delta x_j} \frac{\delta u_k}{\delta x_l} \right] dV \tag{2.7}$$

and integrating by parts yields

$$\delta L = \int_V \left(\sum_i \left[\rho\omega^2 u_i + \sum_{j,k,l} C_{ijkl} \frac{\partial^2 u_k}{\partial x_j \partial x_l} \right] \delta u_i \right) dV - \int_S \left(\sum_i \left[\sum_{j,k,l} \vec{n}_j \, C_{ijkl} \frac{\partial u_k}{\partial x_l} \right] \delta u_i \right) dS \, . \qquad (2.8)$$

The stationary points of the Lagrangian occur when δL is equal to zero. Thus, the values of u_i that correspond to these stationary points must be such that the terms in the square brackets above are zero since δu_i is arbitrary in V and on S. When the first term in brackets is set equal to zero, the following elastic wave equation is formed:

$$\rho\omega^2 u_i + \sum_{j,k,l} C_{ijkl} \frac{\partial^2 u_k}{\partial x_j \partial x_l} = 0 \, . \qquad (2.9)$$

An expression of free-surface boundary conditions is given by setting the second bracketed term to zero

$$\sum_{j,k,l} \vec{n}_j \, C_{ijkl} \frac{\partial u_k}{\partial x_l} = \sum_j \vec{n}_j \, \sigma_{ij} = 0 \qquad (2.10)$$

where the product of the elastic tensor C_{ijkl} and the strain $\partial u_k / \partial x_l$ is replaced with σ_{ij}, the ij th component of the stress tensor.

When these two conditions are satisfied, a simple result arises. The resulting set of u_i consists of those displacements that correspond to ω being one of a discrete set of normal mode frequencies of free vibration of the system.

We expand the displacement vector in a complete set of functions $\{\Phi_\lambda\}$ using the Rayleigh-Ritz method:

$$u_i = \sum_\lambda a_{i\lambda} \Phi_\lambda \, . \qquad (2.11)$$

For Φ_λ, we set powers of Cartesian coordinates:

$$\Phi_\lambda = x^l y^m z^n \qquad (2.12)$$

where λ = (l,m,n) is the function label, a set of three nonnegative integers. By substituting Equation 2.11 in Equation 2.3 and converting to a matrix equation, we find

$$L = \frac{1}{2}\omega^2 \vec{a}^T \overleftrightarrow{E} \vec{a} - \frac{1}{2}\vec{a}^T \overleftrightarrow{\Gamma} \vec{a} \tag{2.13}$$

where a is a vector with elements a_i whose transpose is a^T. Here, E and Γ are matrices, and their order is determined by the following truncation condition:

$$l + m + n < N \tag{2.14}$$

with

$$R = \frac{3(N+1)(N+2)(N+3)}{6}. \tag{2.15}$$

While the value of N should approach ∞ in order to approach an exact solution to Equation 2.13, this number must be restricted when considering the required computing time and memory. It has been observed that an N of 10 provides a good compromise between the accuracy and the computing power required.

The matrices E and Γ in Equation 2.13 have elements

$$E_{\lambda i \lambda' i'} = \delta_{ii'} \int_V \Phi_\lambda \rho \Phi_{\lambda'} dV \tag{2.16}$$

and

$$\Gamma_{\lambda i \lambda' i'} = \sum_{j,j'} C_{ijj'i'} \int_V \frac{\partial \Phi_\lambda}{\partial x_j} \frac{\partial \Phi_{\lambda'}}{\partial x_{j'}} dV\,, \tag{2.17}$$

respectively.

When the displacements u_i are solutions of the free-vibration problem, the Lagrangian is stationary. The solutions of this free-vibration problem are found by setting the derivatives of Equation 2.13 with respect to each of the R amplitudes $a_{i\lambda}$ equal to zero. The following eigenvalue equation results:

$$\omega^2 \overleftrightarrow{E}\vec{a} = \overleftrightarrow{\Gamma}\vec{a}\,. \tag{2.18}$$

The solution of this equation provides both the resonant frequencies in the form of the eigenvalues and the physical displacements during oscillation in the form of the eigenvectors.

2.1.5 Application to the Inverse Problem

The fundamental aspect of RUS is the comparison of experimentally measured resonant frequencies to calculated resonant frequencies in order to determine the elastic tensor for a given sample. Using the procedure described in the previous section, a computer generates a theoretical spectrum of resonant frequencies that are based on the following input parameters: the elastic constants, the crystal structure and orientation, and the sample's shape, dimensions, and mass. Naturally, the elastic constants are not known, as they are the values that are being quantified. However, the operator inputs an initial estimate for these values to begin the iteration procedure. The other input parameters are typically known. The computer then compares the calculated spectrum of resonances with the experimentally-determined resonances and tries to match these two spectra by adjusting the values of the elastic constants which are used to create the calculated list. The computer will repeat this procedure, creating new spectra with different elastic constants until the difference between the two spectra is minimized. The comparison between the calculated spectrum and the experimentally-determined spectrum is represented by the root-mean-square error, σ_{RMS}:

$$\sigma_{RMS} = 100 \times \sqrt{\frac{1}{N}\sum_{i=1}^{N}\left(\frac{g_i - f_i}{f_i}\right)^2}\ \% \tag{2.19}$$

where g_i is the measured frequency, and f_i is the calculated frequency. The measured frequencies and the best-fit calculated frequencies are compared in order to determine the quality of the RUS fit. If this σ_{RMS} value is approximately 0.5% or less, the calculated elastic constants are generally

believed to accurately represent the sample. If this value is higher, the input values need to be re-evaluated or the data should be examined for any overlooked resonant frequencies. Also, the sample quality should be examined. Multiple samples of the same material should be measured to ensure that the fitting procedure did not settle on a false minimum.

2.1.6 Output

As these calculations are performed with the RPR program, RUS output files are developed. An example of such a file is provided in Figure 2.5. This output file begins with a title to identify the sample and temperature. Based on the crystal symmetry and sample shape, the second line lists the independent elastic constants and the orientation of the sample. The third line indicates the order of the polynomial used in the fitting procedure followed by the mass of the sample and the density calculated from the given mass and dimensions. The parameters listed in this header are inputs provided by the user.

```
Mo2.91Ru0.09Sb7_300.00K
free moduli are  c11, c12, c44, cut along 100
using 10 order polynomials    mass=  0.0099 gm  rho= 8.614 gm/cc

 n     fex      fr    %err wt k i    df/d(moduli)
  1 0.993573 0.989577 -0.40 1.00 4 1 0.02-0.01 0.99
  2 1.087342 1.090708  0.31 1.00 6 2 1.45-0.60 0.15
  3 1.124204 1.125951  0.16 1.00 7 2 1.44-0.59 0.15
  4 1.382498 1.392184  0.70 1.00 5 1 1.78-0.78 0.00
  5 1.579051 1.588413  0.59 1.00 4 2 0.13-0.06 0.93
  6 1.600185 1.592966 -0.45 1.00 3 2 0.28-0.12 0.83
  7 1.637674 1.644571  0.42 1.00 2 2 0.46-0.20 0.74
  8 1.708246 1.704687 -0.21 1.00 5 2 1.77-0.80 0.02
  9 1.741304 1.731326 -0.57 1.00 8 2 0.73-0.30 0.57
 10 1.754639 1.750257 -0.25 1.00 1 2 1.63-0.72 0.09
 11 1.784100 1.784158  0.00 1.00 6 3 1.23-0.44 0.21
 12 1.860663 1.869241  0.46 1.00 5 3 1.83-0.83 0.00
 13 1.939524 1.949159  0.50 1.00 2 3 1.01-0.40 0.38
 14 1.963543 1.962168 -0.07 1.00 8 3 0.16-0.07 0.91
 15 1.985461 1.994600  0.46 1.00 7 3 1.24-0.46 0.22
 16 2.007021 2.003685 -0.17 1.00 8 4 0.09-0.02 0.92
 17 2.085465 2.081173 -0.21 1.00 3 3 1.24-0.52 0.27
 18 2.096919 2.101910  0.24 1.00 1 3 1.66-0.75 0.09
 19 2.147844 2.132789 -0.70 1.00 5 4 1.38-0.47 0.09
 20 2.167632 2.162432 -0.24 1.00 1 4 1.47-0.57 0.11
 21 2.242626 2.226404 -0.72 1.00 5 5 1.58-0.60 0.02
 22 2.279143 2.270096 -0.40 1.00 6 4 1.09-0.46 0.37
 23 2.300074 2.283345 -0.73 1.00 7 4 1.15-0.49 0.34
 24 2.334740 2.326885 -0.34 1.00 1 5 1.38-0.56 0.17
 25 2.396558 2.412900  0.68 1.00 4 3 0.30-0.09 0.79
 26 2.424857 2.428501  0.15 1.00 1 6 1.25-0.47 0.22
 27 2.433303 2.441643  0.34 1.00 3 4 1.00-0.42 0.42
 28 2.448810 2.442230 -0.27 1.00 7 5 0.60-0.22 0.62
 29 2.464553 2.459852 -0.19 1.00 2 4 0.87-0.37 0.49
 30 2.482179 2.486971  0.19 1.00 6 5 0.45-0.16 0.71
 31 2.613262 2.603642 -0.37 1.00 2 5 0.67-0.25 0.58
 32 2.668790 2.654950 -0.52 1.00 3 5 0.82-0.31 0.49
 33 2.768562 2.775538  0.25 1.00 4 4 0.54-0.25 0.70
 34 2.774262 2.791451  0.62 1.00 5 6 1.11-0.23 0.11
 35 2.808974 2.814418  0.19 1.00 6 6 0.70-0.31 0.60
 36 2.830840 2.834531  0.13 1.00 7 6 1.16-0.51 0.34
 37 2.835526 2.838533  0.11 1.00 5 7 1.09-0.45 0.36
 38 2.900304 2.906846  0.23 1.00 4 5 0.84-0.36 0.51

Bulk Modulus=     1.204

   c11     c22     c33     c23     c13     c12     c44     c55     c66
 1.8894  1.8894  1.8894  0.8613  0.8613  0.8613  0.7482  0.7482  0.7482

      d1       d2       d3
  0.13521  0.09613  0.08842

 loop# 3  rms error=  0.4082 %, changed by 0.0000003 %

 length of gradient vector=  0.000001  blamb=  0.000000

 eigenvalues          eigenvectors
      0.03868   0.67 0.42 0.61
      5.42581   0.74-0.39-0.55
     15.15748  -0.01-0.82 0.58

chisquare increased 2% by the following % changes in independent parameters
  0.91  2.20 -0.03
  0.05 -0.10 -0.24
  0.04 -0.08  0.10
```

Figure 2.5. Example of an RUS output file.

The table that follows the header begins with the ordered number of each resonant frequency; this column is labeled as *n*, and there are 38 resonant frequencies listed in the example file. The second column lists locations of the experimentally-determined resonant frequencies observed in the resonant spectra, *fex*. As mentioned earlier, every resonant frequency starting with the first must be included in this list up to a sufficient number of frequencies. The third column provides the calculated frequencies, *fr*, that result from the iterative fitting procedure. This list is followed by the percent difference between the experimentally-determined resonant frequencies and the calculated resonant frequencies from the two previous columns. This difference is identified as *%err*. The *wt* value determines whether each resonant frequency in the list is used in the determination of the elastic constants. A value of 1.00 indicates that this measured frequency is used in the calculation, and a value of 0.00 indicates that it is not. A value of 0.00 in the *wt* position acts as a place holder and allows the calculation to proceed without considering the experimentally-determined value for that particular resonant frequency. In the example file, all experimentally-determined resonant frequencies influence the calculation because each *wt* value is set to 1.00. The *k* and *i* values identify the mode; the *k* column describes the symmetry of each mode, and the *i* column describes the order of each mode. The final three columns are labeled collectively as *df/d(moduli)*. These values indicate how each of the resonant frequencies depends on the independent elastic constants. The three columns represent the independent elastic constants in the same order that they are listed in the header. In other words, for the example given in Figure 2.5, the first column in the *df/d(moduli)* section reveals the dependence on c_{11}, the second column reveals the dependence on c_{12}, and the last column reveals the dependence on c_{44}.

Below this table, the bulk modulus is given followed by the calculated elastic constants. Because the sample used for Figure 2.5 is cubic, $c_{11} = c_{22} = c_{33}$, $c_{23} = c_{13} = c_{12}$, and $c_{44} = c_{55} = c_{66}$. The three dimensions of the rectangular parallelepiped sample are then listed, followed by the number of iterations the program performed. The rms error of the current fit is then listed as well as the percentage that this value changed after the previous iteration. This file also provides information about the fit's accuracy. The three columns at the end of the file correspond to the variables listed in the header. For the example, the first column corresponds to c_{11}, the second corresponds to c_{12}, and the third corresponds to c_{44}. The largest value in each column provides an error value for each variable. The errors listed in the example are typical for RUS measurements. Error values for the compressional constants are generally on the order of 1%; for the shear constants, these values are less than a percent, and they are generally on the order of 2% for off-diagonal constants.

2.1.7 Sample Preparation

Because the relationship between the elastic tensor and the resonance frequencies is not a simple one, the geometry of the sample is simplified to facilitate calculations. Samples are generally shaped into rectangular parallelepipeds, spheres, or cylinders for measurement; these shapes can be described by a few mathematical functions. While all three geometries are simple and practically useful, rectangular parallelepipeds are often used because the preparation of these samples is fairly straightforward. These rectangular parallelepipeds are not perfect cubes because the cubic shape leads to a degeneracy of the resonant frequencies.

In order to fully examine single crystals with the RUS technique, the samples must be oriented and polished into rectangular parallelepipeds with all sides perpendicular to the main crystallographic directions. RUS is often used for single crystalline samples of orthorhombic or

higher symmetry. The sample preparation begins with examination of the crystal with X-ray Laue diffraction to determine the orientation of the single crystal. The sample is then cut along the major crystallographic planes. The sample faces are then polished and checked to ensure that the sides are parallel. (An acceptable sample will have faces parallel within 2° [51].) To minimize error, proper sample preparation is important when using this technique.

2.1.8 Temperature Dependence

For samples with irregular shape or symmetry lower than orthorhombic, the procedure for calculating the elastic moduli can be challenging, but RUS measurements can give important information even when it is not possible to obtain an absolute value for the elastic constants. Any deviation from "normal" thermodynamic behavior will be reflected in the temperature dependence of the resonant frequencies, and these can be measured regardless of sample shape or symmetry. An illustration of "normal" temperature dependence is provided in Figure 2.6. A sample that has no transitions will display this type of elastic response: the material gradually stiffens with decreasing temperature until it levels off at very low temperatures.

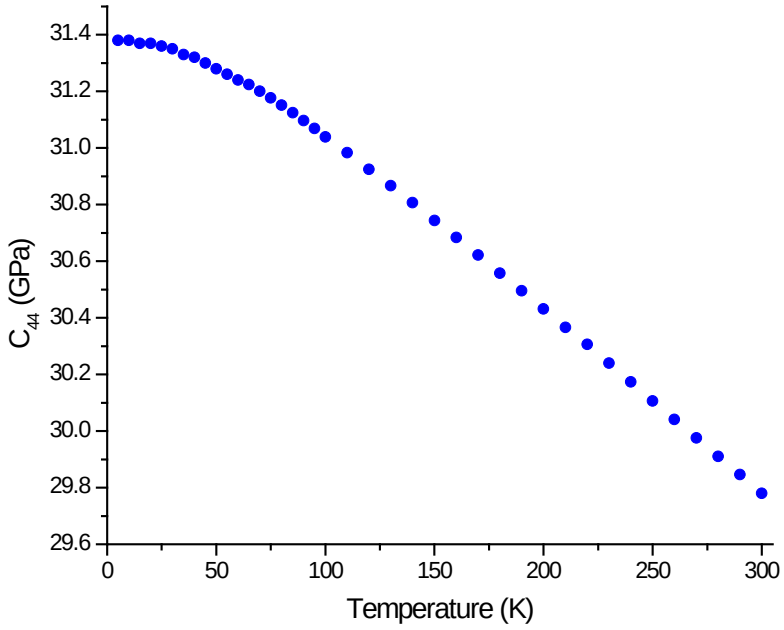

Figure 2.6. "Normal" temperature dependence of elastic constants.

In order to obtain the low-temperature data, a custom-built probe is used to carry out RUS measurements in a physical property measurement system (PPMS). This system provides a way to measure a material's elastic response as a function of temperature (2-400K) as well as its response in a magnetic field (0-9T). In addition, a modified VersaLab system has been used to perform some of the RUS measurements. This system provides a temperature range of 50-400K and can apply a magnetic field up to 3T without the use of liquid cryogens. The availability of this equipment has been very valuable in light of the recent liquid helium shortage.

As part of this research, a high-temperature RUS setup was also developed; this apparatus is pictured in Figure 2.7. The setup makes use of a Thermo Scientific precision high-performance oven that allows RUS measurements up to 600K. This oven is outfitted with a custom-built RUS probe and environmental chamber that can be loaded from the top of the oven.

The head of the probe contains two coaxial connectors for the RUS signal, a multi-pin connector for temperature readout, and 2 hose barbs used for environmental control. Once a sample is placed in the RUS probe, this probe is then lowered into the chamber inside the oven. The probe head and the sample chamber were designed with a flange joint, which is secured with a flange clamp. The chamber is flushed with argon gas before the measurement begins, and flowing argon gas is used throughout the measurement. As typical RUS equipment available in our lab is used at cryogenic temperatures, many typical components had to be exchanged. In particular, SiO_2 mineral-insulated coaxial cable from Thermocoax with a 1 mm diameter is used in place of the usual Teflon-coated coaxial cable, traditional adhesives are replaced with high-temperature vacuum sealant, and silver epoxy replaces the solder at electrical junctions. In order to determine the temperature of the sample, a platinum thermoresistor is placed on the probe in close proximity to the sample. A Lakeshore temperature controller is used to take the temperature readings, and a custom Labview program runs the RUS measurement and records the resonant spectra and temperature.

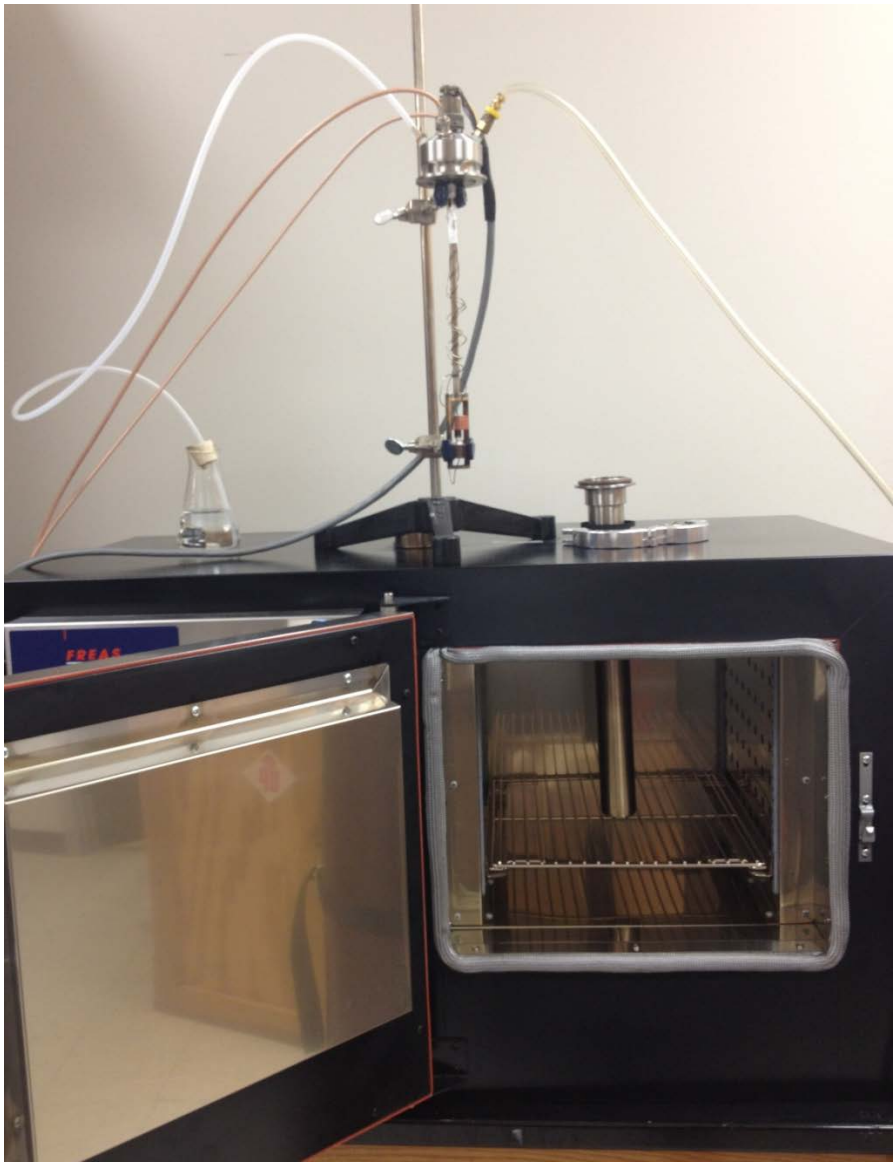

Figure 2.7. Image of high-temperature RUS setup.

2.1.9 Benefits

The RUS technique has a high inherent accuracy and has many advantages over conventional elastic constant measurements. Compared to RUS, traditional measurement techniques, such as the pulse-echo method, seem rather limited. The minimum sample size for RUS measurements is dramatically smaller. In fact, this minimum sample size, by volume, is

reduced by approximately three orders of magnitude when compared to traditional measurement techniques [60]. The use of smaller samples may help to reduce the amount of sample inhomogeneity in polycrystalline samples and reduces the amount of material needed for testing. While this reduction in sample size is often convenient, this smaller sample requirement is particularly important when measuring single crystals. Since single crystals are often limited in size, RUS can be used to look at a much wider range of single-crystalline materials. Also, no bond between the transducer and the sample is required; the sample simply rests between the transducers. Because of thermal expansion/contraction differences between the sample and the bonding agent, this is especially important when measuring the temperature dependence of the elastic constants. This difference in thermal expansion/contraction can cause either the bond to break or unwanted strains to be applied. Furthermore, with RUS, all of the elastic constants can be determined from a single measurement on a single sample. This factor is in sharp contrast to other techniques that require samples to be prepared for measurements along different crystalline directions and often require the use of more than one sample. In addition, the single measurement helps reduce extrinsic variations. RUS is also an attractive technique because it is nondestructive. The sample used for RUS can also be used for other measurements, an important consideration when dealing with precious materials or the need to rule out sample-dependent artifacts. Finally, RUS can be useful even when situations arise that prevent the calculation of the elastic tensor. Phase transitions can be observed as a function of temperature by simply examining the change in the frequency of the resonant frequencies as a function of temperature. Because the square of the frequency is proportional to the elastic constants, an irregularity in the elastic behavior can be observed as an irregular change in the frequency as a function of temperature.

RUS is heavily reliant on computer programs, and in the past, this has limited its use. Extracting the large amount of information contained in an RUS spectrum is not a simple task. Fortunately, recent advances in computer technology have alleviated this problem. Ordinary, modern-day computers are more than adequate for examining typical RUS data.

2.2 Sample Synthesis

In order to effectively study the iron-based superconductors with RUS, high-quality single crystals were grown. Single crystals of $BaFe_2As_2$ and related materials were grown using a self-flux growth technique. Due to the possible impurities that may occur when using a typical flux growth, a self-flux growth method is preferred. Single-crystal flux growth involves melting the components of the desired crystal in a chosen flux. The flux material must have a lower melting point than the crystal. The flux material and stoichiometric amounts of the crystal components are placed in a crucible together, a catch crucible is placed on top, and the crucibles are sealed in a quartz tube for heating. The mixture is heated until melted. The temperature is then lowered closer to the melting point of the crystal (but still well above the melting point of the flux material). The mixture is held at this temperature for some time and then removed from the furnace and decanted. If the correct temperatures, times, and mixtures are used, the flux will be decanted off, and several crystals will remain.

For the $BaFe_2As_2$ crystal growth, as well as related FeAs-based materials, a self-flux growth method is used. In this case, the binary FeAs material is first formed by slowly reacting high-purity iron and arsenic pieces. These elements (all elements are >99.9% from Alfa Aesar) are combined in a 1:1 ratio and placed inside a quartz tube which is then sealed under vacuum. The sealed material is then placed in a furnace and heated to 350°C at a rate of 100°C/hr and held for 1 hour followed by heating to 600°C at a rate of 30°C/hr. It is held at this temperature

for 10 hours and then heated to 1060°C at a rate of 60°C/hr. The material is held at this temperature for 5 hours before slowly cooling to room temperature. The solidified FeAs material is then removed from the tube and broken into pieces to be used for the flux growths.

Pieces of the FeAs flux are combined with elemental barium pieces with a ratio of Ba:FeAs = 1:5. (Because barium is very air sensitive, this work must take place in a glove box.) These materials are combined in an alumina crucible which is then placed in a quartz tube. A second alumina crucible is filled about two-thirds full with quartz wool and placed, inverted, inside the same quartz tube. This crucible acts as a catch crucible. The tube is then sealed with a partial atmosphere of argon, and placed in a furnace. The mixture for the $BaFe_2As_2$ parent material is heated to 1180°C at a rate of 400°C/hr and held for about 15 hours. It is then cooled slowly to 1090°C at a rate of 2°C/hr and held at this temperature for at least 48 hours. The material is then removed from the furnace at this temperature and quickly inverted in order to decant the remaining FeAs flux. The molten flux flows through the quartz wool in the catch crucible, and many plate-like single crystals are left in the growth crucible or on top of the quartz wool.

In order to make doped samples, other arsenide binary materials are made. In particular, CoAs and CrAs are formed in order to dope the parent material with cobalt or chromium. The method for making these binaries is similar to that for the FeAs binary; however, the temperature profiles are different. For both CoAs and CrAs, the material is heated to 350°C at a rate of 50°C/hr and held for 3 hours. It is then heated to 600°C at a rate of 30°C/hr and held for 10 hours followed by heating to 900°C at a rate of 30°C/hr and held for 15 hours before slowly cooling to room temperature for use in the flux growths.

In order to form $BaFe_{2-x}Co_xAs_2$ samples, the total ratio of Ba:flux is 1:5; however, the flux is now a combination of FeAs and CoAs. To produce a sample with nominal x of 0.1, the ratio of Ba:FeAs:CoAs is 1:4.75:0.25; for x of 0.22, this ratio is 1:4.45:0.55; for x of 0.56, this ratio is 1:3.6:1.4. The process and temperature profile for these materials is the same as that for the parent material.

The Ba:flux ratio is also 1:5 for $BaFe_{2-x}Cr_xAs_2$ materials. For a nominal x of 0.06, the ratio of Ba:FeAs:CrAs is 1:4.85:0.15; for x of 0.12, this ratio is 1:4.7:0.3; for x of 0.22, this ratio is 1:4.45:0.55. For the chromium-doped samples, the growth process is the same as that for the parent material, but the temperature profile must be changed. These materials are heated to 1230°C at a rate of 400°C/hr and held at this temperature for 13 hours. They are then cooled at a rate of 1.8°C/hr, and held at 1100°C for at least 48 hours, at which point they are removed from the furnace and the excess FeAs/CrAs flux material is decanted. Samples with higher chromium content were also grown with Ba:FeAs:CrAs ratios as follows: for x of 0.28, this ratio is 1:4.3:0.7; for x of 0.32, this ratio is 1:4.2:0.8; for x of 0.34, this ratio is 1:4.15:0.85; for x of 0.5, this ratio is 1:3.75:1.25; for x of 1, this ratio is 1:2.5:2.5. These materials were heated to 1230°C at a rate of 400°C/hr and held for 10 hours; they were then cooled to 1120°C and held for at least 48 hours followed by decanting of the excess flux material.

The self-flux growths described above yield multiple high-quality, plate-like single crystals. The geometric proportions of these crystals are typically a few millimeters in two dimensions and on the order of a tenth of a millimeter in the third dimension. Figure 2.8 is an image of some of the superconducting crystals grown for this study. These resulting crystals are partially oriented; the c-axis is aligned so that it is perpendicular to the plane of the plates. Thus, the [001] direction of the crystal lattice corresponds to the thin dimension of the crystal.

Figure 2.8. Image of $BaFe_2As_2$ single crystals grown for study.

The resulting crystals were examined with powder X-ray diffraction and energy-dispersive spectroscopy to determine the quality and composition of the crystals. Powder X-ray diffraction was performed using a Scintag XDS 2000 powder X-ray diffractometer in order to examine the phase purity and lattice constants of the crystals. Energy-dispersive X-ray spectroscopy (EDS) was accomplished with a JEOL JSM-840 scanning electron microscope in order to examine the chemical composition of the crystals. The samples were measured in multiple spots to confirm that the samples are uniform.

Our study of thermoelectric materials also used high-quality single crystals. These promising thermoelectric crystals, the Mo_3Sb_7 series, were grown with a similar technique in the Correlated Electron Materials Group at ORNL. However, unlike the superconducting growths, the thermoelectric material growths yielded three-dimensional single crystals.

Chapter 3

Results – Iron-based Superconductors

3.1 $BaFe_2As_2$

Following the self-flux growth method described in Chapter 2, single crystals of the $BaFe_2As_2$ parent material were grown using the facilities at ORNL. Each batch yielded several high-quality single crystals with plate-like geometry. The resulting crystals with tetragonal crystal symmetry ranged in size from 2-6 mm in the a-b plane and 0.1-0.2 mm in the c direction. Powder X-ray diffraction determined that these crystals were the desired $BaFe_2As_2$. In addition, X-ray Laue diffraction was used to orient these crystals for RUS measurements; this procedure was conducted with a Philips Materials Research Diffractometer. A backscattered Laue diffraction pattern for this material is provided in Figure 3.1. These reflections indicate that the sample is indeed single crystalline. Some of the single crystals measured were also oriented using a Bruker D2 Cryso bench-top crystal orientation analyzer.

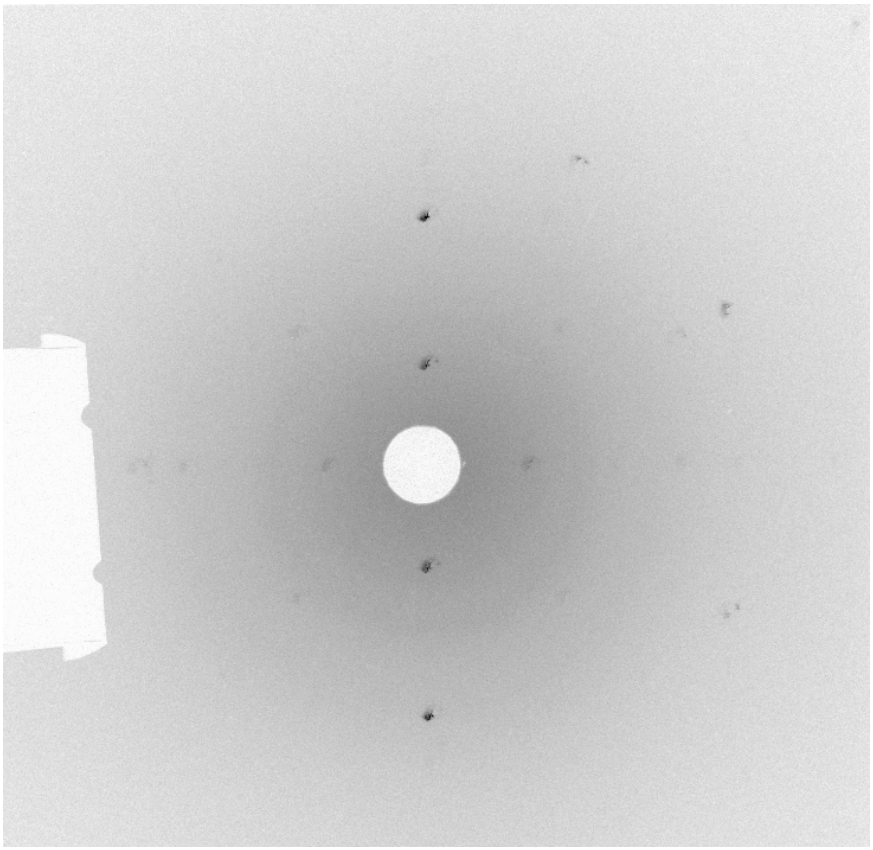

Figure 3.1. Backscattered Laue pattern for a $BaFe_2As_2$ sample.

RUS was used to study the elastic response of these crystals; however, the determination of the full elastic tensor was not possible. Despite much effort, the fitting procedure for this material was never completed to satisfaction. Much of the difficulty lies with the sample shape and properties. As mentioned earlier (also seen in Figure 2.8), the samples grow in a plate-like shape. Although this shape does not prohibit the use of RUS for calculating the elastic tensor, it does introduce plate modes that occur at lower frequencies than normal, and some of these modes may be missed when examining the resonant spectrum. A more prominent issue regarding the sample is the fact that it is very difficult to prepare a high-quality rectangular parallelepiped. While the thin dimension makes it challenging to polish the edges of the sample, the real problem occurs with the plane faces. These faces cannot be polished, and it is difficult to

cut the samples due to delamination of these faces. Even while using a wire saw at low speed, multiple layers of wax must be used to hold the sample to prevent the surface from delaminating. Furthermore, even gently polishing this face tends to destroy the sample. Beyond the sample preparation, the RUS signal for these materials is often unclear, and data analysis has proven to be complicated. Even with oriented single crystals that have been carefully prepared, there exist 6 independent elastic constants at room temperature and 9 independent elastic constants at low temperatures; selecting a good set of starting values is somewhat complex. The computation of these constants with an imperfect sample and poor signal has been elusive.

Fortunately, RUS can be used to examine the elastic behavior as a function of temperature without calculation of the elastic tensor. The temperature dependence of the resonant frequencies does reveal clear information about the elastic response of the crystal. As previously mentioned, resonant frequencies are directly proportional to the square root of the elastic constants. Thus, the frequency squared represents the change in the elastic response with temperature. Figure 3.2 displays a representative resonant frequency for the $BaFe_2As_2$ parent material as a function of temperature.

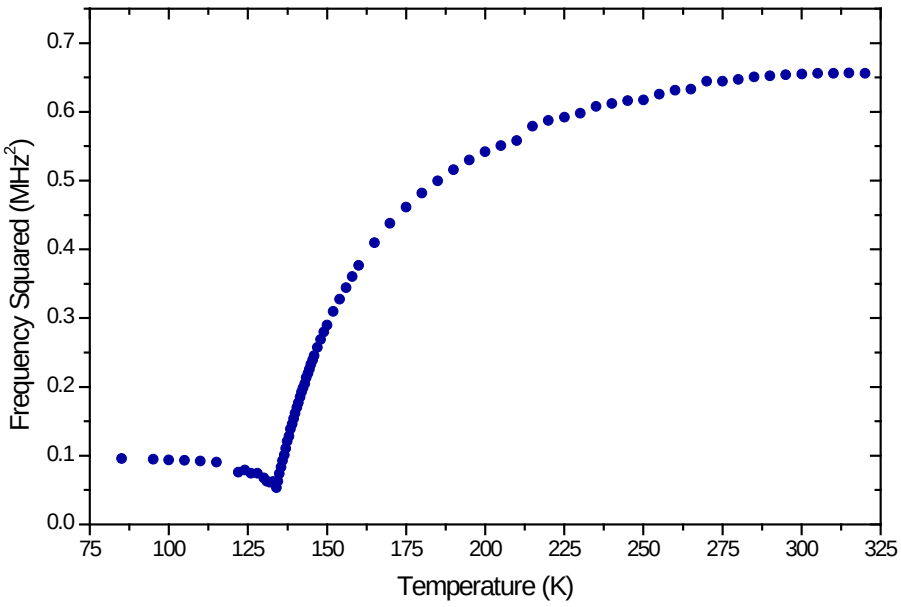

Figure 3.2. Resonant frequency of $BaFe_2As_2$ as a function of temperature.

The elastic response, represented as the frequency squared in Figure 3.2, of $BaFe_2As_2$ shows a considerable softening over a large temperature range upon cooling. Upon cooling, this softening becomes dramatic as the material approaches the associated structural (tetragonal-to-orthorhombic) and magnetic (antiferromagnetic spin-density-wave) phase transitions around 132K. This response is consistent with a dramatic softening often observed in the vicinity of structural transitions. Magnetic transitions may be observed in the elastic response as well, but the temperatures of the two transitions are too close to observe them separately for this sample. When the transition temperature is reached, the softening ceases. As the temperature is decreased below the transition temperature, gradual stiffening is observed.

While a large amount of softening is expected as the material approaches the joint, weakly first order structural and magnetic transitions, this data, along with data obtained in optimally cobalt-doped material (discussed later), is used to illustrate how magnetically-driven nematic fluctuations are responsible for inducing the structural transition [61]. There is no doubt

that strong magnetostructural coupling is prevalent in these materials. Although the structural transition and the antiferromagnetic transition follow each other closely, as can be seen in the partial phase diagrams in Figure 1.4 of Chapter 1, the structural transition temperature is either equal to the magnetic transition temperature or slightly higher. This relation between the transition temperatures would direct one to believe that the transition from tetragonal structure to orthorhombic structure occurs first and leads to the formation of antiferromagnetic order. It has been suggested, however, that this is not the case for some of these iron-based superconductors [62, 63]. Instead, spin fluctuations associated with the antiferromagnetic order bring about emergent nematic degrees of freedom at higher temperatures. The structure is affected because these nematic degrees of freedom couple to the lattice [64, 65]. This type of behavior had been predicted earlier [66].

As illustrated in Chapter 1, the antiferromagnetic phase of $BaFe_2As_2$ consists of antiferromagnetically aligned iron spins along one diagonal and ferromagnetically aligned iron spins along the second diagonal. An in-plane view of this antiferromagnetic state is shown in the left-hand panel of Figure 3.3. Because of the nematic order coupling to the lattice's elastic degrees of freedom, the orthorhombic fluctuations cause the bonds between neighboring parallel spins to contract and the bonds between neighboring antiparallel spins to expand. These changes are illustrated in the right-hand panel of Figure 3.3, where $\varphi > 0$ represents parallel spins, and $\varphi < 0$ represents antiparallel spins.

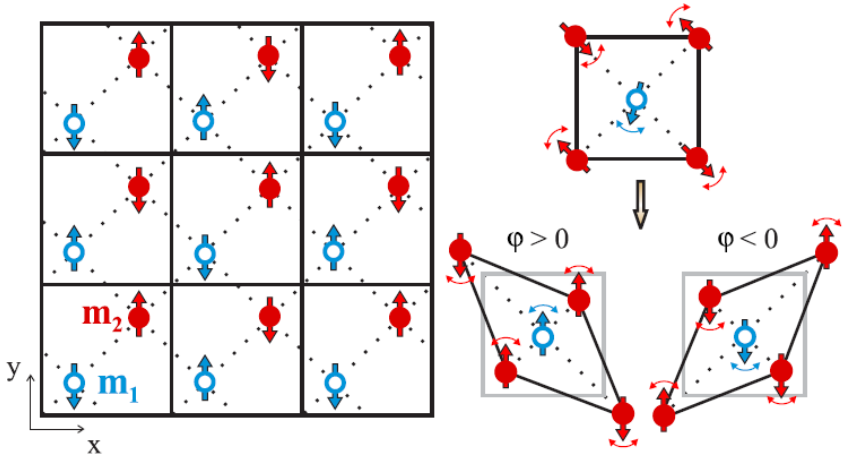

Figure 3.3. Illustration of (left panel) in-plane magnetic ordering of $BaFe_2As_2$ and (right panel) distortion of bonds between neighboring parallel ($\varphi > 0$) and antiparallel ($\varphi < 0$) spins.[61]

Due to this distortion, the orthorhombic fluctuation requires energy. This energy cost is characterized by the shear modulus, C_s, and in this case, C_s is defined as C_{66}. Though determination of the elastic tensor for this material remains elusive, information about this value can be extracted from the RUS data. Each resonant frequency is dependent on some combination of the independent elastic constants. (The high temperature tetragonal phase has six independent elastic constants.) Numerical simulations indicate that this shear mode c_{66} dominates several of the resonant frequencies [52], and from symmetry, the structural transition from tetragonal to orthorhombic necessitates that this shear mode go soft. The temperature dependences of more than twenty resonant frequencies were collected, and each showed similar behavior: a large amount of softening upon cooling as the material approached the transitions at about 132K and a slight stiffening beyond the transitions. With this information and because the resonant frequency squared is proportional to the elastic constants, the frequency squared of a characteristic resonant frequency is believed to represent the shear modulus well. Figure 3.4

displays this data along with a renormalization of the high-temperature shear modulus $C_{s,0}$ by nematic fluctuations calculated using the following:

$$C_s^{-1} = C_{s,0}^{-1} + \lambda^2 C_{s,0}^{-2} \chi_{nem}, \tag{3.1}$$

where λ is the magnetoelastic coupling and χ_{nem} is the nematic order parameter susceptibility which have been determined using a theoretical model outlined in Reference [61]. According to the equation, the nematic fluctuations soften the tetragonal material, and from Figure 3.4, this calculation agrees well with the RUS data.

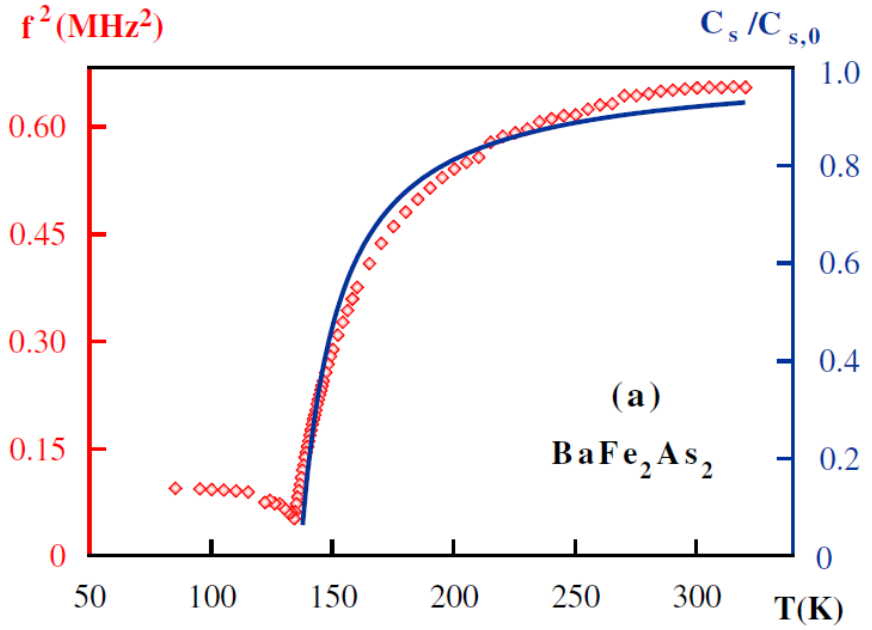

Figure 3.4. Temperature dependence of the resonant frequency squared (red data points) and the shear modulus calculated using Equation 3.1 (solid blue line) of the tetragonal phase of the parent material.[61]

The observed softening is well described by the magnetically-driven nematic fluctuations. In addition, it appears that nematic fluctuations occur over a large temperature range, as the material begins to soften near room temperature. These results support the assertion that the structural transition is induced by antiferromagnetic fluctuations occurring at

higher temperatures. In addition, a highly cobalt-doped $BaFe_2As_2$ material, discussed below, is examined with RUS to ensure that the features seen in this material and the superconducting material are not due to mechanical instability of the samples. As this highly-doped material does not undergo any low-temperature transitions, the RUS results simply show gradual stiffening with decreasing temperature.

3.1.1 $BaFe_{2-x}Co_xAs_2$

Single crystals of cobalt-doped $BaFe_2As_2$ were also examined with RUS. Cobalt doping is known to produce superconductivity in this material at the right concentrations, as indicated by the phase diagram provided in Figure 1.5. The addition of cobalt to $BaFe_2As_2$ electron dopes the FeAs layers, and superconductivity emerges for a range of cobalt concentrations. Samples were grown and measured representing three types of doping concentration: underdoped, optimally doped, and overdoped.

The term "underdoped" in this case identifies the material that has been cobalt doped, but this doping is less than that required to achieve the maximum superconducting transition temperature (T_c) for the $BaFe_{2-x}Co_xAs_2$ family of materials. This underdoped material has a nominal x value of 0.1; it displays the tetragonal-to-orthorhombic structural phase transition and antiferromagnetic ordering in addition to a superconducting transition at a lower temperature. A representative squared resonant frequency is provided in Figure 3.5 to illustrate the elastic behavior of this material. Like the parent material, a softening is evident as the material is cooled to the structural transition temperature, though for the underdoped material, this transition occurs around 70K because cobalt doping suppresses the structural and magnetic transition temperatures. Unfortunately, the RUS signal is not clear enough to continue tracking the resonant frequencies much below these transitions.

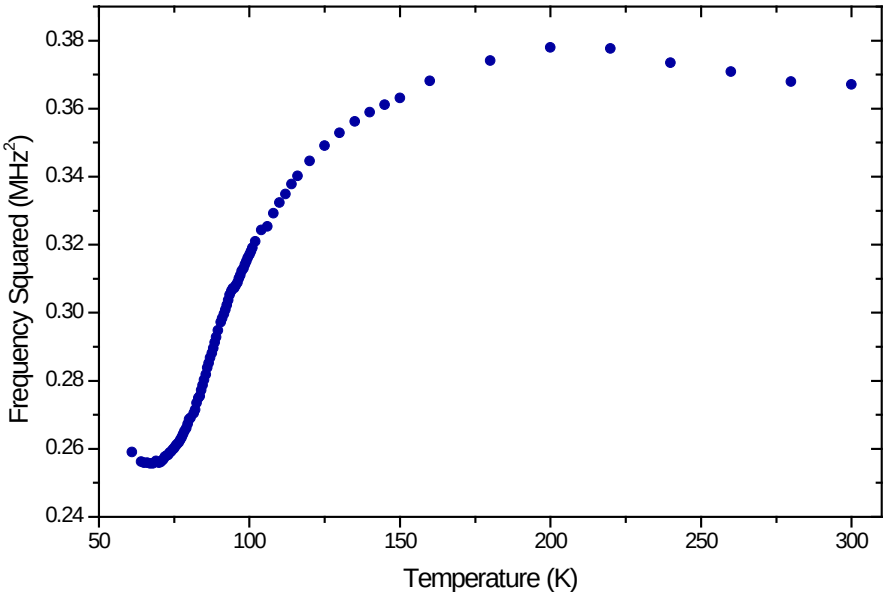

Figure 3.5. Temperature dependence of a representative resonant frequency squared for the underdoped material.

The optimally-doped material corresponds to the material with the highest T_c observed for the $BaFe_{2-x}Co_xAs_2$ series. In other words, the amount of cobalt doping coincides with the top of the superconducting dome from the phase diagram, and this material has a T_c of 22K. Also, this composition corresponds to a material in which the structural and magnetic transitions have been fully suppressed; the only low-temperature phase transition is the superconducting transition. Though the nominal value of x is 0.22, the actual x value for these samples is about 0.16, giving $BaFe_{1.84}Co_{0.16}As_2$. Figure 3.6 displays the temperature dependence of a representative resonant frequency squared for the optimally-doped material.

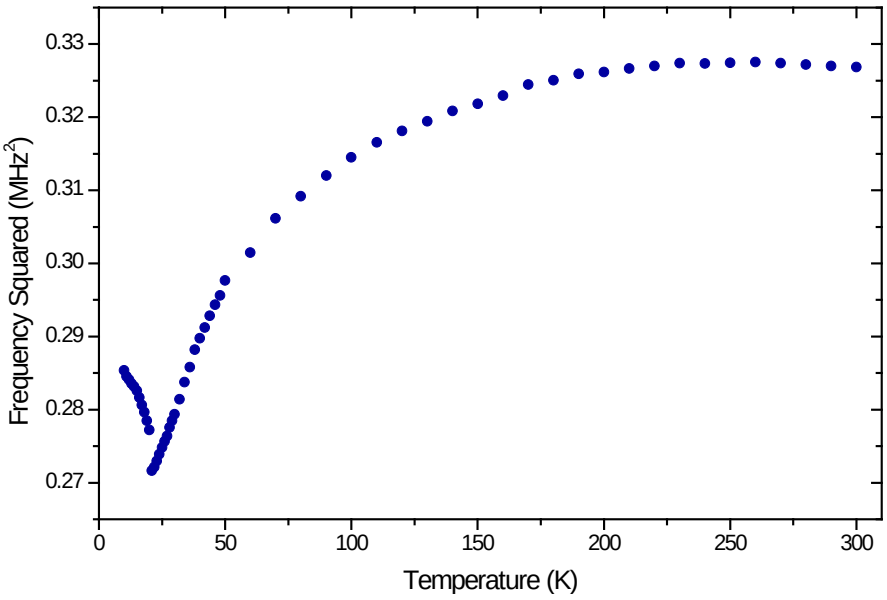

Figure 3.6. Temperature dependence of a representative resonant frequency squared for the optimally-doped material.

The elastic behavior of the material reveals a significant softening upon cooling as the material approaches the superconducting transition at 22K. The amount of softening observed for such a transition is surprising. The softening begins more than 150K above the transition temperature and ceases abruptly at the superconducting transition. The transition is followed by significant stiffening upon further cooling. Figure 3.7 provides two examples from Reference [51] of the elastic behavior observed with RUS for superconducting materials, namely conventional BCS superconductor YNi_2B_2C and popular curate $YBa_2Cu_3O_{7-x}$, near their superconducting transitions. Because these data are given in terms of resonant frequency as a function of temperature and normalized resonant frequency as a function of temperature, respectively, Figure 3.8 provides the RUS data for $BaFe_{1.84}Co_{0.16}As_2$ in these terms for comparison.

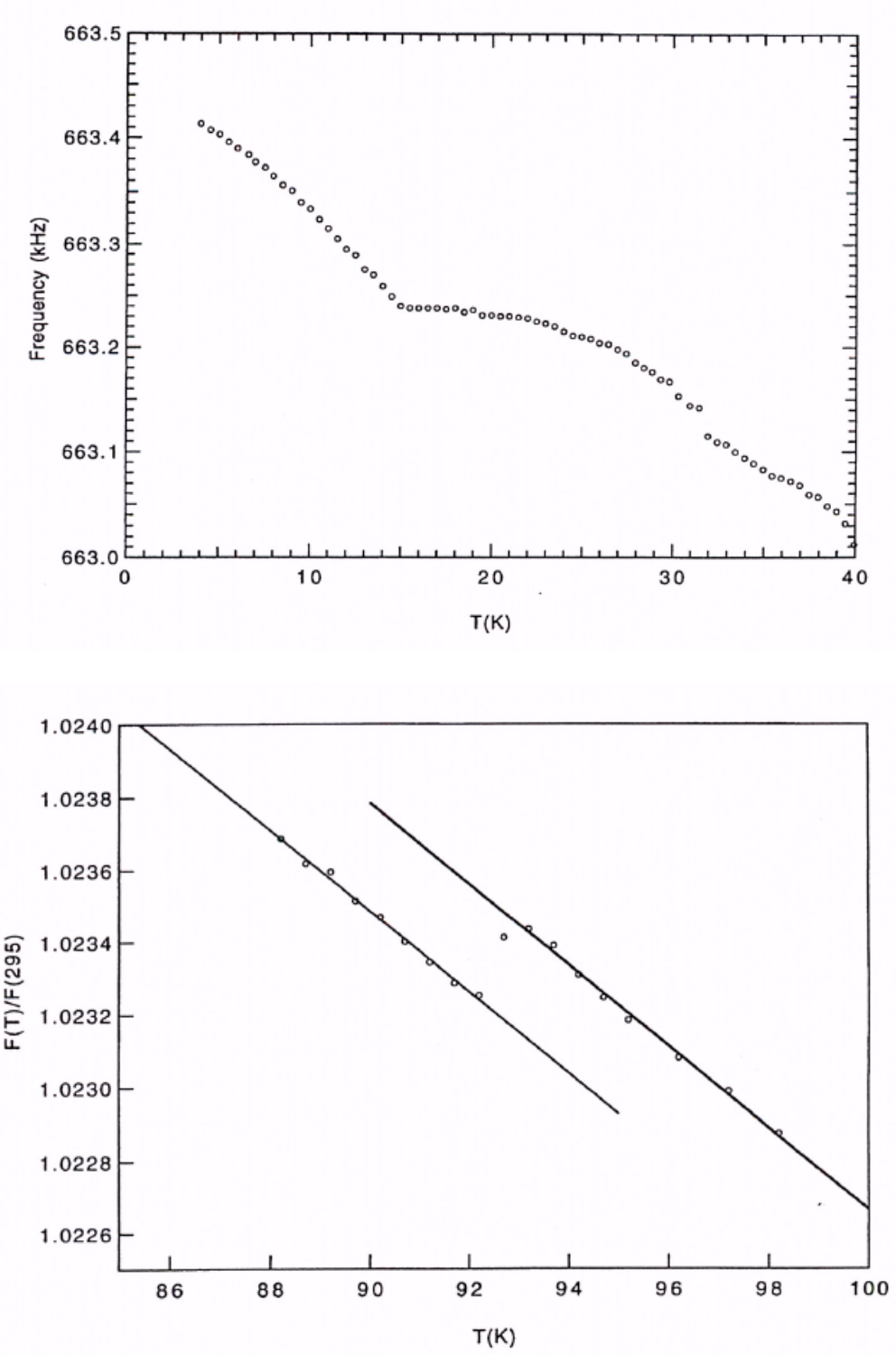

Figure 3.7. Top panel: temperature dependence of a resonant frequency for a single crystal flake of YNi_2B_2C near its T_c of 14K. Bottom panel: temperature dependence of a normalized resonant frequency for a single crystal of $YBa_2Cu_3O_{7-x}$ near its T_c of 93K.[51]

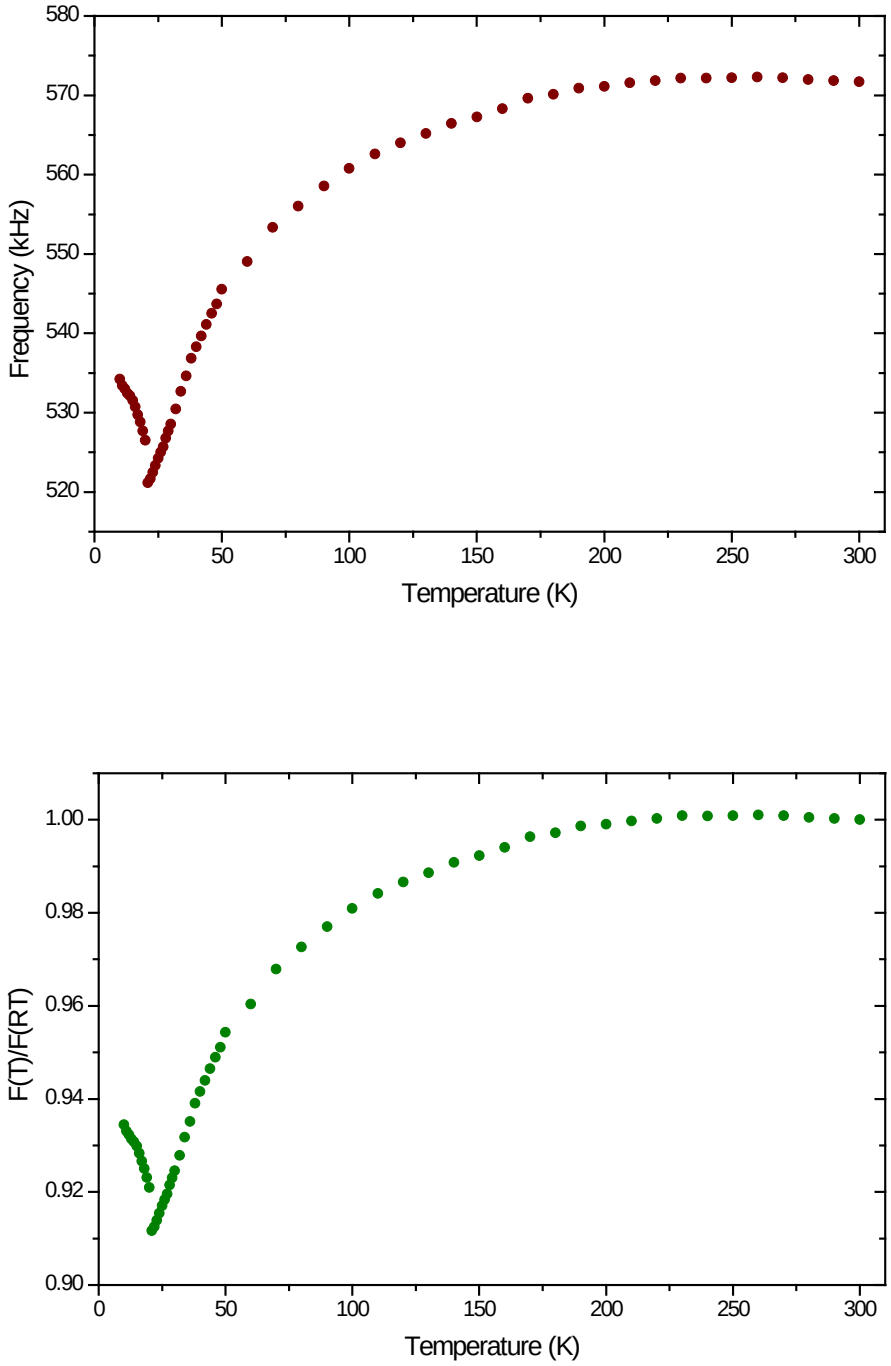

Figure 3.8. Top panel: Temperature dependence of a representative resonant frequency for the $BaFe_{1.84}Co_{0.16}As_2$. Bottom panel: Normalized temperature dependence of a representative resonant frequency for the $BaFe_{1.84}Co_{0.16}As_2$.

The change in slope of the resonant frequency for the YNi_2B_2C at its superconducting transition of 14K is clear in the top panel of Figure 3.7, and the step-like behavior of the resonant frequency is distinct at the superconducting transition of 93K for $YBa_2Cu_3O_{7-x}$ in the bottom panel of the figure. However, it is evident from the comparison of Figures 3.7 and 3.8 that the elastic response of the $BaFe_{1.84}Co_{0.16}As_2$ material to its superconducting transition is much stronger. This fact is more impressive when considering that the data presented in Figure 3.7 represents some of the most pronounced discontinuities in elastic properties due to the superconducting phase transition [51].

As with the parent $BaFe_2As_2$, this behavior is explained by the presence of magnetically-driven nematic fluctuations, revealing that these fluctuations are manifest over a significant portion of the phase diagram. Once more, the shear modulus is represented by a resonant frequency squared that is representative of a larger set of shear-mode-dominated resonant frequencies. Figure 3.9 displays the RUS data along with the renormalization, according to Equation 3.1, of the high-temperature shear modulus $C_{s,0}$ due to the nematic fluctuations. In this case, the nematic fluctuations again act to soften the lattice, and this softening continues until the superconducting transition temperature is reached. Although no structural instability exists at the superconducting transition, a minimum in the shear modulus is observed. This observation is explained by the competition between the antiferromagnetic and superconducting orders. The magnetism is greatly affected by the superconductivity, and the competition between these two orders results in the minimum. The magnetic order is diminished due to the superconductivity, and the shear modulus increases in this superconducting region.

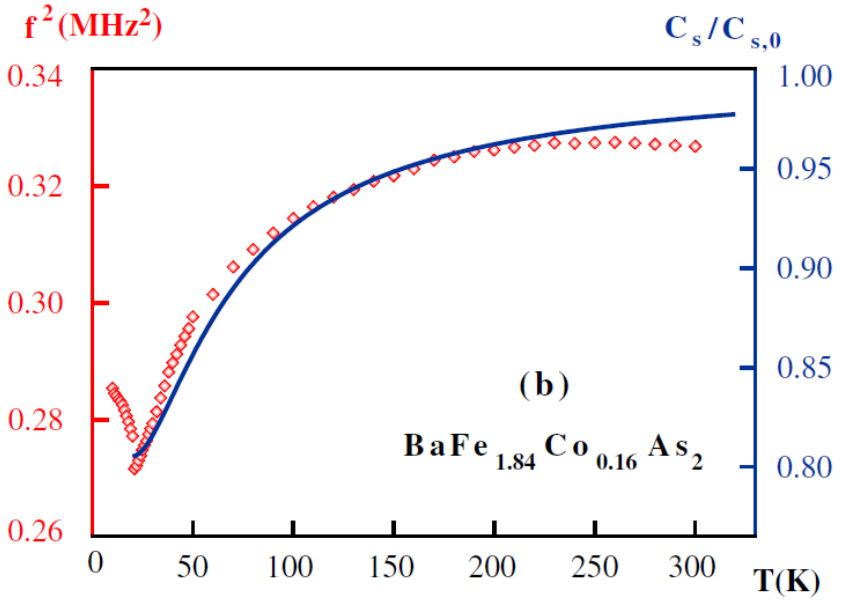

Figure 3.9. Temperature dependence of the resonant frequency squared (red data points) and the calculated shear modulus (solid blue line) of the superconducting material.[61]

Single crystals of overdoped $BaFe_{2-x}Co_xAs_2$ were also examined with RUS. The nominal value of x for these materials is 0.56. This amount of cobalt produces a material that lies beyond the superconducting dome, and, in fact, this material does not display any low-temperature phase transitions. As such, the elastic behavior of this material reveals the expected gradual stiffening upon cooling. A representative resonant frequency squared for this material is seen in Figure 3.10. The material shows gradual stiffening upon cooling with no remarkable features.

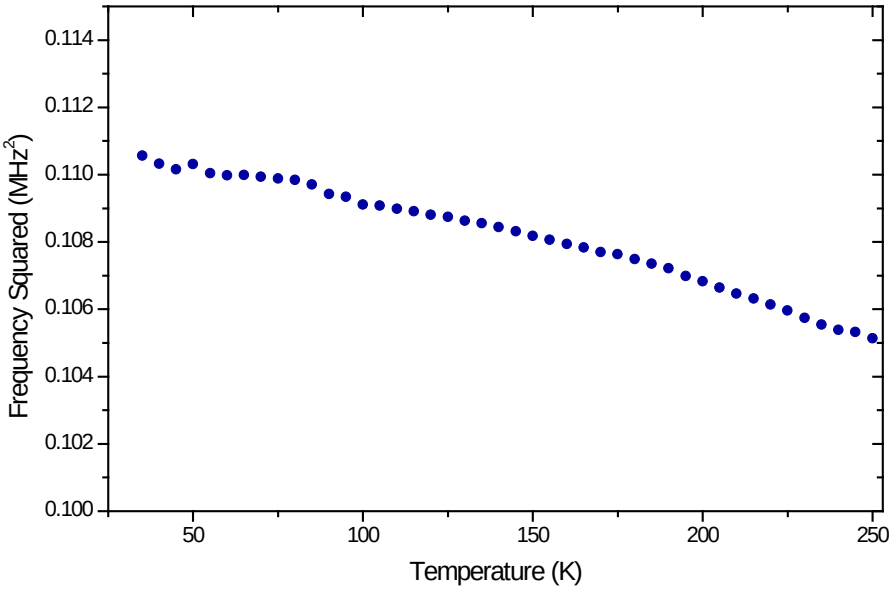

Figure 3.10. Temperature dependence of a representative resonant frequency squared for the overdoped material.

The effect of cobalt doping on the elastic response of these materials is very evident in the RUS data. In order to compare the magnitude of this effect, the three representative doping concentrations are plotted in Figure 3.11 along with the parent material for reference. As mentioned above, the point at which the softening concludes for the parent material is the structural/magnetic transition temperature. A softening is also observed for the underdoped material, but it is far less dramatic. The addition of cobalt acts to suppress these transitions, and while the transitions still occur in the underdoped material, the evidence of this suppression is seen in the diminished amount of softening. For the optimally-doped material, a definite softening is also observed; however, this softening, though dramatic for a superconducting transition, is far less than that seen for a structural transition. Finally, the overdoped material, which presents "normal" temperature dependence, displays little change as the temperature is decreased.

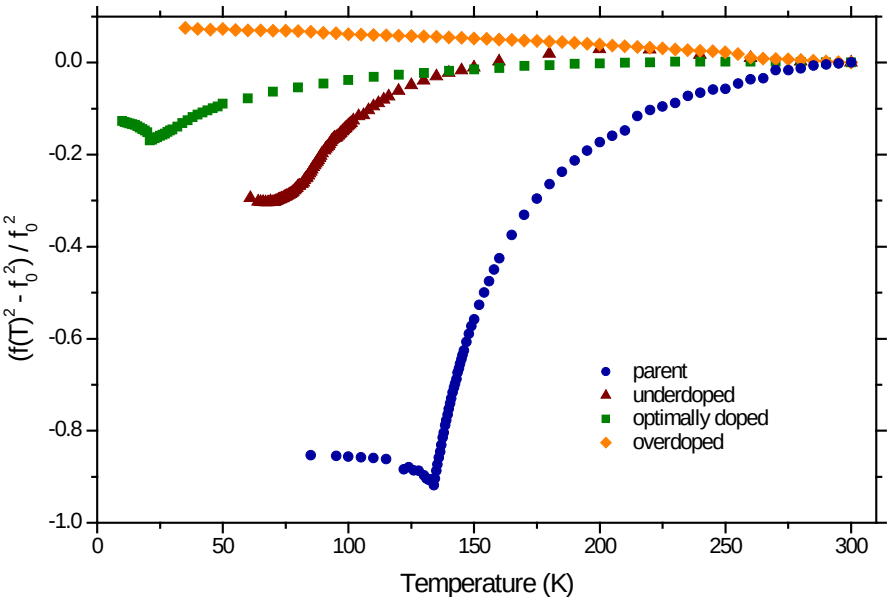

Figure 3.11. Normalized temperature dependence of the squared resonance frequency for $BaFe_{2-x}Co_xAs_2$.

3.1.2 $BaFe_{2-x}Cr_xAs_2$

Single crystals of chromium-doped $BaFe_2As_2$ were also grown in order to determine the effect of chromium doping on the $BaFe_2As_2$ parent material. The addition of chromium acts to hole dope the iron-arsenide layer. It is known that hole doping on the barium site (i.e. potassium doping) and electron doping on the iron-arsenide layer (i.e. cobalt doping) produce superconductivity. In fact, many dopants produce superconductivity in this material. As mentioned, it has also been observed that this superconductivity occurs following a sufficient suppression of both the antiferromagnetic transition and the tetragonal-to-orthorhombic structural transition.

For the $BaFe_{2-x}Cr_xAs_2$ crystals grown, it was found that the percent of chromium in the resulting single crystals was less than that put into the growth mixture. As mentioned in the experimental details, the crystals were analyzed with EDS in order to determine the amount of chromium present. Table 3.1 lists the nominal and measured values of x for many of the $BaFe_{2-}$

$_xCr_xAs_2$ compounds grown (an error of ±0.02 is associated with these values). Because the measured values represent the actual chromium content, this value is used to identify the crystals.

Table 3.1. Nominal and measured values of x for the $BaFe_{2-x}Cr_xAs_2$ crystals.

Nominal x	Measured x
0	0
0.06	0.04
0.12	0.08
0.22	0.14
0.28	0.2
0.32	0.23
0.34	0.25
0.5	0.36
0.54	0.40
0.81	0.61
0.9	0.67
1	0.75
2	2

Naturally, the electrical resistivity of these materials is of great interest. These measurements were performed for a representative group of the $BaFe_{2-x}Cr_xAs_2$ crystals. The temperature-dependent electrical resistivity for materials with x values of 0, 0.04, 0.08, 0.14, 0.36, and 0.75 is given in Figure 3.12. As is apparent, none of these materials achieve zero electrical resistivity. In fact, the parent material is the only material to show a significant reduction in resistivity. After a gradual reduction, a sharp drop in the resistivity of the parent material is seen near the transition temperature of 132K. Instead, for the $BaFe_{2-x}Cr_xAs_2$ materials

with $0.04 \leq x \leq 0.36$, there is a very gradual reduction of the resistivity upon cooling down to some temperature at which this resistivity shows a sharp increase. It is also evident that the temperature of this upturn decreases with increasing chromium content. For the material with an x value of 0.75, the resistivity changes little with temperature until low temperatures where it begins to increase.

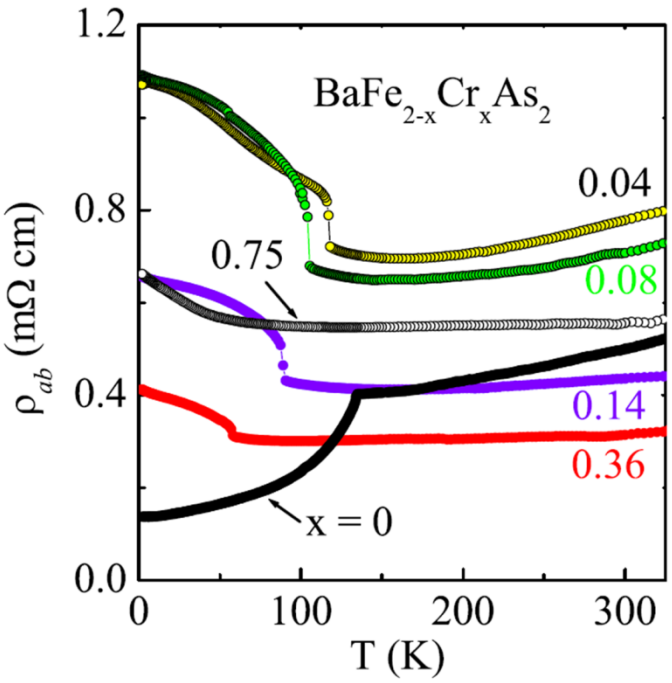

Figure 3.12. Electrical resistivity as a function of temperature for $BaFe_{2-x}Cr_xAs_2$ materials.[67]

These materials were also examined with various other techniques. Figure 3.13 displays the temperature-dependent data of the magnetic susceptibility, Hall coefficient, and specific heat. The systematic changes that occur as the amount of chromium increases are evident. Each of these measurements reveals features that identify the magnetic transition temperature for these materials. In Figure 3.13, panels a and b display the susceptibilities along the a-b and c directions, respectively. Below the magnetic transition, these susceptibilities become anisotropic

in these two sets of directions. From this data, the magnetic transition temperature is 118K for chromium content x = 0.04, 104K for x = 0.08, 88K for x = 0.14, 80K for x = 0.20, and 58K for x = 0.36. For these compositions, the magnetic transition temperatures agree well with the abrupt upturn seen in resistivity data, the sharp anomaly observed in the Hall coefficient, and the peak detected in the specific heat measurements. These measurements are used to create a partial phase diagram for $BaFe_{2-x}Cr_xAs_2$ as a function of chromium doping, discussed below (Figure 3.16). The anomalies seen for these intermediate chromium concentrations are different for the $BaFe_{1.25}Cr_{0.75}As_2$ material. In this case, the magnetic anisotropy switches for the magnetic susceptibility, the Hall coefficient is relatively independent of temperature, and there is no peak observed in the specific heat data. These data suggest that this high concentration of chromium has significantly changed the characteristics of the material.

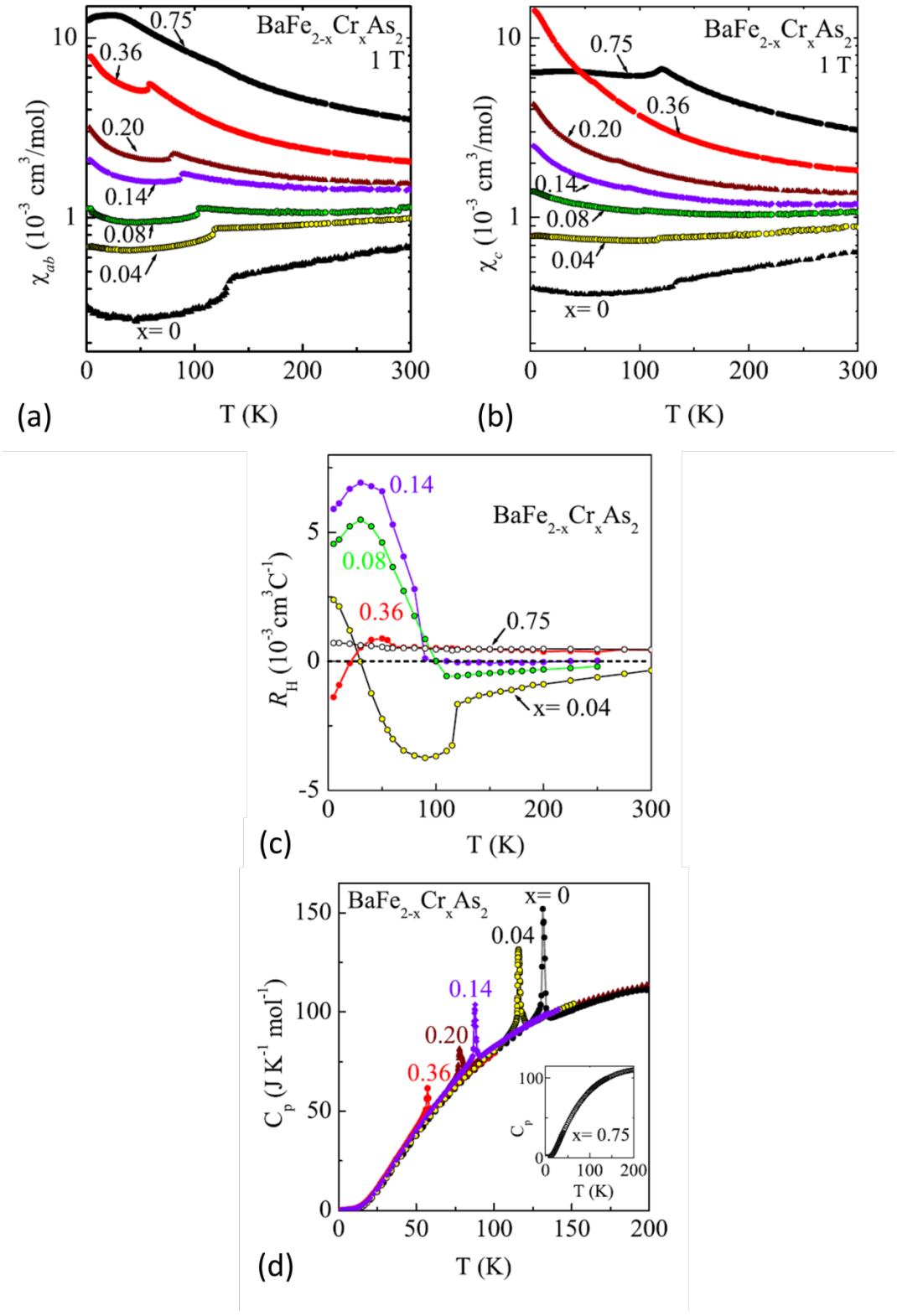

Figure 3.13. Magnetic susceptibility along the(a) a-b and(b) c directions, (c) Hall coefficient, and (d) specific heat for a series of $BaFe_{2-x}Cr_xAs_2$ materials.[67]

In order to establish the quality of the crystals and determine the lattice constants for these materials, single crystals from each growth were ground for powder X-ray diffraction. As the resulting crystals are rather small in the c direction, several of the crystals were often needed to perform these measurements. Crystals were chosen carefully to avoid excess flux material and to preserve some of the crystals for further measurements. Figure 3.14 provides room temperature X-ray diffraction patterns for a number of the crystals grown, and Figure 3.15a displays the lattice constants as a function of chromium concentration. While the *a* parameter changes little with concentration, the *c* parameter increases as the chromium concentration increases. In addition, Figure 3.15b presents the change in these lattice parameters with temperature for the materials with an x value of 0.04. This material is lightly doped, and a structural and magnetic transition similar to those of the parent material is expected for this composition.

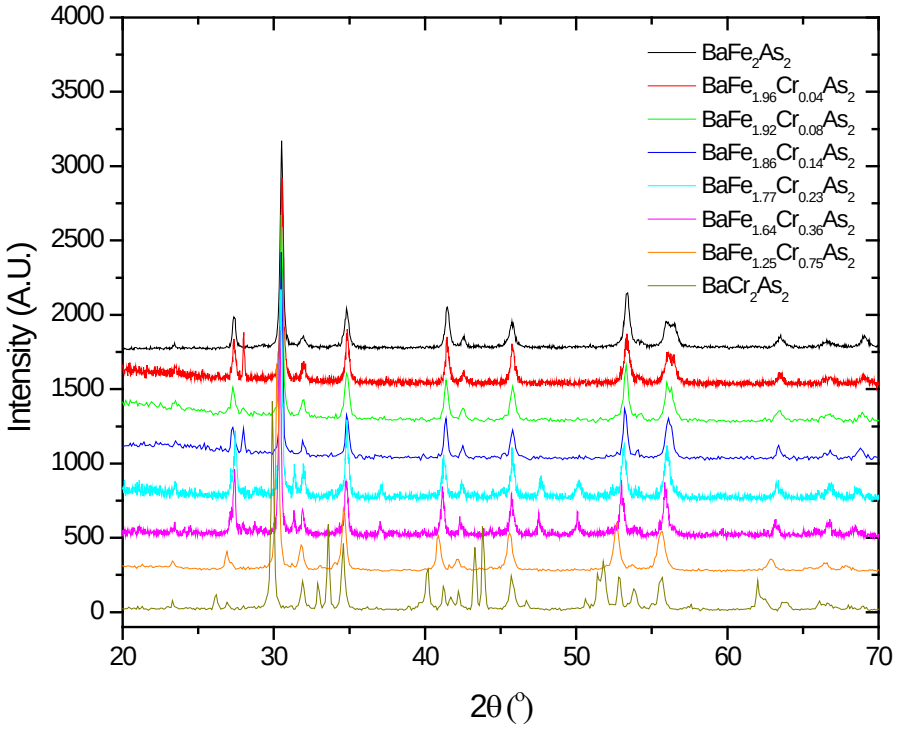

Figure 3.14. Powder X-ray diffraction patterns for several of the materials in the $BaFe_{2-x}Cr_xAs_x$ series.

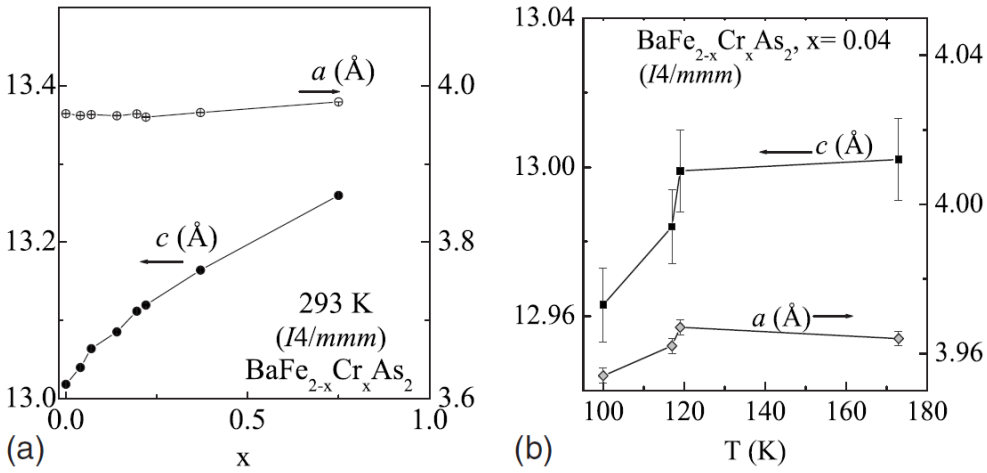

Figure 3.15. (a) Lattice parameters as a function of concentration and (b) temperature dependence of lattice parameters for an x value of 0.04.[67]

A distinct decrease in both lattice parameters is observed for the x=0.04 material at about 119K upon cooling. While there appears to be some structural change around 119K, these initial X-ray refinements indicate that the structure remains tetragonal. Because a distortion to different crystal symmetry was not detectable with this data, though it was expected, a partial phase diagram including only the magnetic transition temperatures for these materials was developed. This phase diagram is provided in Figure 3.16. From this diagram, it does appear that the addition of chromium acts to suppress the magnetic transition, as observed for the cobalt doping as well. Because superconductivity does not occur with these materials, it is apparent that the suppression of this spin density wave antiferromagnetic order is not solely responsible for the development of superconductivity in these materials.

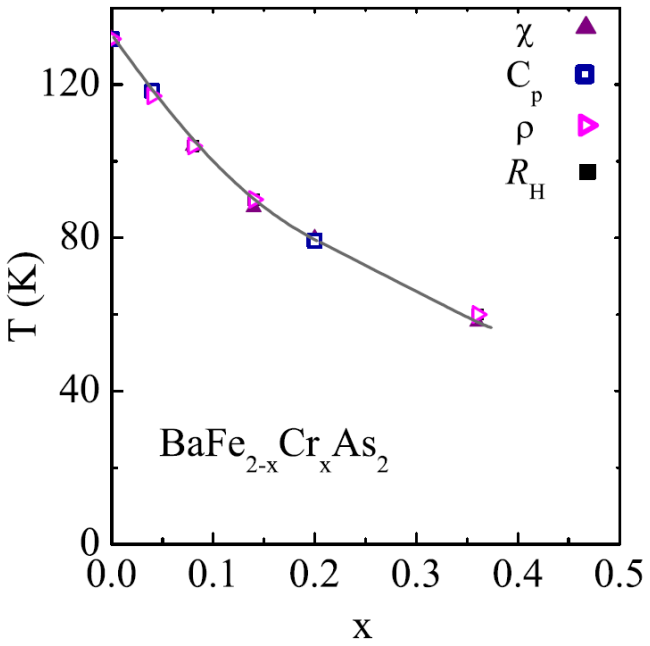

Figure 3.16. Partial magnetic phase diagram for $BaFe_{2-x}Cr_xAs_2$.[67]

RUS measurements were performed on many of these chromium-doped materials, and the data for $BaFe_{1.96}Cr_{0.04}As_2$, which has the lowest chromium concentration of these materials, are shown in Figure 3.17. As with the other layered iron-arsenide materials reported, a full determination of the elastic tensor was not possible. However, Figure 3.17 provides a representative resonant frequency squared for this material. As before, the temperature dependence of this resonant frequency represents the temperature dependence of the material's elastic behavior. A very dramatic softening is observed as this material approaches the magnetic transition temperature (near 118K) and the abrupt lattice parameter change (near 119K). Such a large softening observed in RUS data indicates a structural transition. This softening, which is arrested below T = 118K, is also very similar to that observed at the tetragonal-to-orthorhombic structural transition for the underdoped $BaFe_{2-x}Co_2As_2$ material seen earlier.

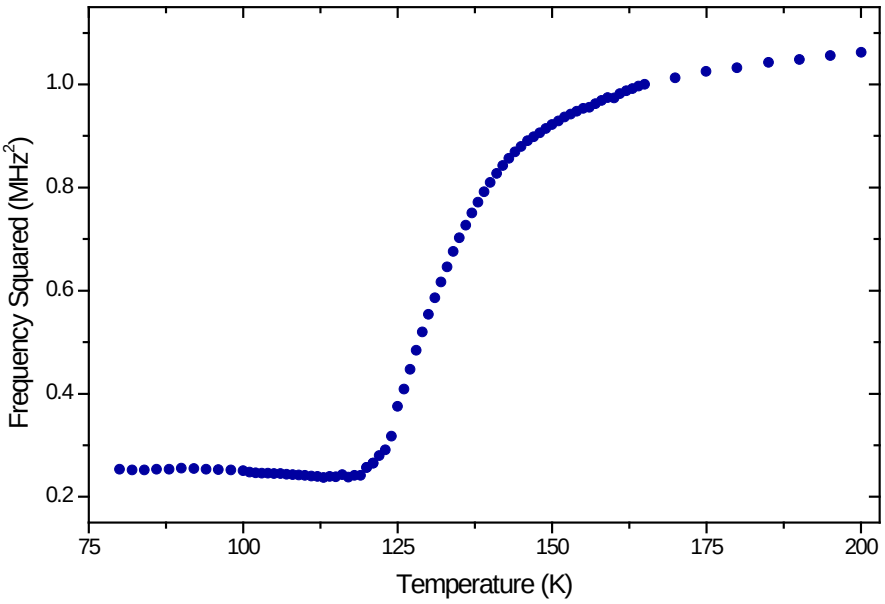

Figure 3.17. Temperature dependence of a representative resonant frequency squared for $BaFe_{1.96}Cr_{0.04}As_2$.

As mentioned, many of these $BaFe_{2-x}Cr_xAs_2$ materials were examined with RUS. Figure 3.18 provides results for three other chromium concentrations: x = 0.08, x = 0.25, and x = 0.75. For the lower doping concentrations, a sharp softening with an abrupt stop is observed, similar to the $BaFe_{1.96}Cr_{0.04}As_2$ material. For $BaFe_{1.92}Cr_{0.08}As_2$, this softening occurs as the temperature approaches approximately 104K, and for $BaFe_{1.75}Cr_{0.25}As_2$, this temperature is approximately 75K. These temperatures correspond to the magnetic transitions outlined earlier; however, as mentioned, such large softening is often indicative of a structural instability. The transition temperature is suppressed as more chromium is added to the system. A softening is also apparent in the $BaFe_{1.25}Cr_{0.75}As_2$ material, which becomes stronger as the temperature nears 19K. However, this material does not show the same features as the materials with lower chromium concentration.

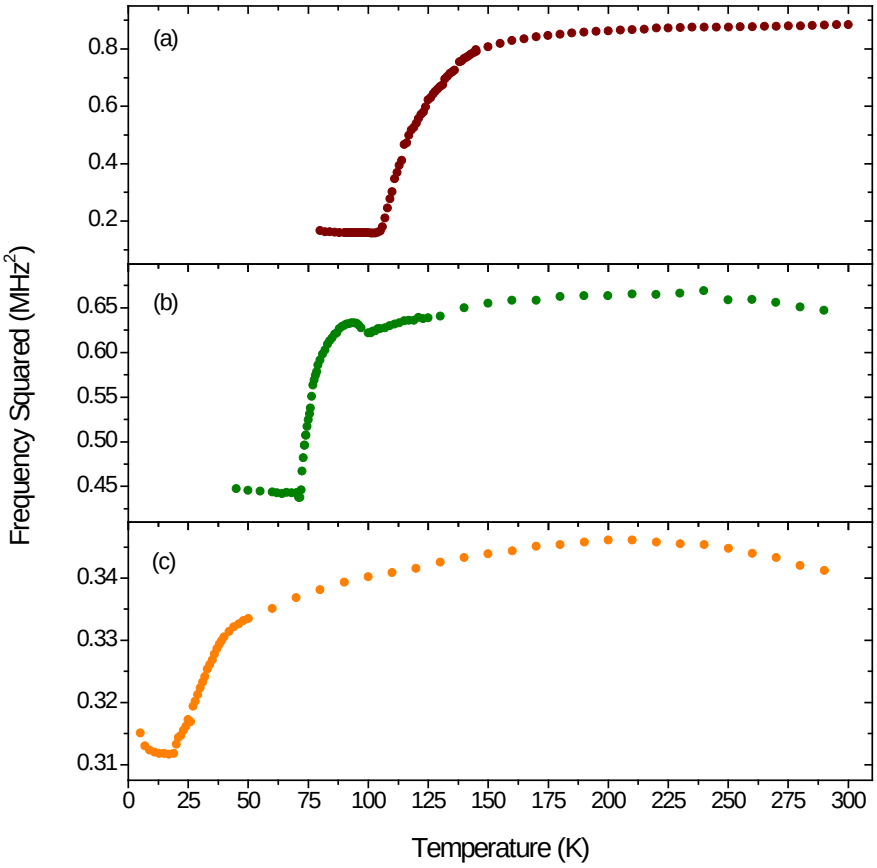

Figure 3.18. Temperature dependence of a representative resonant frequency squared for (a) $BaFe_{1.92}Cr_{0.08}As_2$, (b) $BaFe_{1.75}Cr_{0.25}As_2$, and (c) $BaFe_{1.25}Cr_{0.75}As_2$.

Although each of the samples displays an apparent softening, the magnitude of this softening is very different. Figure 3.19 provides an illustration of how the assumed structural instability is suppressed with the addition of chromium. The RUS data for this series of materials are normalized at room temperature for comparison. While the suppression of the transition temperature was observed before, here the reduction in the amount of softening observed with increasing chromium content is made apparent. The degree of softening is systematically reduced with the addition of chromium, much like that seen for the addition of cobalt.

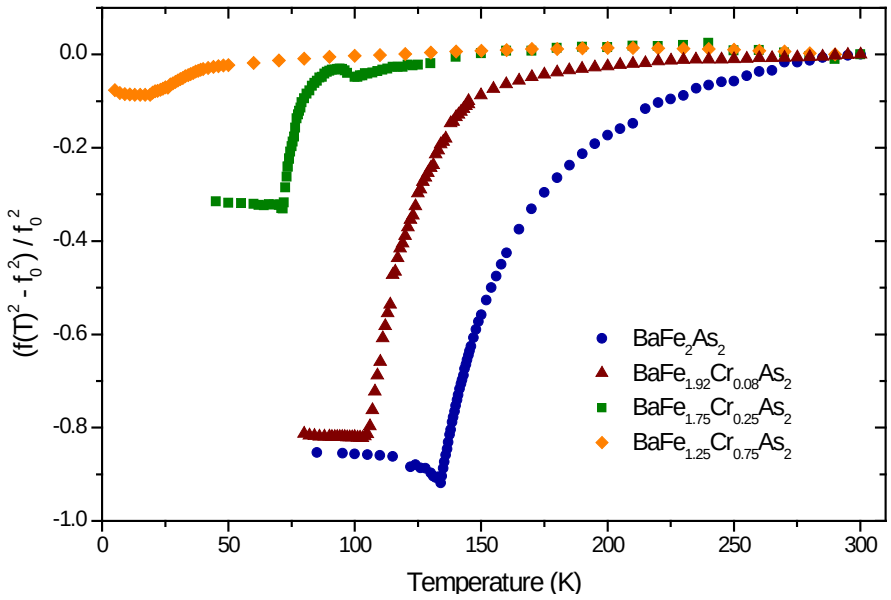

Figure 3.19. Normalized temperature dependence of the squared resonant frequency for $BaFe_{2-x}Cr_xAs_2$.

These data show that, similar to cobalt doping, the addition of chromium does suppress the structural and magnetic transitions. However, it is apparent from both the RUS data and the phase diagram that chromium doping is much less effective at suppressing these transitions. For the samples represented here, the material that is underdoped with cobalt ($BaFe_{1.9}Co_{0.1}As_2$) and the $BaFe_{1.92}Cr_{0.08}As_2$ material have very similar amounts of dopant. Yet, their elastic responses are different; these responses are compared in Figure 3.20a along with the parent material for reference. The cobalt-doped sample shows a much more dramatic shift in transition temperature as well as a much more pronounced decrease in softening. Furthermore, the optimally-doped cobalt material has a much lower doping concentration than the $BaFe_{1.75}Cr_{0.25}As_2$ material; these materials are compared in Figure 3.20b. In fact, the chromium-doped samples clearly display the structural/magnetic phase transitions with doping concentrations well beyond the limit of the superconducting dome for the cobalt-doped samples.

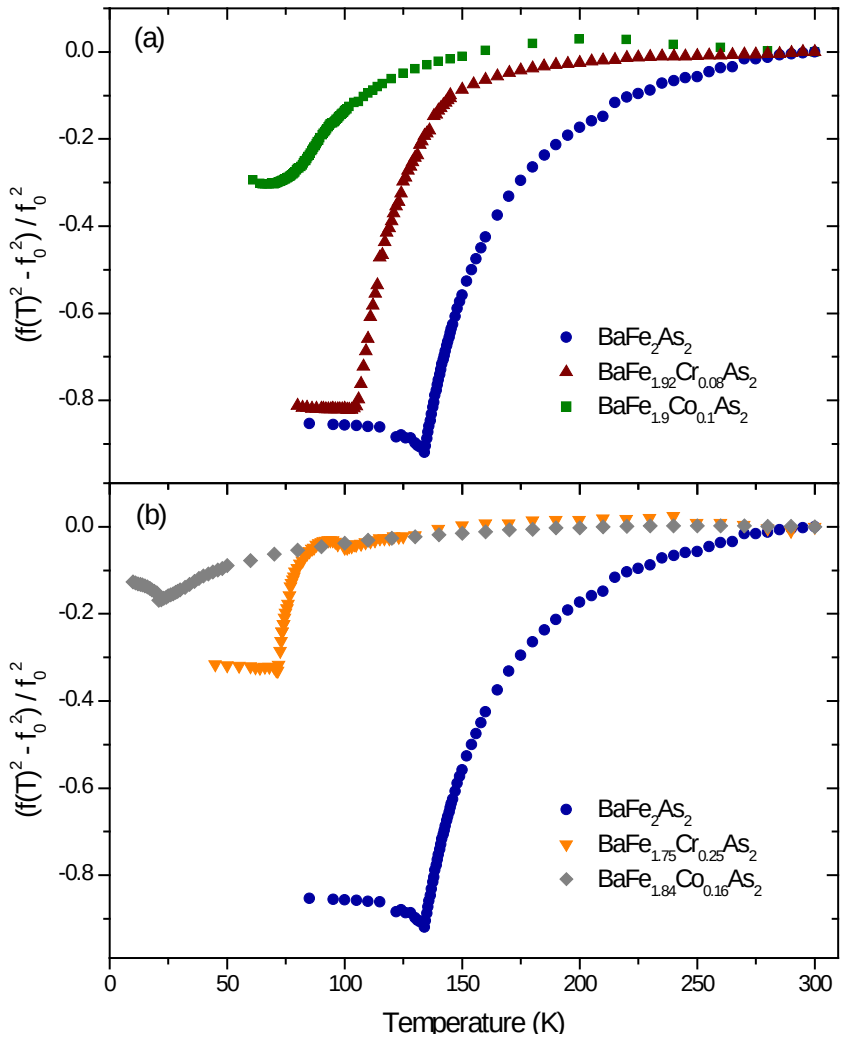

Figure 3.20. Comparison of the elastic response of (a) $BaFe_{1.92}Cr_{0.08}As_2$ and $BaFe_{1.9}Co_{0.1}As_2$ with the parent $BaFe_2As_2$ and (b) $BaFe_{1.75}Cr_{0.25}As_2$ and $BaFe_{1.84}Co_{0.16}As_2$ with the parent $BaFe_2As_2$.

The addition of chromium does eventually suppress the magnetic and structural phase transition; however, it requires considerably more chromium to achieve this suppression than cobalt. While these transitions seen in the parent material are more robust with the addition of chromium, this larger amount of required doping for suppression does not explain the lack of superconductivity. It has been observed that ruthenium doping, which does produce superconductivity, requires a similar concentration to suppress the magnetic transition (when

compared to chromium doping) [21, 22]. The lack of superconductivity in chromium-doped $BaFe_2As_2$ is attributed to the favorability of magnetism across the $BaFe_{2-x}Cr_xAs_2$ phase diagram. A stronger covalency exists for chromium and arsenic than for iron and arsenic, which leads chromium-doped materials to have an antiferromagnetic preference. In fact, from neutron diffraction data [68], a competition between two antiferromagnetic states develops with the addition of chromium. A more complete phase diagram for this system is provided in Figure 3.21; this diagram was developed via neutron diffraction [68].

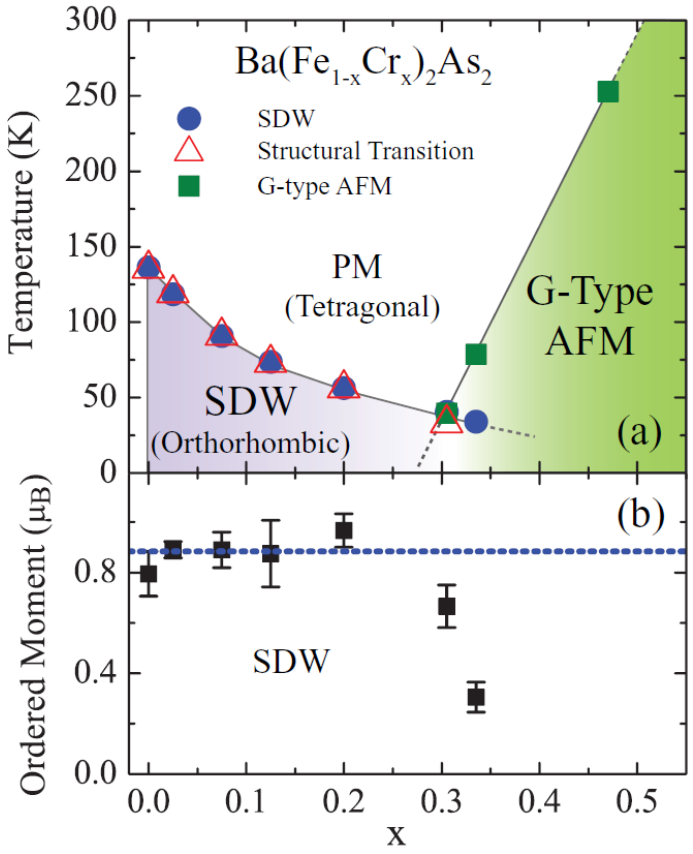

Figure 3.21. Partial phase diagram of $Ba(Fe_{1-x}Cr_x)As_2$ illustrating both magnetic and structural phase transitions as a function of chromium concentration.[68]

This phase diagram illustrates the suppression of both the spin-density-wave antiferromagnetic order and the tetragonal-to-orthorhombic transitions with the addition of chromium, but it also includes the development of a G-type antiferromagnetic order at higher chromium concentrations. A continuous transition from spin density wave order to G-type antiferromagnetic order is observed. Moreover, for some compositions, these two states appear to coexist, though it is not clear if this is due to phase separation. Nevertheless, strong magnetism is observed at all chromium concentrations. These competing states provide a natural explanation for the absence of superconductivity in the $BaFe_{2-x}Cr_xAs_2$ materials. Long-range magnetic order throughout the phase diagram is sufficient to prevent the development of superconductivity.

3.2 $TlFe_{1.6}Se_2$

The elastic behavior as a function of temperature is also studied for $TlFe_{1.6}Se_2$. As discussed in Chapter 1, anomalies have recently been observed in $TlFe_{1.6}Se_2$ near 100K and 140K [32, 33, 35]. These anomalies have been attributed to the canting of the iron spins at 140K and the recovery of the original magnetic structure at 100K [33]. While this material is not superconducting, it is very close to superconductivity; materials with slightly higher iron content (i.e. $TlFe_{1.7}Se_2$) are superconductors.

As with the $BaFe_2As_2$-based samples, the elastic behavior of the $TlFe_{1.6}Se_2$ material is represented by the square of the resonant frequencies obtained from RUS measurements. Figure 3.22 displays this low-temperature behavior. At higher temperature, the material shows very gradual stiffening. However, near the initial transition temperature of 140K, the material undergoes a gradual softening. Although the magnitude of this softening appears substantial in the RUS data, the amount of softening is actually less than 2%. As the temperature is further

decreased and approaches the recovery of the magnetic structure near 100K, the material stiffens. An effect on the elastic behavior is expected at this temperature due to the abrupt change that occurs in the *c* lattice parameter.

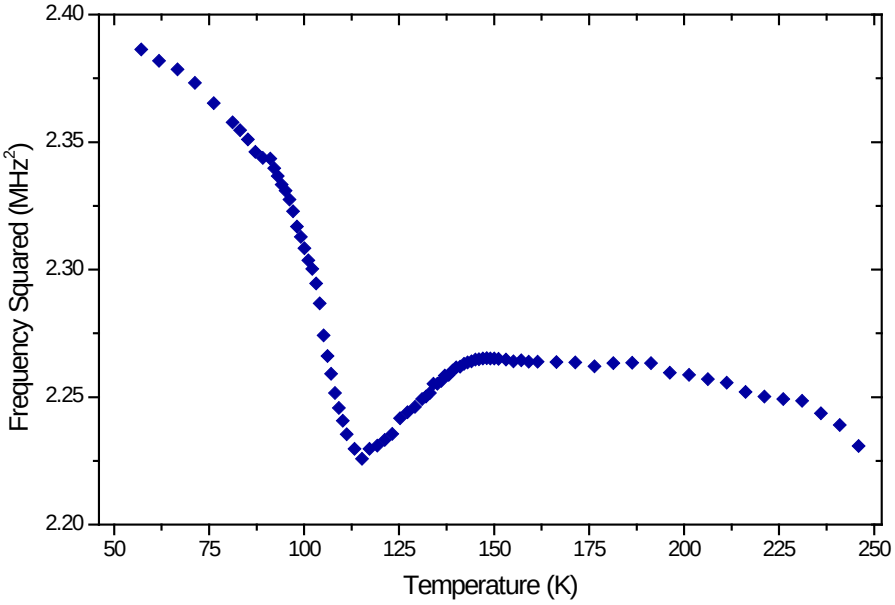

Figure 3.22. Temperature dependence of a representative resonant frequency squared for $TlFe_{1.6}Se_2$.

Because these two transitions are magnetic in nature (the iron moments cant away from the c-axis between 140K and 100K), the effect of an applied magnetic field on the elastic behavior is of interest. Therefore, RUS data were also collected while applying a magnetic field. Figure 3.23 displays the temperature dependence of two representative squared resonant frequencies at 0T, 0.5T, and 3T for comparison. These data were collected with the magnetic field applied parallel to the c-axis of the material. Though these transitions have been described in terms of a magnetic change, the elastic behavior displays little change with applied magnetic field. If these transitions were magnetically driven, one would expect the application of a strong magnetic field in the c direction to suppress this change in some way. However, the magnetic

field does not appear to affect the behavior of the material. These data provide evidence that the canting of the magnetic moments is not solely responsible for the transitions at low temperature.

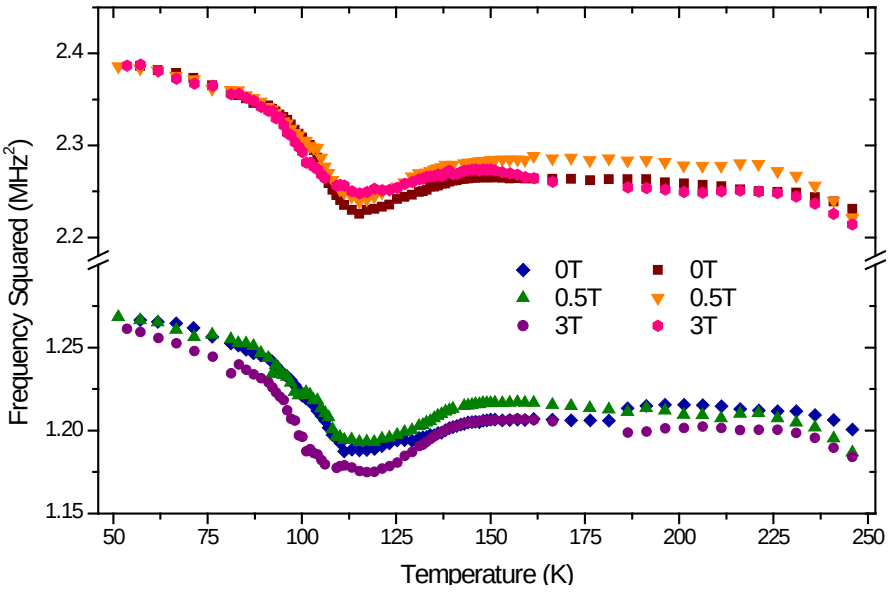

Figure 3.23 Temperature dependence of two representative resonant frequencies squared for $TlFe_{1.6}Se_2$ with applied magnetic field.

In addition, the high temperature RUS setup was used to examine the elastic behavior of $TlFe_{1.6}Se_2$ above room temperature. These data are displayed in Figure 3.24, and from this figure it is apparent that the elastic behavior changes little as the temperature is increased. No observable change is detected at the antiferromagnetic transition at 430K. There is a slight softening that appears just below 460K, which is likely due to the vacancy ordering that occurs near this temperature. Each of the resonant frequencies seen in the figure shows a different amount of change at this temperature. These differences are not unexpected because these resonant frequencies may have very different dependencies on the elastic constants (see section 2.1.6).

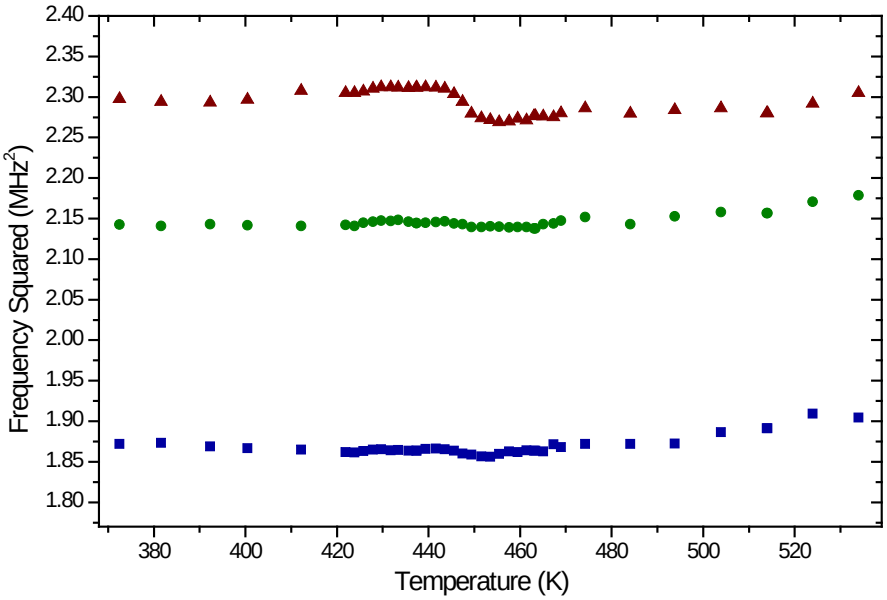

Figure 3.24 Temperature dependence of representative resonant frequencies squared for $TlFe_{1.6}Se_2$ above room temperature.

Chapter 4

Results – Thermoelectric Materials

4.1 Mo_3Sb_7

A series of Mo_3Sb_7-based promising thermoelectric materials was examined with RUS. Several three-dimensional single crystals were measured including the parent Mo_3Sb_7 as well as samples of this material doped with ruthenium, tellurium, and chromium. These crystals were oriented and shaped into rectangular parallelepipeds aligned so that each face was polished along a (100) plane. RUS measurements were then performed in order to determine the values of the elastic tensor and the elastic behavior of these materials as a function of temperature.

Because these materials have cubic crystalline symmetry, the elastic tensor consists of only three independent elastic constants: c_{11}, c_{12}, and c_{44}. Also, c_{11} and c_{12} allow determination of an alternative constant c':

$$c' = \frac{c_{11} - c_{12}}{2} \tag{4.1}$$

Though c' is determined as a function of c_{11} and c_{12}, it is an important value to consider due to its physical significance. The c' constant represents the second propagating transverse wave in a material with cubic symmetry, as it is proportional to this wave's velocity squared. (In a similar fashion, the first propagating transverse wave is represented by c_{44}, and the longitudinal wave is represented by c_{11}.) While this constant is a function of c_{11} and c_{12}, as seen in the equation, it is actually better defined in the following RUS data because some of the measured resonant frequencies are almost entirely dependent on this c' value.

For the parent Mo_3Sb_7 material, the room temperature values for these elastic constants found using RUS are as follows: c_{11} = 178 GPa, c_{12} = 87 GPa, c_{44} = 67.8 GPa, and c' = 45 GPa.

To illustrate how these quantities change upon cooling, plots of the elastic constants as a function of temperature are provided for the parent material in Figure 4.1. The temperature dependence of the elastic constants directly determined from the RUS output file is shown in Figure 4.1a, and the temperature dependence of *c'* is shown in Figure 4.1b along with that of c_{44} for reference. From this temperature-dependent RUS data, it is apparent that the c_{11}, c_{12}, and *c'* values display a very dramatic softening as the material approaches the cubic-to-tetragonal structural transition near 53K, while c_{44} shows little change as temperature is changed. The difference between the two transverse values shown in Figure 4.1b is apparent: c_{44} shows only slight stiffening while *c′* displays a dramatic softening preceding the phase transition at 53K.

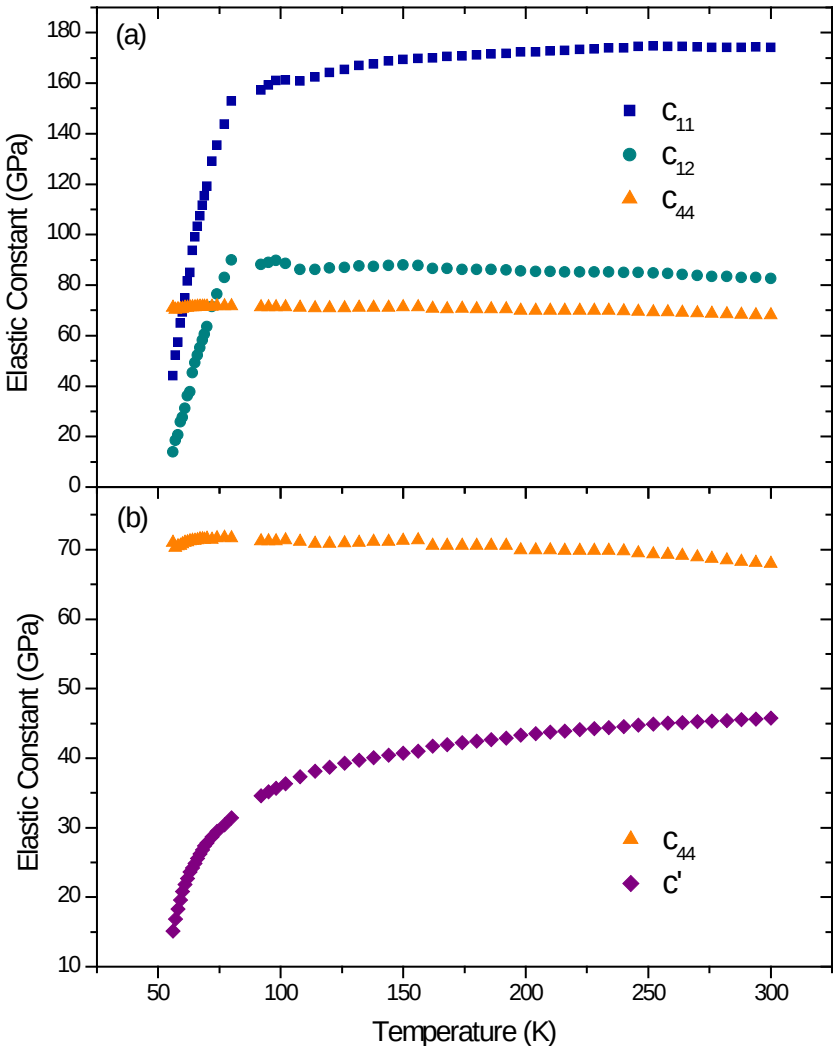

Figure 4.1. Temperature-dependent elastic constants for Mo_3Sb_7. The three independent elastic constants are included in (a), and c' is provided in (b) with c_{44} for reference.

Though RUS data were collected down to a temperature of 2K, the results presented do not proceed below the structural phase transition. These results include much of the cubic phase (with three independent elastic constants), but following the transition to tetragonal structure (with six independent elastic constants), the RUS spectra are no longer clear enough to evaluate peak locations. Figure 4.2 provides an illustration of this difficulty. Figure 4.2a displays a partial resonant spectrum for this material at a temperature above the structural transition. Here,

the peaks identifying the resonant frequency locations are clear and prominent. On the other hand, Figure 4.2b displays this same partial resonance spectrum at a temperature below the structural transition. At this point, no peaks can be detected, and the locations of the resonant frequencies are unknown. Below the transition (at approximately 23K), the RUS signal does improve. Several resonances appear at very low temperatures, but we cannot observe a sufficient amount of resonances to allow the calculation of the low-temperature elastic constants. Furthermore, the response of the resonant frequencies present at low temperatures does not show any "irregularity" at the superconducting transition at 2.35K. Figure 4.3 displays a few of the representative resonant frequencies near this superconducting transition temperature.

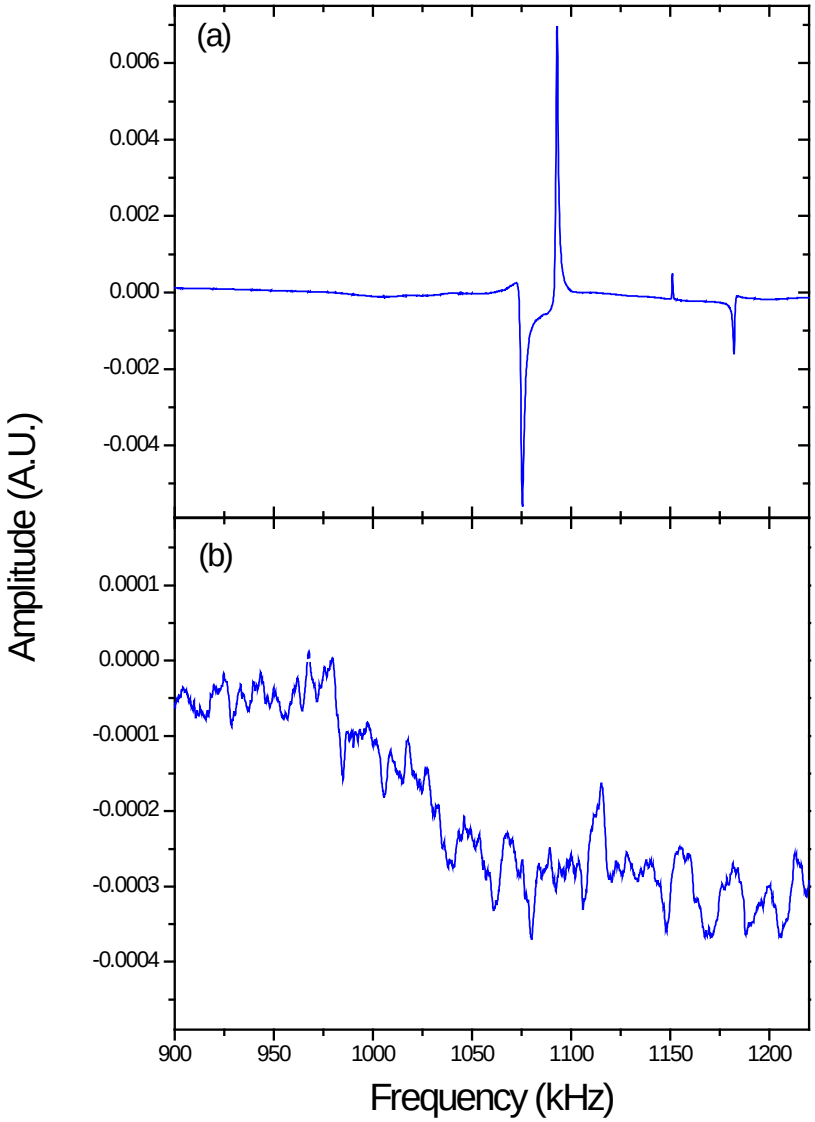

Figure 4.2. A resonance spectrum (a) above the structural transition temperature and (b) below the structural transition temperature.

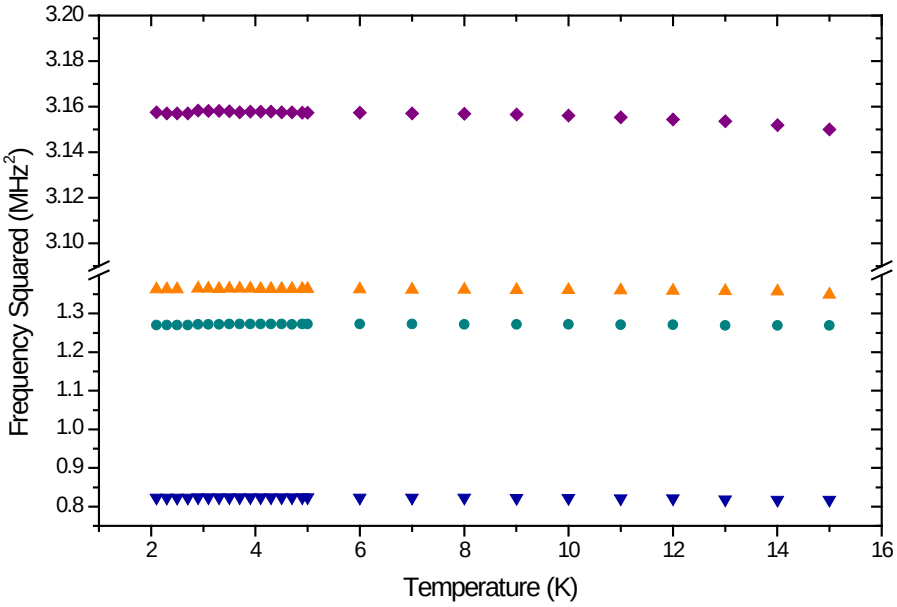

Figure 4.3. Temperature dependence of representative resonant frequencies squared for Mo_3Sb_7 near the superconducting transition.

4.1.1 $Mo_{3-x}Ru_xSb_7$

The effect of ruthenium on the elastic behavior of the Mo_3Sb_7 parent material was also examined with RUS. The primary material examined for this purpose had an x value of 0.09, or a composition of $Mo_{2.91}Ru_{0.09}Sb_7$. For this amount of ruthenium doping, the structural transition from cubic to tetragonal is suppressed, and the superconducting transition is still present, although at a slightly lower temperature.

The room temperature elastic constants for this material determined from RUS are as follows: c_{11} = 189 GPa, c_{12} = 86 GPa, c_{44} = 74.8 GPa, and c' = 51 GPa. The addition of ruthenium dopant to the parent Mo_3Sb_7 increases its elastic constants. Because the c' value is better determined than c_{11} and c_{12}, this value is used to display the elastic response of the material as a function of temperature. This behavior is shown in Figure 4.4; because c_{44} does not change much with temperature, this value is also provided in the figure in order to provide some

scale. Although the structural transition has been suppressed by the addition of ruthenium, a significant amount of softening is still observed in *c'*. Though this material remains cubic, some structural instability still exists as evidenced by this softening.

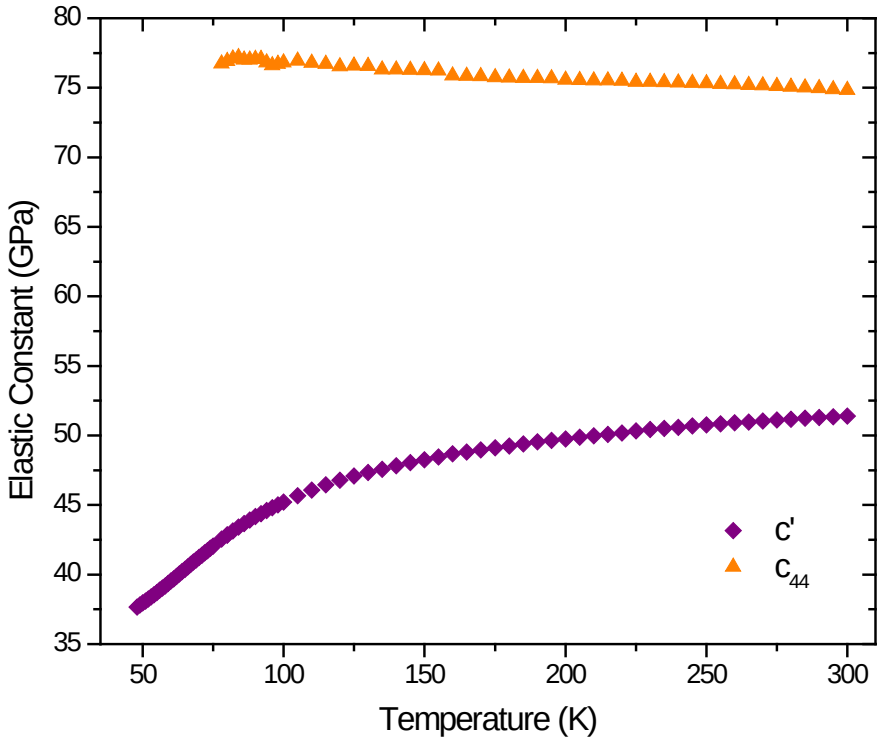

Figure 4.4. Temperature-dependent elastic constants for $Mo_{2.91}Ru_{0.09}Sb_7$.

The effect of much higher ruthenium doping was also investigated with RUS. In this case, a material with a composition of $Mo_{2.1}Ru_{0.9}Sb_7$ was examined. Figure 4.5 provides the squared frequency of a representative resonant peak in order to observe the temperature-dependent elastic behavior. Although the irregularly-shaped sample was only about a millimeter in each dimension and not large enough to shape for a determination of the elastic tensor, the RUS data show that such a large amount of ruthenium destroys the structural instability responsible for the significant softening seen in the $Mo_{2.91}Ru_{0.09}Sb_7$ material. For $Mo_{2.1}Ru_{0.9}Sb_7$,

the temperature dependence of the representative resonant frequency reveals that the material slightly stiffens as the temperature is decreased, and no softening associated with the structural instability remains.

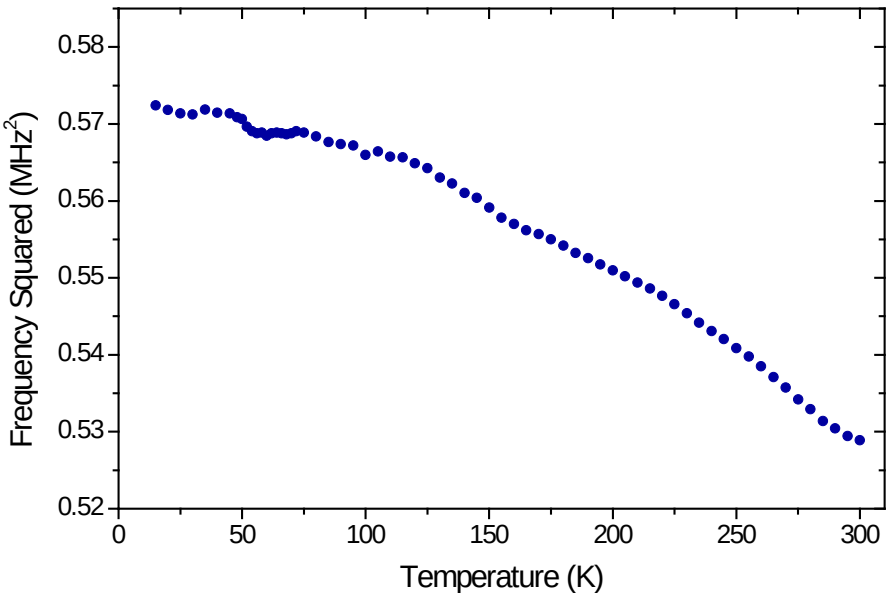

Figure 4.5. Temperature dependence of a representative resonant frequency squared for $Mo_{2.1}Ru_{0.9}Sb_7$.

4.1.2 $Mo_3Sb_{7-x}Te_x$

Tellurium-doped samples of Mo_3Sb_7 were also examined with RUS. Although the tellurium replaces antimony rather than molybdenum, these materials behave very similarly to the ruthenium-doped materials. The structural transition is destroyed with light doping, and the superconducting transition temperature is slightly suppressed. Here, two materials that are lightly doped with tellurium are considered: $Mo_3Sb_{6.925}Te_{0.075}$ and $Mo_3Sb_{6.9}Te_{0.1}$.

From the RUS measurement, the elastic tensors for these two materials were determined. For $Mo_3Sb_{6.925}Te_{0.075}$, c_{11} = 185 GPa, c_{12} = 86 GPa, c_{44} = 74.0 GPa, and c' = 49 GPa. These values are slightly higher compared to the parent Mo_3Sb_7, and with further addition of tellurium,

these values continue to increase. For $Mo_3Sb_{6.9}Te_{0.1}$, c_{11} = 189 GPa, c_{12} = 88 GPa, c_{44} = 75.4 GPa, and c' = 50 GPa. Again, like the ruthenium doping, the addition of tellurium dopant to the parent material acts to increase these elastic constants. The temperature dependence of c' and c_{44} for these materials is provided in Figure 4.6. As expected, these materials behave very similarly; they also behave much like the $Mo_{2.91}Ru_{0.09}Sb_7$ material seen above. The c_{44} value shows only slight stiffening as the temperature is decreased, and the c' value displays a definite softening due to a structural instability near the structural transition temperature for the parent material.

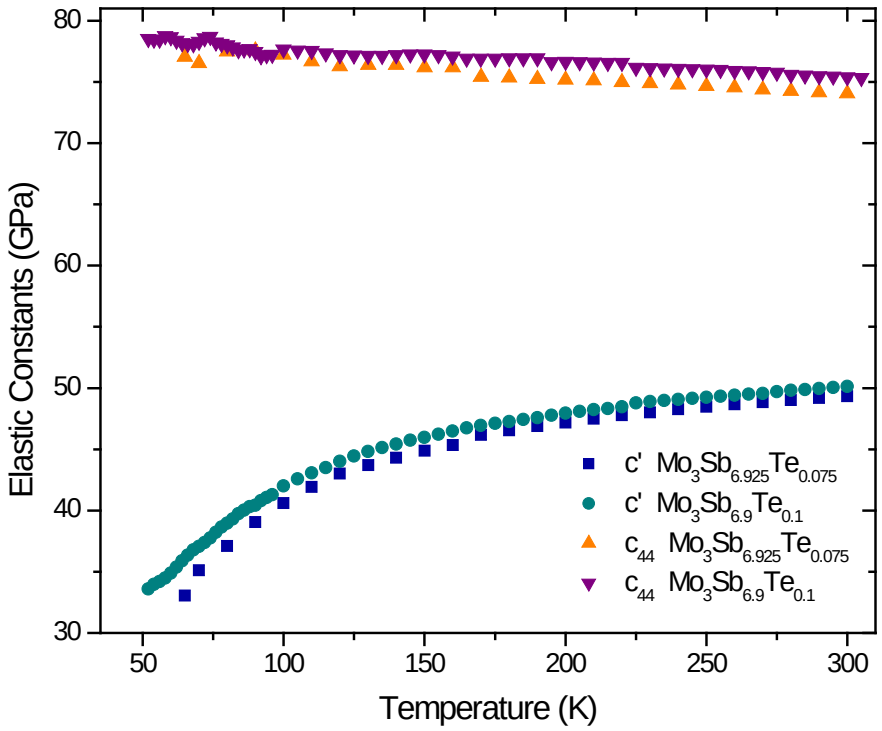

Figure 4.6. Temperature-dependent elastic constants for $Mo_3Sb_{6.925}Te_{0.075}$ and $Mo_3Sb_{6.9}Te_{0.1}$.

4.1.3 $Mo_{3-x}Cr_xSb_7$

Though ruthenium doping and tellurium doping affect the Mo_3Sb_7 material in similar ways, the effect of chromium doping is rather different. With the addition of chromium on the

molybdenum site, the structural transition persists, yet at a slightly lower temperature. In addition, no superconducting transition is observed above 1.8K. Here, RUS is used to examine the elastic behavior of two chromium-doped materials: Mo_2CrSb_7 and $Mo_{2.4}Cr_{0.6}Sb_7$.

For Mo_2CrSb_7, the room temperature elastic constants are determined from RUS, and they are as follows: c_{11} = 164 GPa, c_{12} = 80 GPa, c_{44} = 63.8 GPa, and c' = 42 GPa. Contrary to the previous elemental dopings, the addition of chromium reduces these elastic constants when compared with the parent Mo_3Sb_7. Figure 4.7 displays the temperature dependence of c' and c_{44} for this material. As before, c_{44} does not change much with decreasing temperature; however, the softening seen in c' is very evident. This more intense softening is expected for this material since it does undergo a structural transition at about 48K. The temperature dependences of c' for the Mo_2CrSb_7 and $Mo_{2.4}Cr_{0.6}Sb_7$ materials are compared in Figure 4.8. At higher temperatures, additional chromium doping decreases the value of c'. However, as the temperature is cooled to near the cubic-to-tetragonal structural transition at 48K, both materials show a very similar drop in c'. Interestingly, the structural transition temperature is reduced upon chromium doping the parent material (from 53K to 48K), but in this chromium composition range ($0.6 \leq x \leq 1$), the amount of chromium does not change this temperature significantly. For both Mo_2CrSb_7 and $Mo_{2.4}Cr_{0.6}Sb_7$, this transition occurs near 48K. It is also noteworthy that the structural transition is much more resilient with chromium doping than with ruthenium doping. This structural transition, including the structural instability, was fully suppressed in the $Mo_{2.1}Ru_{0.9}Sb_7$ material; however, this transition remains in the Mo_2CrSb_7 material with a higher x value.

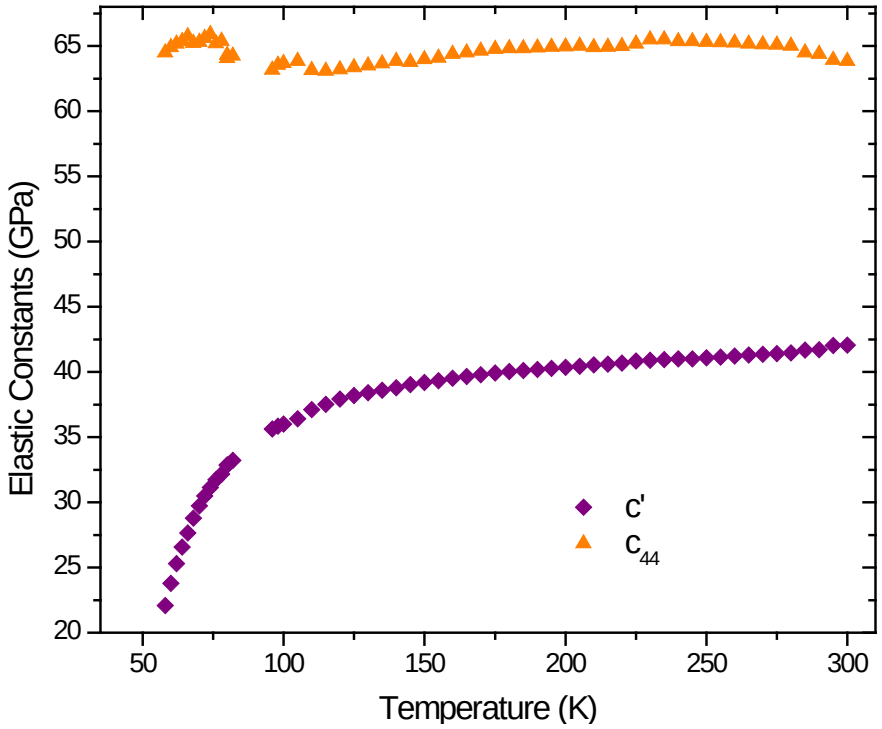

Figure 4.7. Temperature-dependent elastic constants for Mo_2CrSb_7.

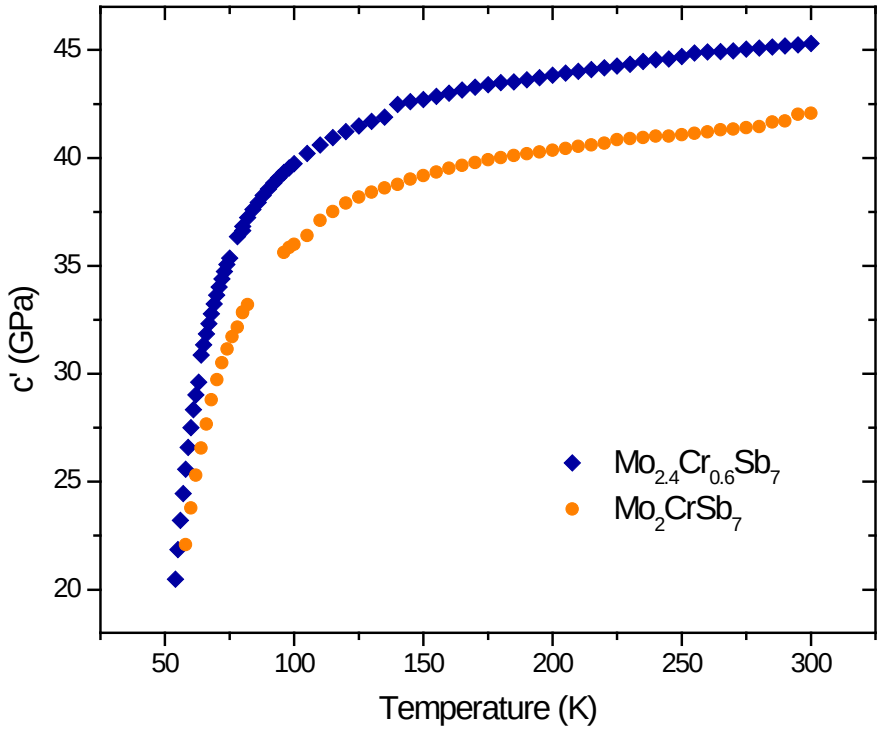

Figure 4.8. Comparison of temperature-dependent c' for $Mo_{2.4}Cr_{0.6}Sb_7$ and Mo_2CrSb_7.

4.2 Compilation

Looking at individual samples, it is difficult to visualize the amount of softening that occurs in each of these materials and to perceive how each of the elemental dopings affect the parent Mo_3Sb_7. In order to more clearly observe the effect of the ruthenium, tellurium, and chromium dopants on the temperature-dependent elastic behavior of Mo_3Sb_7, the *c'* values have been normalized at room temperature and plotted together. This comparison is seen in Figure 4.9. While each of these materials reveals a definite softening upon cooling, it is evident that this effect is much more prominent in the materials that undergo the structural phase transition from cubic to tetragonal. The parent material and chromium-doped material, which do display this transition, experience a very sharp softening as this transition temperature is approached at 53K and 48K, respectively. The softening observed for the ruthenium-doped and the tellurium-doped

materials is noticeably more gradual, and as was shown earlier, additional ruthenium doping eliminates this softening, indicating suppression of the structural instability.

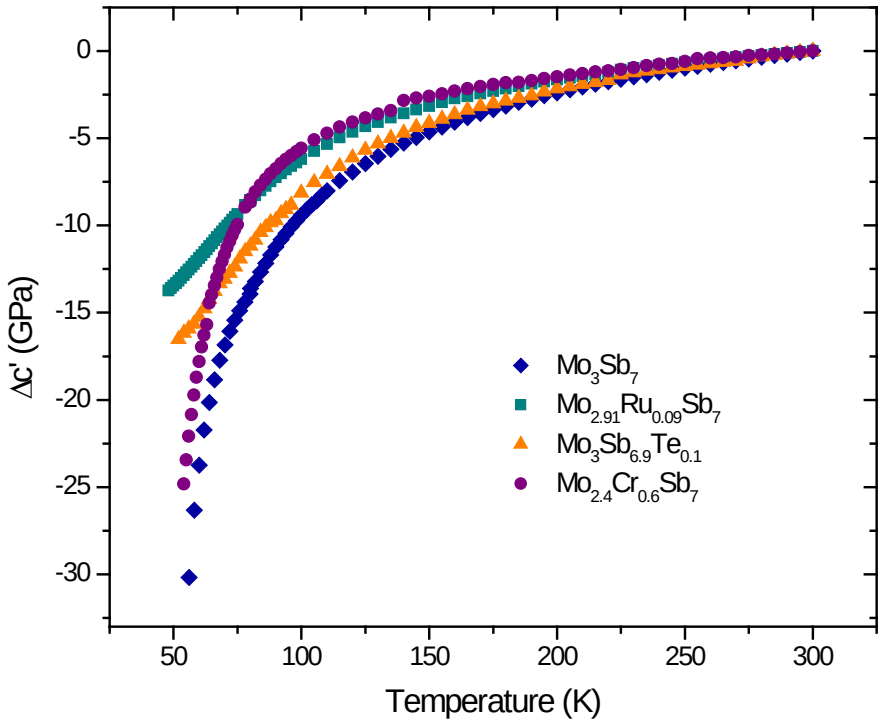

Figure 4.9. Normalized c′ for Mo_3Sb_7 parent and doped materials.

Conclusion

The relationship between structural instability, magnetic ordering, and superconductivity is often complicated. RUS has been used to examine the effect of these interactions on the elastic behavior of some interesting iron-based superconductors and thermoelectric materials as a function of temperature. The evolution of these behaviors with the addition of elemental dopants is also examined.

An RUS investigation of iron-based superconductors and related materials grown using a self-flux technique reveals how their elastic behavior changes as a function of temperature. The $BaFe_2As_2$ parent material displays a large softening as the tetragonal-to-orthorhombic structural distortion is approached near 132K. While an antiferromagnetic spin-density-wave ordering also occurs at this temperature, such a dramatic softening is indicative of a structural instability. This softening is arrested immediately following the transition. Though this type of behavior is often associated with structural transitions, it is not expected for superconducting transitions. However, a very dramatic softening is observed in the $BaFe_{1.84}Co_{0.16}As_2$ superconducting material as its critical temperature of 22K is approached. This observation, as well as the behavior of the parent material, is the result of magnetically-driven nematic fluctuations that emerge at higher temperatures. Though the structural transition temperature is higher than the magnetic transition temperature for cobalt-doped $BaFe_2As_2$, the structural transition is actually a result of the magnetic fluctuations. The suppression of the $BaFe_2As_2$ structural transition with the addition of cobalt is also observed with RUS. An underdoped material reveals a less dramatic softening near the structural transition temperature, which is also reduced, and a highly-doped material displays only gradual stiffening as temperature decreases.

A series of chromium-doped $BaFe_2As_2$ materials is also developed in order to study the effect of chromium on this system. The addition of this element does not produce superconductivity at any concentration. While the structural and associated magnetic transitions are suppressed by the addition of chromium, substantially more dopant is required to achieve this suppression than in the case of cobalt doping. The suppression of the structural distortion with the addition of chromium can be clearly observed in the temperature dependence of the elastic behavior. The destruction of these transitions is clearly not the sole requirement for the production of superconductivity in $BaFe_2As_2$. Strong magnetism in the form of competing spin-density-wave antiferromagnetic order and G-type antiferromagnetic order exists throughout the $BaFe_{2-x}Cr_xAs_2$ phase diagram, and this magnetic preference is sufficient to prevent the emergence of superconductivity.

The elastic behavior of $TlFe_{1.6}Se_2$, a material close to superconductivity, displays a small amount of softening at a transition near 140K, and stiffening occurs as a second transition near 100K is approached. While these transitions have been described by a canting of the magnetic moment, application of a magnetic field along the c-axis does not have much effect on the elastic behavior. Because the magnetic moments cant away from the c-axis at 140K and application of magnetic field does not suppress the transition at this temperature, we can conclude that these transitions are not entirely due to magnetic canting.

RUS studies of a series of Mo_3Sb_7-based promising thermoelectric materials reveal a strong elastic response near 53K, the structural transition temperature for the parent Mo_3Sb_7. At this temperature, the material undergoes a transition from cubic symmetry to tetragonal symmetry. This parent material displays a very distinct softening as this transition temperature is approached. The addition of chromium suppresses this transition temperature slightly to 48K.

The chromium-doped materials also display a sharp softening as this temperature is approached. On the other hand, both ruthenium and tellurium doping suppress this transition to tetragonal symmetry. However, RUS results indicate that a structural instability still exists at doping levels of x = 0.09 and x = 0.1 for $Mo_{3-x}Ru_xSb_7$ and $Mo_3Sb_{7-x}Te_x$, respectively. This instability is manifested as an apparent softening in the temperature region near the transition temperature of the parent material. The elimination of this instability with further ruthenium doping is also observed.

References

[1] D. van Delft, P. Kes, Physics Today **63** (2010) 38-43.
[2] C.P. Poole, H.A. Farach, R.J. Creswick, R. Prozorov, Superconductivity, 2nd Ed., Elsevier/Academic Press, Amsterdam; Boston, 2007, 671 p.
[3] J. Bardeen, L.N. Cooper, J.R. Schrieffer, Physical Review **106** (1957) 162-164.
[4] J.G. Bednorz, K.A. Muller, Zeitschrift Fur Physik B-Condensed Matter **64** (1986) 189-193.
[5] M.K. Wu, J.R. Ashburn, C.J. Torng, P.H. Hor, R.L. Meng, L. Gao, Z.J. Huang, Y.Q. Wang, C.W. Chu, Physical Review Letters **58** (1987) 908-910.
[6] P.C. Dai, J.P. Hu, E. Dagotto, Nature Physics **8** (2012) 709-718.
[7] Y. Kamihara, T. Watanabe, M. Hirano, H. Hosono, Journal of the American Chemical Society **130** (2008) 3296.
[8] Z.A. Ren, J. Yang, W. Lu, W. Yi, X.L. Shen, Z.C. Li, G.C. Che, X.L. Dong, L.L. Sun, F. Zhou, Z.X. Zhao, Epl **82** (2008) 57002.
[9] Z.A. Ren, J. Yang, W. Lu, W. Yi, G.C. Che, X.L. Dong, L.L. Sun, Z.X. Zhao, Materials Research Innovations **12** (2008) 105-106.
[10] Z.A. Ren, W. Lu, J. Yang, W. Yi, X.L. Shen, Z.C. Li, G.C. Che, X.L. Dong, L.L. Sun, F. Zhou, Z.X. Zhao, Chinese Physics Letters **25** (2008) 2215-2216.
[11] K. Ishida, Y. Nakai, H. Hosono, Journal of the Physical Society of Japan **78** (2009) 062001.
[12] J. Paglione, R.L. Greene, Nature Physics **6** (2010) 645-658.
[13] M. Rotter, M. Tegel, D. Johrendt, I. Schellenberg, W. Hermes, R. Pottgen, Physical Review B **78** (2008) 020503.
[14] M. Rotter, M. Tegel, D. Johrendt, Physical Review Letters **101** (2008) 107006.
[15] A.S. Sefat, R.Y. Jin, M.A. McGuire, B.C. Sales, D.J. Singh, D. Mandrus, Physical Review Letters **101** (2008) 117004.
[16] A.A. Aczel, E. Baggio-Saitovitch, S.L. Budko, P.C. Canfield, J.P. Carlo, G.F. Chen, P.C. Dai, T. Goko, W.Z. Hu, G.M. Luke, J.L. Luo, N. Ni, D.R. Sanchez-Candela, F.F. Tafti, N.L. Wang, T.J. Williams, W. Yu, Y.J. Uemura, Physical Review B **78** (2008) 214503.
[17] C. Lester, J.H. Chu, J.G. Analytis, S.C. Capelli, A.S. Erickson, C.L. Condron, M.F. Toney, I.R. Fisher, S.M. Hayden, Physical Review B **79** (2009) 144523.
[18] S. Aswartham, M. Abdel-Hafiez, D. Bombor, M. Kumar, A.U.B. Wolter, C. Hess, D.V. Evtushinsky, V.B. Zabolotnyy, A.A. Kordyuk, T.K. Kim, S.V. Borisenko, G. Behr, B. Buchner, S. Wurmehl, Physical Review B **85** (2012) 224520.
[19] Z. Bukowski, S. Weyeneth, R. Puzniak, P. Moll, S. Katrych, N.D. Zhigadlo, J. Karpinski, H. Keller, B. Batlogg, Physical Review B **79** (2009) 104521.
[20] L.J. Li, Y.K. Luo, Q.B. Wang, H. Chen, Z. Ren, Q. Tao, Y.K. Li, X. Lin, M. He, Z.W. Zhu, G.H. Cao, Z.A. Xu, New Journal of Physics **11** (2009) 025008.
[21] S. Sharma, A. Bharathi, S. Chandra, V.R. Reddy, S. Paulraj, A.T. Satya, V.S. Sastry, A. Gupta, C.S. Sundar, Physical Review B **81** (2010) 174512.
[22] A. Thaler, N. Ni, A. Kracher, J.Q. Yan, S.L. Bud'ko, P.C. Canfield, Physical Review B **82** (2010) 014534.
[23] N. Ni, A. Thaler, A. Kracher, J.Q. Yan, S.L. Bud'ko, P.C. Canfield, Physical Review B **80** (2009) 024511.
[24] X.L. Wang, H.Y. Shi, X.W. Yan, Y.C. Yuan, Z.Y. Lu, X.Q. Wang, T.S. Zhao, Applied Physics Letters **96** (2010) 012507.
[25] S.R. Saha, T. Drye, K. Kirshenbaum, N.P. Butch, P.Y. Zavalij, J. Paglione, Journal of Physics-Condensed Matter **22** (2010) 072204.

[26] X.Y. Zhu, F. Han, G. Mu, P. Cheng, J. Tang, J. Ju, K. Tanigaki, H.H. Wen, Physical Review B **81** (2010) 104525.
[27] S. Kasahara, K. Hashimoto, R. Okazaki, H. Shishido, M. Yamashita, K. Ikada, S. Tonegawa, N. Nakata, Y. Sensyu, H. Takeya, K. Hirata, T. Shibauchi, T. Terashima, Y. Matsuda, Physica C-Superconductivity and Its Applications **470** (2010) S462-S463.
[28] M. Rotter, M. Pangerl, M. Tegel, D. Johrendt, Angewandte Chemie-International Edition **47** (2008) 7949-7952.
[29] F.C. Hsu, J.Y. Luo, K.W. Yeh, T.K. Chen, T.W. Huang, P.M. Wu, Y.C. Lee, Y.L. Huang, Y.Y. Chu, D.C. Yan, M.K. Wu, Proceedings of the National Academy of Sciences of the United States of America **105** (2008) 14262-14264.
[30] A.M. Zhang, J.H. Xiao, Y.S. Li, J.B. He, D.M. Wang, G.F. Chen, B. Normand, Q.M. Zhang, T. Xiang, Physical Review B **85** (2012) 214508.
[31] M.H. Fang, H.D. Wang, C.H. Dong, Z.J. Li, C.M. Feng, J. Chen, H.Q. Yuan, Epl **94** (2011) 27009.
[32] B.C. Sales, M.A. McGuire, A.F. May, H.B. Cao, B.C. Chakoumakos, A.S. Sefat, Physical Review B **83** (2011) 224510.
[33] H.B. Cao, C. Cantoni, A.F. May, M.A. McGuire, B.C. Chakoumakos, S.J. Pennycook, R. Custelcean, A.S. Sefat, B.C. Sales, Physical Review B **85** (2012) 054515.
[34] L. Haggstrom, H.R. Verma, S. Bjarman, R. Wappling, R. Berger, Journal of Solid State Chemistry **63** (1986) 401-408.
[35] A.F. May, M.A. McGuire, H.B. Cao, I. Sergueev, C. Cantoni, B.C. Chakoumakos, D.S. Parker, B.C. Sales, Physical Review Letters **109** (2012) 077003.
[36] A.D. LaLonde, Y.Z. Pei, H. Wang, G.J. Snyder, Materials Today **14** (2011) 526-532.
[37] J.M. An, A. Subedi, D.J. Singh, Solid State Communications **148** (2008) 417-419.
[38] O. Delaire, J. Ma, K. Marty, A.F. May, M.A. McGuire, M.H. Du, D.J. Singh, A. Podlesnyak, G. Ehlers, M.D. Lumsden, B.C. Sales, Nature Materials **10** (2011) 614-619.
[39] E.S. Bozin, C.D. Malliakas, P. Souvatzis, T. Proffen, N.A. Spaldin, M.G. Kanatzidis, S.J.L. Billinge, Science **330** (2010) 1660-1663.
[40] J. Ma, O. Delaire, A.F. May, C.E. Carlton, M.A. McGuire, L.H. VanBebber, D.L. Abernathy, G. Ehlers, T. Hong, A. Huq, W. Tian, V.M. Keppens, Y. Shao-Horn, B.C. Sales, Nature Nanotechnology **8** (2013) 445-451.
[41] T.M. Tritt, M.A. Subramanian, MRS Bulletin **31** (2006) 188-194.
[42] X.Y. Shi, Y.Z. Pei, G.J. Snyder, L.D. Chen, Energy & Environmental Science **4** (2011) 4086-4095.
[43] P. Villars, K. Cenzual, Pearson's Crystal Data: Crystal Structure Database for Inorganic Compounds (on CD-ROM), Release 2012/13, ASM International®, Materials Park, Ohio, USA.
[44] J.-Q. Yan, M.A. McGuire, A.F. May, D.G. Mandrus, B.C. Sales, (2012) unpublished manuscript.
[45] J.Q. Yan, M.A. McGuire, A.F. May, H. Cao, A.D. Christianson, D.G. Mandrus, B.C. Sales, Physical Review B **87** (2013) 104515.
[46] C. Candolfi, B. Lenoir, J. Leszczynski, A. Dauscher, E. Guilmeau, Journal of Applied Physics **105** (2009) 083701.
[47] C. Candolfi, B. Lenoir, J. Leszczynski, A. Dauscher, J. Tobola, S.J. Clarke, R.I. Smith, Inorganic Chemistry **48** (2009) 5216-5223.

[48] C. Candolfi, J. Leszczynski, P. Masschelein, C. Chubilleau, B. Lenoir, A. Dauscher, E. Guilmeau, J. Hejtmanek, S.J. Clarke, R.I. Smith, Journal of Electronic Materials **39** (2010) 2132-2135.
[49] V.H. Tran, W. Miiller, Z. Bukowski, Physical Review Letters **100** (2008) 137004.
[50] Z. Bukowski, D. Badurski, J. Stepien-Damm, R. Troc, Solid State Communications **123** (2002) 283-286.
[51] A. Migliori, J.L. Sarrao, Resonant ultrasound spectroscopy: applications to physics, materials measurements, and nondestructive evaluation, Wiley, New York; Chichester, 1997, 201 p.
[52] A. Migliori, J.D. Maynard, Review of Scientific Instruments **76** (2005) 121301.
[53] J. Maynard, Physics Today **49** (1996) 26-31.
[54] D.B. Fraser, R.C. Lecraw, Review of Scientific Instruments **35**, (1964) 1113-1115.
[55] Schreibe.E, O.L. Anderson, N. Soga, N. Warren, C. Scholz, Science **167** (1970) 732-734.
[56] H.H. Demarest, Journal of the Acoustical Society of America **49** (1971) 768-775.
[57] I. Ohno, Journal of Physics of the Earth **24** (1976) 355-379.
[58] W.M. Visscher, A. Migliori, T.M. Bell, R.A. Reinert, Journal of the Acoustical Society of America **90** (1991) 2154-2162.
[59] A. Migliori, J.L. Sarrao, W.M. Visscher, T.M. Bell, M. Lei, Z. Fisk, R.G. Leisure, Physica B **183** (1993) 1-24.
[60] R.G. Leisure, F.A. Willis, Journal of Physics-Condensed Matter **9** (1997) 6001-6029.
[61] R.M. Fernandes, L.H. VanBebber, S. Bhattacharya, P. Chandra, V. Keppens, D. Mandrus, M.A. McGuire, B.C. Sales, A.S. Sefat, J. Schmalian, Physical Review Letters **105** (2010) 157003.
[62] C. Fang, H. Yao, W.F. Tsai, J.P. Hu, S.A. Kivelson, Physical Review B **77** (2008) 224509.
[63] C. Xu, M. Muller, S. Sachdev, Physical Review B **78** (2008) 020501.
[64] Y. Qi, C.K. Xu, Physical Review B **80** (2009) 094402.
[65] V. Barzykin, L.P. Gor'kov, Physical Review B **79** (2009) 134510.
[66] P. Chandra, P. Coleman, A.I. Larkin, Physical Review Letters **64** (1990) 88-91.
[67] A.S. Sefat, D.J. Singh, L.H. VanBebber, Y. Mozharivskyj, M.A. McGuire, R.Y. Jin, B.C. Sales, V. Keppens, D. Mandrus, Physical Review B **79** (2009) 224524.
[68] K. Marty, A.D. Christianson, C.H. Wang, M. Matsuda, H. Cao, L.H. VanBebber, J.L. Zarestky, D.J. Singh, A.S. Sefat, M.D. Lumsden, Physical Review B **83** (2011) 060509.

Vita

Lindsay Heatherly VanBebber received her B.S. in Materials Science and Engineering from the University of Tennessee, Knoxville in 2004. Staying at UT, she worked as a research assistant in Dr. Pharr's lab while earning her M.S. degree, also in Materials Science and Engineering. Her research involved study of a combinatorial method for making ternary compositions and nanofriction. She received her non-thesis M.S. in 2008 following a leave of absence.

In 2008, Lindsay joined Dr. Keppens' lab while working toward her Ph.D. She served as both a research assistant as well as a teaching assistant for several undergraduate laboratory classes. Her research centered on using Resonant Ultrasound Spectroscopy in order to examine the elastic behavior of materials, particularly, the popular iron-based superconductors and promising thermoelectric materials.